

FG

12

RADC-TR-76-112
Final Technical Report
April 1976



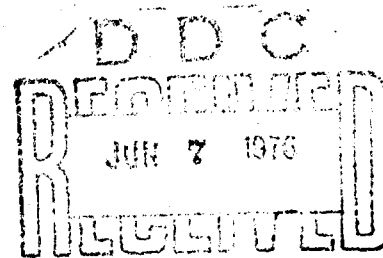
PREDETECTION COMPENSATED IMAGING

Hughes Research Laboratories

Sponsored by
Defense Advanced Research Projects Agency
ARPA Order No. 2646

AD A 025190

Approved for public release;
distribution unlimited.



[Handwritten signature]

**ROME AIR DEVELOPMENT CENTER
AIR FORCE SYSTEMS COMMAND
GRIFFISS AIR FORCE BASE, NEW YORK 13441**

SECTIONS V and VI (pages 89 - 135) have been deleted from this document.

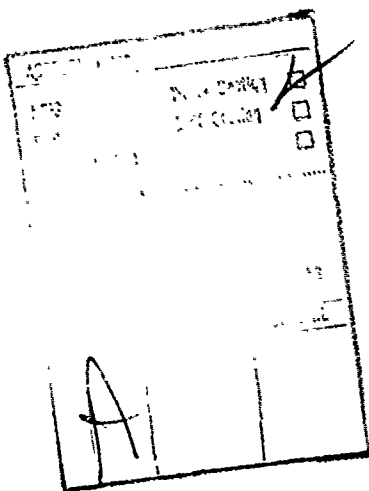
This report has been reviewed by the RADC Information Office (OI) and is releasable to the National Technical Information Service (NTIS). At NTIS it will be releasable to the general public including foreign nations.

This report has been reviewed and is approved for publication.

APPROVED:



DONALD W. HANSON
Project Engineer



The views and conclusions contained in this document are those of the authors and should not be interpreted as necessarily representing the official policies, either expressed or implied, of the Defense Advanced Research Projects Agency or the U. S. Government.

Do not return this copy. Retain or destroy.

PREDETECTION COMPENSATED IMAGING

C. J. Swigert
W. P. Brown
T. R. O'Meara
D. Y. Tseng
S. Wandzura

Contractor: Hughes Research Laboratories
Contract Number: F30602-75-C-0026
Effective Date of Contract: 16 September 1974
Contract Expiration Date: 15 August 1975
Amount of Contract: \$235,000.00
Program Code Number: 5E20
Period of work covered: Sep 74 - Aug 75

Principal Investigator: C. J. Swigert
Phone: 213 456-6411

Project Engineer: Donald W. Hanson
Phone: 315 330-3145

Approved for public release;
distribution unlimited.

This research was supported by the Defense Advanced Research Projects Agency of the Department of Defense and was monitored by Donald W. Hanson (OCSE), Griffiss AFB NY 13441.

UNCLASSIFIED

SECURITY CLASSIFICATION OF THIS PAGE (When Data Entered)

REPORT DOCUMENTATION PAGE		READ INSTRUCTIONS BEFORE COMPLETING FORM
1. REPORT NUMBER RAL-TR-76-112	2. GOVT ACCESSION NO.	3. REPORT PARTS CATALOG NUMBER
4. TYPE (and Subtype) PREDETECTION COMPENSATED IMAGING	5. TYPE OF REPORT & PERIOD COVERED Final Technical Report 16 Sep 74 - 15 Aug 75	6. PERFORMING ORG. REPORT NUMBER N/A
7. AUTHOR(s) C. J. Swigert, D. V. Tseng W. P. Brown, S. Wandzura T. R. O'Meara	8. CONTRACT OR GRANT NUMBER(s) F30602-75-C-0026, NEW WARRA/ARPA/AF-2646	9. PERFORMING ORGANIZATION NAME AND ADDRESS Hughes Research Laboratories 3011 Malibu Canyon Road Malibu CA 90265
10. CONTROLLING OFFICE NAME AND ADDRESS Defense Advanced Research Projects Agency 1400 Wilson Blvd Arlington VA 22209	11. REPORT DATE April 1976	12. NUMBER OF PAGES 180
14. MONITORING AGENCY NAME & ADDRESS (if different from Controlling Office) Rome Air Development Center (OCSE) Griffiss AFB NY 13441	15. SECURITY CLASS (of this report) UNCLASSIFIED	15a. DECLASSIFICATION/DOWNGRADING SCHEDULE S/A
16. DISTRIBUTION STATEMENT (of this Report) Approved for public release; distribution unlimited		
17. DISTRIBUTION STATEMENT (of the abstract entered in Block 20, if different from Report) Same		
18. SUPPLEMENTARY NOTES RADP Project Engineer: Donald W. Hanson (OCSE) SECTIONS V and VI (pages 89 - 135) have been deleted from this document.		
19. KEY WORDS (Continue on reverse side if necessary and identify by block number) COAT, Predetection Compensation, Image Formation, Turbulence Compensation, Adaptive Optical Systems, Deformable Mirror, Signal to Noise Ratio, Predictive Track, Visual Assessment		
20. ABSTRACT (Continue on reverse side if necessary and identify by block number) This report describes the techniques developed and evaluated for predetection compensated imaging systems to measure and correct wavefront distortions at a telescope aperture. One approach to compensate these wavefront distortions is to introduce the appropriate (real-time) wavefront correction ahead of the image formation process.		

(Cont'd)

UNCLASSIFIED

SECURITY CLASSIFICATION OF THIS PAGE(When Data Entered)

We call systems that achieve such corrections Imaging COAT (coherent Optical Adaptive Techniques) systems, since they are spatically coherent systems.

Two general classes of wavefrnt error sensors have been identified and explored in this study. We have also examined several wavefront perturbation techniques (multidither techniques) that allow a detector to operate in a time shared mode to collect the wavefront error data that would normally require the use of several detectors using a non-perturbation mode of operation. This technique has been developed and refined into the Multiple Aperture InterLinked (MAIL) predetection compensation system.

When advantageous, we use the MAIL concept for predictive track of multiple phase layers to obtain an extended integration time; otherwise, we rely on "quick looks" of the phase error while viewing a bright target. An improved predictive track procedure is described and illustrated that obtains a least squares error solution to an atmospheric phase model. A visual assessment of image degradation with different amounts of phase distortion has also been performed and is illustrated. While the image quality assessments are subjective, there is a correlation between image degradation and rms phase distortion.

UNCLASSIFIED

SECURITY CLASSIFICATION OF THIS PAGE(When Data Entered)

TABLE OF CONTENTS

SECTION		PAGE
I	INTRODUCTION TO PREDETECTION COMPENSATED IMAGING SYSTEMS	11
II	CLASSES OF WAVEFRONT ERROR SENSORS	17
	A. Comparison of Quantum Noise Effects on the Hartman-Test and Pinhole Interfero- meter Systems.	18
	B. Wavefront Correction with a Pinhole Interferometer for an Extended Target.	33
	C. Computer Evaluation of Wavefront Correction with Image Quality Detectors	38
III	DEFORMABLE MIRROR DESIGN	49
	A. Surface Figure.	52
	B. Structural Resonances	56
	C. Interactuator Coupling	65
IV	THE MULTIPLE APERTURE INTERLINKED BLOCK CODED SYSTEM.	77
	A. Introduction.	77
	B. Pairwise Element Angle Calculation for Four Elements per Block	82
	C. Block Rectification Procedure for Four Elements per Block	84
	D. Introduction to the Two Element per Block Organization	85
	E. Element Angle Calculation for Two Elements per Block	86

SECTION V deleted from this document

SECTION VI deleted from this document

VII	IMPROVED PREDICTIVE TRACK PROCEDURES . . .	137
	A. One Phase Layer "Quick Look" Technique	137
	B. Multiple Phase Layer Predictive Track Scheme	140
	C. Unobservable Multiple Phase Layers	148
VIII	IMAGE QUALITY WITH RMS PHASE ERROR,	157
IX	REPORT CONCLUSIONS.	171
	REFERENCES	173
	APPENDIX	175

LIST OF ILLUSTRATIONS

FIGURE		PAGE
I-1	An imaging COAT system is basically a servo-mechanism	13
II-1	Pinhole interferometer	20
II-2	Four-quadrant detectors for each subaperture	21
II-3	Flow chart for predetection compensation	39
II-4	Phasor diagram for the electric fields, using element by element method.	40
II-5	Phasor diagram for the electric fields, using elements by halves method.	42
II-6	Walsh functions (1, 2, 3, 4)	44
III-1(a)	Sixty-four element I-COAT deformable mirror prototype	50
III-1(b)	Interferogram of surface showing one actuator energized	50
III-2	Hughes high power phase compensating deformable mirror	51
III-3	High power 28 kHz deformable dither mirror prototype.	53
III-4	Conceptual phase corrector/dither mirror configurations	54
III-5	Faceplate-actuator design considerations	55
III-6	Isocontours of a portion of the 64-element I-COAT mirror	57
III-7	Double-pulse holographic interferogram of the 64-element I-COAT mirror	58
III-8	Actuator, faceplate, and backplate resonant modes.	59
III-9	Resonant frequencies of the faceplate/actuator mode, and actuator column modes	61
III-10	Interactuator coupling as a function of ratio of actuator head diameter to actuator spacing	66

FIGURE		PAGE
III-11	Seven actuators	67
III-12	Faceplate section	67
III-13	Actuator head	69
III-14	Spring model	72
III-15	Conceptual deformable mirror cross-section using a honeycomb backplate structure	74
IV-1	Block-coded, multiple-apertured, inter-linked imaging COAT system.	79
IV-2	Linked, block-coded I-COAT system.	79
IV-3	Typical mirror deformations and block- plane images with piston mirrors	80
IV-4	Phasor diagram which defines ϕ_A	80
IV-5	Linked, block-coded I-COAT system.	81

FIGURES FOR SECTION V AND VI deleted from this document.

VII-1	Optical geometry for measurement of phase layers by 12 detectors.	141
VII-2	Optical setup for least squares estimation procedure.	142
VII-3	Phase measurement matrix for Fig. VI-2 and 3 detectors and 9 measurement time intervals.	145

FIGURE		PAGE
VII-4	Pseudoinverse of matrix A in Fig. III-3	147
VII-5	Unmeasurable basis vectors for two layer atmosphere	151
VIII-1	Comparison of computer calculated and theoretical phase structure function results	160
VIII-2	Photograph of object on display	162
VIII-3	Selective gain curve applied in LABGC within a window area.	162
VIII-4	Degraded image, using phase screen No. 3 for conditions in Table VIII-1	165
VIII-5	Degraded image, using phase screen No. 32 for conditions in Table VIII-1	166
VIII-6	Degraded image, smoothed using five separate representations of random phase screen No. 3 for conditions in Table VIII-1	167
VIII-7	Degraded image, smoothed using five separate representations of random phase screen No. 32 for conditions in Table VIII-1.	168

PREFACE

This final report was prepared by Hughes Research Laboratories, Malibu, California under Contract No. F30602-75-C-0026. It describes work performed from 16 September 1974 to 15 August 1975. The Program Manager is C. J. Swigert who assumed this role in the last half of the program from J. A. Jenney. In addition to the authors we wish to acknowledge the contributions of V. Evtuhov, C. R. Giuliano, J. A. Jenney, L. Miller and V. Wang, who served as technical advisors for the whole range of technical problems that arose during the program.

I. INTRODUCTION TO PREDETECTION COMPENSATED IMAGING SYSTEMS

It was observed by the earliest astronomers that the resolution achievable with a large telescope is determined by atmospheric conditions rather than by the size of the telescope. Generally, it is observed that the resolution limit set by free-space diffraction theory is attained only for telescopes smaller than about 10 cm. Although larger telescopes have greater light-gathering capabilities, they do not have better resolution capabilities. The departure from the predictions of free-space diffraction theory is caused by the fact that the atmosphere is not a homogeneous medium, but rather contains random density variations caused by turbulence. The refractive index variations associated with these density variations cause the phase and amplitude of an image field to become randomized. Generally, the perturbing effect of the phase variations is dominant and amplitude scintillations are of secondary importance.

The objectives of this predetection compensated imaging systems study are to determine effective techniques both for the measurement of the wavefront errors at a telescope aperture and for the correction of these wavefront distortions. These techniques are to be identified through analysis, simulation, tradeoff studies and experimental measurements of the system elements required for wavefront error measurement and correction.

One approach to compensate these wavefront distortions is to introduce the appropriate (real-time) wavefront correction ahead of the image-formation process. We call systems that achieve such corrections Imaging COAT (Coherent Optical Adaptive Techniques) systems. In principle, both propagation and telescope figure-induced wavefront errors can be substantially reduced by such systems. Some classes of COAT systems may correct for amplitude variations as well, but these were not studied under this contract, since they were not judged essential for long range imaging.

Two general classes of wavefront error sensors have been identified and explored in this study. We have also examined several wavefront perturbation techniques (multiplier techniques) that allow a detector to operate in a time shared mode to collect the wavefront error data that would normally require the use of several detectors using a non-perturbation mode of operation. This technique has been developed and refined into the Multiple Aperture Interlinked (MAIL) predetection compensation system. This technique has been evaluated in detail in the First and Second Standard Noise Calculations performed under this contract and described below.

Basically, an imaging COAT system, as illustrated in Fig. I-1, consists of three components: (1) a reflective or transmissive device which changes path length, index, or phase shift as a function of spatial position over the beam according to prescribed error signal inputs, usually electrical signals. Since most such devices have a discrete phase control which is monotonic over some subapertures or control regions called the elements (which correspond roughly to the "elements" of a microwave phase array), we call such a phase-correcting system a phaser matrix. (2) An error-sensing system which either detects the departure (in radians) from uniformity of the received wavefront, or some secondary measure of its departure - for example, local wavefront tilt error. (3) A servo system which derives some measure of the local wavefront error and computes or establishes the required error signals to be supplied to the phaser matrix.

Early in the program we were motivated to examine image quality error sensing systems, in which the "wavefront" error sensor operates at a system image plane, preferably the main image plane of the system. Clearly, one does not obtain a direct wavefront error measure from such information. Alternatively, one must extract a measure of image quality or sharpness based on one or more measures of image sharpness via the image plane detectors; this measure is then maximized with respect to the available degrees of freedom, the mirror actuator or electrode excitations. There were two motivations for concentrating on this approach: (1) the number of additional detectors required for the approach was low, perhaps zero; and (2) confidence in performance would be high since local optical path difference errors in the separate imaging and wavefront processing paths following the beam splitter of Fig. I-1) could be avoided.

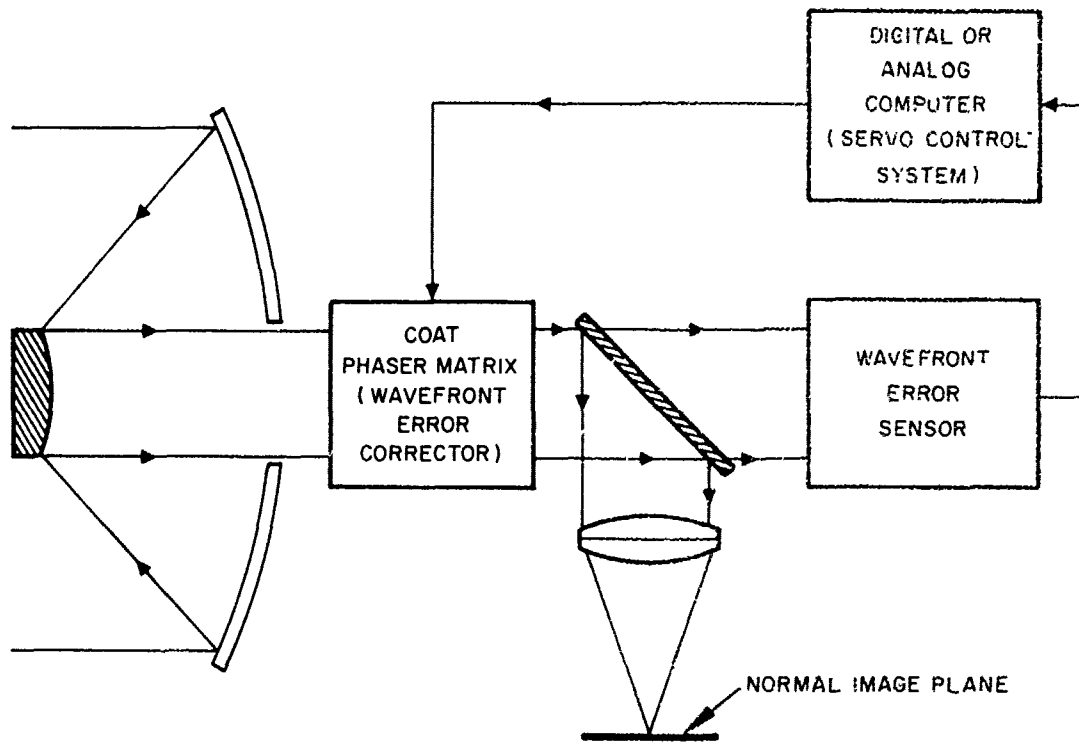


Fig. I-1. An imaging COAT system is basically a servo-mechanism which is capable of sensing phase errors in the arriving wavefront from atmospheric propagation effect or telescope figure distortions, and driving these to zero or an acceptably small value.

We had analyzed a number of such systems on IR&D (prior to the present contract) and for the sake of completeness are including some of these results in the current report (Section II). This work continued only for a very brief time on the present contract. We quickly found that most such systems achieve a signal-to-noise ratio which typically varies as the inverse of the square of the number of actuators and in the best cases as the inverse of the first power. This remained true for all image plane detection and/or dither policies of which we could conceive. At the same time, analysis of requirements was suggesting that the number of actuators would be between two hundred and four hundred and that the utmost in sensitivities would be required for applications of extreme interest. Further, analysis of the required speed of response was suggesting that it would be impossible to achieve the required dither excursion speeds, for image quality sensing, with conventional PZT driven mirrors. Clearly, image plane detection of the types considered to that point would not suffice.*

Consequently, a new class of dither systems was conceived which we call "block-encoded" systems, which avoided the inverse dependence upon the number of actuators and improved detection sensitivities in other respects. Further, the required number of dither excursions was reduced by many orders of magnitude. A particular subclass of the block-encoded systems, which we call Multiple-Aperture-InterLinked MAIL appeared to offer the best performance and the remainder of the program was devoted to achieving the best performance with this approach. This system is however more complex than its predecessors. For example, a separate detector plane is required to extract the error information.

Section II discusses the classes of wavefront error sensors analyzed in this study. Two general classes of wavefront error sensors, namely interferometric sensors and image quality sensors, are identified and explored in this study. The Searing interferometer and the pinhole interferometer, which is analyzed in some detail, are both examples of interferometric sensors. Image quality sensors include the Hartman test system, the integral of intensity through a mask, e. g., a pinhole, and the integral of intensity squared detector.

*These systems types are for long-range imaging through a turbulent atmosphere. We feel that the techniques may be perfectly suited to short-range problems or space telescopes where long servo integration times are feasible.

Section III reviews our deformable mirror design and development effort for image correction and dither. Because of program redirection to emphasize theoretical evaluation of the candidate predetection compensated imaging concepts, the deformable mirror design effort was not carried to completion.

Section IV presents the description of Hughes Research Laboratories predetection compensated imaging concept. The concept can be described as a block coded, multiple aperture interlinked (MAIL), deferred correction, polystep dither system.

Section V reviews our analysis of the MAIL compensated imaging system performance for the first standard noise calculation. The problem statements for the first and second standard noise calculations were presented to aid evaluation of the candidate predetection compensated imaging system. The parameters of the first Standard Noise problem are summarized in Table V-1.

Section VI reviews our analysis of the second standard noise problem for the MAIL compensated imaging system. The phase error measurement strategy for the MAIL concept is to use predictive track of multiple phase layers to obtain an extended integration time, when it is advantageous; otherwise, rely on "quick looks" of the phase error while viewing a bright target. Due to lack of time, the predictive track algorithm has not been optimally formulated for the second Standard Noise calculation.

Section VII presents an improved predictive track procedure that obtains a least squares error solution to an atmospheric phase model. The atmospheric model contains only two phase layers, but permits a complete demonstration of the track procedure. It is shown that there will always be six unobservable phase patterns out of the set of all possible phase patterns that can never be measured with this predictive track procedure. Further, it is concluded that with the addition of more phase layers to the atmospheric model, there will be more unmeasurable phase patterns added to the null space. However, we have not determined the frequency with which these phase patterns will occur.

Section VIII presents the results of a visual assessment of image degradation with different amounts of phase distortion. While the image quality assessments are subjective, there is a correlation between image degradation and rms phase distortion.

Section IX presents the summary conclusions of the report.

II. CLASSES OF WAVEFRONT ERROR SENSORS

Two general classes of wavefront error sensors have been identified and explored in this study. The two generic classes of wavefront error sensors are interferometric sensors and image quality sensors. The Shearing interferometer and the pinhole interferometer, which has been analyzed at Hughes Research Laboratories, are both examples of interferometric sensors. Image quality sensors include the Hartman test system, the integral of intensity through a mask, e. g., a pinhole, and the integral of intensity squared detector.

Early in the study the Hartman test system showed good signal-to-noise characteristics as a wavefront error sensor. Similarly, the pinhole interferometer, which is basically M Michelson interferometers in parallel, with one for each of the M phase shifter elements, has good signal-to-noise characteristics. A comparative signal-to-noise ratio analysis of these two sensors for point sources is presented in Section II-A. Further analysis of the pinhole interferometer has demonstrated an inability to measure the correct phase distortion when viewing multiple point sources and extended targets. The degradation, i. e., increased noise, is caused by the mixing of the multiple wavefronts from the multiple sources at each of the detectors. An analysis of this multiple target process is presented in Section II-B.

In parallel with the analysis of the Hartman and pinhole interferometer, considerable effort has been expended to develop viable image quality techniques. An analytic computer simulation of the predetection compensation process was developed to evaluate the performance characteristics of image quality improvement measuring (1) integral of intensity through a pinhole matched to the Airy disk size and (2) integral of intensity squared. A description of the simulation and the results are presented in Section II-C. The results indicate the required target brightness for good wavefront correction, e. g., $\langle(\Delta\Phi)^2\rangle$ less than 0.4 or $\lambda/10$ correction, under typical seeing conditions, is greater than the brightness of most targets of interest. An examination of this excessively large target brightness requirement indicates that the source of the difficulty is an excessively large noise component in the signal-to-noise ratio calculation. Since the image quality

measurement is made with only one detector, the signal component for each element of the primary aperture acts like a noise term for the phase measurement of each of the other elements comprising the primary aperture. Our technique to improve the signal-to-noise ratio is to use more detectors and have each detector view only two or four actuator elements at the primary aperture. This technique has been developed into a Multiple Aperture InterLinked (MAIL) system, described in Section IV, and has been our baseline concept for comparative evaluation in the first and second Standard Noise calculation for predetection compensation imaging systems.

A. Comparison of Quantum Noise Effects on the Hartman-Test and Pinhole Interferometer Systems

This section mathematically compares the signal-to-noise sensitivities of the Hartmann test and the pinhole-interferometer adaptive imaging systems. The comparison is done for four discrete cases and, in each case, for a continuum of targets. The four cases are

- Case I Filled disk of n subapertures, system nearly converged
- Case II Ring of n subapertures, system nearly converged
- Case III Filled disk of n subapertures, system unconverged
- Case IV Ring of n subapertures, system unconverged.

The unconverged state is that where the phases of the wavefront in each subaperture are nearly stochastically independent, i. e.,

$$\left| \sum_{k=1}^n e^{i\phi_k} \right|_{\text{unconverged}} \approx \sqrt{n} \quad (2.1)$$

This condition holds, for example, when the system is first turned on. The nearly converged state has the subaperture phases differing from each other by only fractions of a radian, giving

$$\left| \sum_{k=1}^n e^{i\phi_k} \right| \approx \sqrt{n} \quad \text{.} \quad (2.2)$$

nearly
converged

It is desirable to obtain this state, most of the time, during operation of the imaging system.

A continuum of gaussian targets is considered; the targets are assumed to have a gaussian spatial distribution of reflectance with standard deviation σ :

$$I(x, y)_{\text{at target}} = I_0 e^{-\frac{(x^2+y^2)}{(2\sigma^2\sigma_0^2R^2)}} \quad (2.3)$$

where R is the distance to the target. The parameter σ_0 is selected so that $\sigma = 1$ corresponds to a target just resolvable by the telescope:

$$\sigma_0 = 0.8 \lambda/d \quad \text{.} \quad (2.4)$$

Table II-1 summarizes the results described in this section for the standard deviations $\sigma(\phi^*)$ of the phase-error estimators for the Hartmann test system and the pinhole interferometer, illustrated in Fig. II-1. All results given in Table II-1 must be multiplied by $1/\sqrt{I_T}$, where I_T is the light flux (expressed as photoelectrons) on a subaperture.

1. The Hartmann Test System

The Hartmann test system has four-quadrant detectors for each subaperture (Fig. II-2).

The variable proportional to x-direction tilt is taken as

$$I^x \equiv I_2 + I_4 - I_1 - I_3 \quad (2.5)$$

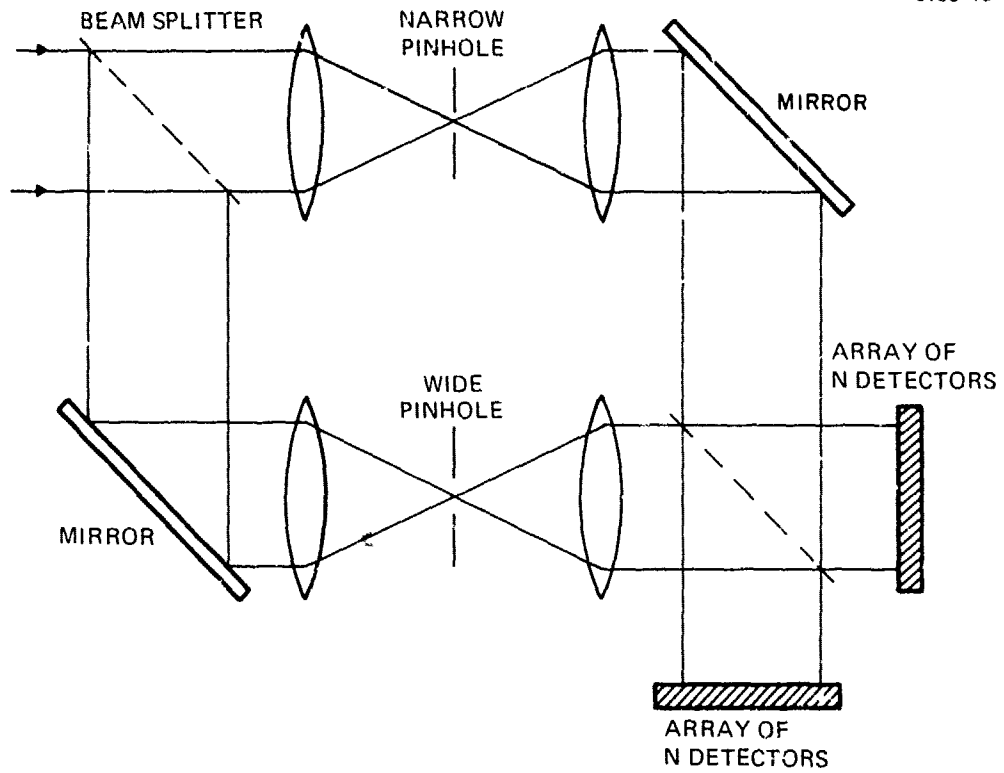


Fig. II-1. Pinhole interferometer.

Table II-1. Standard Deviations $\sigma(\phi^*)$ of the Phase-Error Estimators (Multiply all quantities by $1/\sqrt{I_T}$ where I_T is the flux on a subaperture)

	Filled Disk		Ring	
	Converged	Unconverged	Converged	Unconverged
	Case I	Case III	Case II	Case IV
<u>Hartmann</u>				
Small σ	4.5	4.5	$1.8 \sqrt{n}$	$1.8 \sqrt{n}$
Large σ	$4.5 \sigma / \sqrt{n}$	$4.5 \sigma / \sqrt{n}$	$5.7 \sigma / \sqrt{n}$	$5.7 \sigma / \sqrt{n}$
<u>Pinhole</u>				
Small σ	1	$0.45 \sqrt{n}$	1	$0.2 n$
Large σ	$0.45 \sigma \sqrt{n}$	0.64σ	$0.14 \sigma n$	0.6σ

T1839

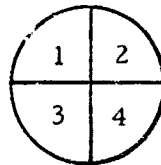


Fig. II-2. Four-quadrant detectors for each subaperture.

and for y-direction hit,

$$Y = I_1 + I_2 - I_3 - I_4 \quad (2.6)$$

(All currents are in units of photoelectrons per second.) The quantum-noise response of the system will be determined by first determining the system's best estimator ϕ_i^* for the phase error in the i th subaperture, and then calculating the standard deviation of ϕ_i^* caused by the quantum noise.

The currents I_j are then random variables having roughly gaussian distribution (the gaussian approximation to the Poisson for large numbers) with expectation $E(I_j)$ and standard deviation $\sigma(I_j) = \sqrt{E(I_j)} \approx \sqrt{I_j}$.

a. Filled-Aperture Cases (I and III)

(1) The Estimator ϕ^* - The phase error estimates ϕ_{ij}^* in the filled-aperture case are chosen to minimize the χ^2 function

$$\chi^2 \equiv \sum_{ij} \left[\left(\phi_{i,j}^{*x} - \phi_{i-1,j}^* - k_{i,j}^{yx} \right)^2 + \left(\phi_{i,j}^{*y} - \phi_{i,j-1}^* - k_{i,j}^{xy} \right)^2 \right] \quad (2.7)$$

where the subscript i, j refers to the subaperture in the i^{th} column and the j^{th} row of the filled aperture. The constant k is inversely proportional to the rate of change of

$$\begin{pmatrix} x \\ y \\ I_{i,j} \end{pmatrix}$$

with change in $\phi_{i,j}$; a small change $\Delta\phi_{i,j}$ causes a displacement of the image on detector i, j by

$$\Delta x = \frac{\lambda \ell \Delta\phi_{i,j}}{2\pi w} \quad (2.8)$$

where ℓ is the system focal length and w is the spacing between adjacent subapertures. At the detector, the image is approximately gaussian with standard deviation

$$\sigma_{\text{image}} = \ell \sigma_1 = \ell \sigma_0 \sqrt{1/v^2 + \sigma^2} = \frac{0.8 \ell \lambda}{d} \sqrt{1/v^2 + \sigma^2} \quad (2.9)$$

Here v is the ratio of the full-aperture diffraction limit to that of a subaperture. d is the diameter of the full aperture. For the filled disk,

$$v \approx 1/\sqrt{n} \quad (2.10)$$

The fluxes on detectors 2 and 4 together for our gaussian image are

$$I_2 + I_4 = I_T \int_0^\infty e^{-(u-x)^2/2(\ell\sigma_1)^2} du \left/ \int_{-\infty}^\infty e^{-(u-x)^2/2(\ell\sigma_1)^2} du \right. \quad (2.11)$$

where x is the x -coordinate of the center of the image. For small x the numerator is

$$\begin{aligned} I_T \int_0^\infty e^{-(u-x)^2/2(\ell\sigma_1)^2} du &= I_T \int_{-x}^\infty e^{-v^2/2(\ell\sigma_1)^2} dv \\ &\approx x I_T + I_T \int_0^\infty e^{-v^2/2(\ell\sigma_1)^2} dv \end{aligned} \quad (2.12)$$

since

$$\left. \frac{\partial}{\partial x} \int_{-x}^\infty e^{-v^2/2(\ell\sigma_1)^2} dv \right|_{x=0} = -e^{-v^2/2(\ell\sigma_1)^2} \Big|_0^\infty = -1 \quad (2.13)$$

So, for small x ,

$$I_2 + I_4 \approx \frac{I_T x}{\ell\sigma_1 \sqrt{2\pi}} + \frac{I_T}{2} \quad (2.14)$$

and by similar reasoning we will have

$$I_1 + I_3 = \frac{-I_T x}{\ell \sigma_1 \sqrt{2\pi}} + \frac{I_T}{2} .$$

Then

$$I_x = I_2 + I_4 - I_1 - I_3 = \frac{2I_T x}{\ell \sigma_1 \sqrt{2\pi}} . \quad (2.15)$$

The displacement $\lambda \ell \Delta \phi_{i,j} / 2\pi w$ of an initially centered image then gives output change

$$\Delta I^x = \frac{2I_T}{\ell \sigma_1 \sqrt{2\pi}} \cdot \frac{\lambda \ell \Delta \phi}{2\pi w} = \frac{2\lambda I_T \Delta \phi}{\sigma_1 w (2\pi)^{3/2}} . \quad (2.16)$$

The constant k then is

$$k = \frac{\Delta \phi}{\Delta I^x} = \frac{\sigma_1 w (2\pi)^{3/2}}{2\lambda I_T} . \quad (2.17)$$

For the filled aperture, $w \approx d/\sqrt{n}$, so eqs. (2.9) and (2.17) combine to give

$$\begin{aligned} k_{\text{cases I and III}} &\approx \frac{6.3 \sqrt{\sigma_e^2 + \sigma^2}}{\sqrt{n} I_T} \\ &= \frac{6.2 \sqrt{n + \sigma^2}}{\sqrt{n} I_T} \end{aligned} \quad (2.18)$$

using eq. (2.10) with $\sigma_e = 1/v = \sqrt{n}$.

In eq. (2.7) χ^2 is minimized when the $\phi_{i,j}^*$ are chosen so that

$$\begin{aligned} \phi_{i,j}^* = 1/4 & \left(\phi_{i-1,j} + kI_{i,j}^x + \phi_{i+1,j} - kI_{i+1,j}^x \right. \\ & \left. + \phi_{i,j-1} + kI_{i,j}^y + \phi_{i,j+1} + kI_{i,j+1}^y \right) \end{aligned} \quad (2.19)$$

(with the absence of appropriate terms at the boundaries).

This implicit set of equations can be solved for each $\phi_{i,j}^*$ explicitly as a linear function of the I^x 's and I^y 's. The linear operator M giving the solution is local and position-independent (except near the boundaries):

$$\phi_{i,j}^* \approx k \sum_{k,l} \left(M_{i-k,j-l} I_{k,l}^x + M_{j-l,i-k} I_{k,l}^y \right) \quad (2.20)$$

Table II-2 gives our computer calculation of M.

Table II-2. Values of $M_{k,l}$ for eq. (2.20)

-0.04	-0.03	-0.02	-0.01	0.01	0.02	0.03	0.04	3
-0.04	-0.04	-0.04	-0.03	0.03	0.04	0.04	0.04	2
-0.05	-0.05	-0.06	-0.07	0.07	0.06	0.05	0.05	1
-0.05	-0.07	-0.11	-0.25	0.25	0.11	0.07	0.05	0
-0.05	-0.05	-0.06	-0.07	0.07	0.06	0.05	0.05	-1
-0.04	-0.04	-0.04	0.03	0.03	0.04	0.04	0.04	-2
-0.04	-0.03	-0.02	-0.01	0.01	0.02	0.03	0.04	-3
-3	-2	-1	0	1	2	3	4	

K

(2) Standard Deviation of ϕ^* - The fluctuations of the estimators ϕ^* due to quantum noise will now be determined. Assuming the atmospheric phase errors are frozen and the system collects I_T photoelectrons per subaperture, the standard deviations of the system's estimates $\phi_{i,j}^*$ of the atmospheric errors are calculated.

The standard deviations of each I^x and I^y are all $\sqrt{I_T}$ since each subaperture generates I_T photoelectrons. The standard deviation of $\phi_{i,j}^*$ is then [using Eq. (2.20)]

$$\begin{aligned} \sigma(\phi_{i,j}^*) &\approx k \left[\sum_{k,l} (M_{i-k,j-l}^2 + M_{j-l,i-k}^2) \right]^{1/2} \sqrt{I_T} \\ &= k \left[2 \sum_{k,l} M_{k,l}^2 \right]^{1/2} \sqrt{I_T} \\ &= k [2 \times 0.26]^{1/2} \sqrt{I_T} = 4.5 \sqrt{1 + \sigma^2/n} \sqrt{I_T}, \quad (2.21) \end{aligned}$$

since $\sum_{k,l} M_{k,l}^2 = 0.26$. This result is independent of the degree of convergence of the system.

b. Ring Aperture Cases (II and IV) - The χ^2 to be minimized is

$$\chi^2 = \sum_i (\phi_i - \phi_{i-1} - kI_i)^2 \quad (2.22)$$

Here i indexes position around the circle and I_i is the tilt in the tangential direction (compare with I^x , I^y). This χ^2 is minimized by the solution

$$\phi_i = k \sum_k Q_k I_{i+k} \quad (2.23)$$

where the kernel Q is

$$Q_k \equiv \begin{cases} \frac{1}{2} - \frac{k}{n} & \frac{n}{2} \geq k > 0 \\ -\frac{1}{2} - \frac{k-1}{n} & -\frac{n}{2} < k \leq 0 \end{cases} \quad (2.24)$$

The quantity $\sum_k Q_k^2$ is

$$\sum_k Q_k^2 \approx \frac{n}{12} \quad (2.25)$$

For the ring aperture, we have $v \approx \pi/n$ and $w \approx \pi d/n$. Equation (2.17) then gives

$$k = \frac{0.8\pi(2\pi)^{3/2} \sqrt{n^2/\pi^2 + \sigma^2}}{2n I_T} = \frac{19.7}{n I_T} \sqrt{n^2/\pi^2 + \sigma^2} \quad .$$

The standard deviation of ϕ^* , using the same reasoning as in the previous section, is then

$$\sigma(\phi_i^*) \approx k \sqrt{\sum_i Q_i^2} \sqrt{I_T} = 5.7 \sqrt{n/\pi^2 + \sigma^2/n} \sqrt{I_T} \quad , \quad (2.26)$$

again independent of the degree of convergence of the system.

2. The Pinhole Interferometer System

Figure II-1 illustrates the pinhole interferometer. The narrow pinhole has diameter $d_n = 2.44\lambda l/d$, the diameter of the telescope's Airy disk. Focal length of the telescope is l and d is the diameter of the telescope aperture. The wide pinhole has diameter $d_w = v d_n$ where

$$v = \begin{cases} \sqrt{n} & \text{for the filled disk} \\ n/\pi & \text{for the ring.} \end{cases} \quad (2.27)$$

We let θ be the fraction of light in each subaperture that is sent to the signal beam, i. e., θ is the reflectivity of S_1 . Assuming S_1 does not absorb, the light in the reference beam in the disk aperture cases is then $n(1 - \theta) I_T$. We will not treat the case that the light inside the ring is used in the reference beam.

The amount of light penetrating the narrow pinhole is $n I_n$. This is the light incident on the pinhole multiplied by the fraction of the gaussian image falling on the circular opening of pinhole. This fraction is obtained by a geometric-optics calculation: For our four cases this is

$$n I_n \approx \begin{cases} \frac{(1 - \theta) n I_T}{1.2 + 0.8 \sigma^2} & \text{Case I} \\ \frac{(1 - \theta) n I_T}{1.2 + 0.8 \sigma^2} & \text{Case II} \\ \frac{(1 - \theta) n I_T}{0.8 \sigma^2 + 0.8 n} & \text{Case III} \\ \frac{(1 - \theta) n I_T}{0.8 \sigma^2 + 0.8 n^2/\pi^2} & \text{Case IV} \end{cases} \quad (2.28)$$

(The cases here and in the following are those defined at the beginning of this section.)

The amount of light penetrating the wide pinhole is, again from the geometry,

$$n I_w \approx \begin{cases} \frac{n\theta I_T}{1 + 0.8 \sigma^2/n} & \text{Cases I and III} \\ \frac{n\theta I_T}{1 + 0.8 \sigma^2 \pi^2/n^2} & \text{Cases II and IV} \end{cases} \quad (2.29)$$

We have used approximating fractions in place of the exact functions for I_n and I_w .

a. Depth of Modulations — The degree of interferometer modulation I_m is defined here as the peak value of the sinusoidal variation of interferometer output with path length difference. The expected outputs 1 and 2 of the interferometer for channel i are

$$E\left(I \begin{Bmatrix} 1 \\ 2 \end{Bmatrix}\right) = \frac{1}{2} \left[I_n + I_w \{\pm\} I_m \sin\left(\frac{2\pi \nu \Delta}{C} - \pi/2\right) \right] \quad (2.30)$$

where Δ is pathlength difference and ν is the frequency of light. We will introduce a fixed $\pi/2$ path length difference in one arm so that the zero-phase-error condition will give equal outputs in the two photomultipliers. So the actual phase error will be $\phi = 2\pi \nu \Delta / C - \pi/2$.

The appendix derives I_m for our four cases and for small σ and large σ . Table II-3 summarizes these results. The transition from small σ to large σ takes place between $\sigma = 1$ and $\sigma = \nu$.

Table II-3. Evaluation of I_m

	Cases I and II	Cases III and IV
Small σ	$2 \sqrt{I_w I_n}$	$2 \sqrt{I_w I_n}$
Large σ	$(2/\nu) \sqrt{I_w I_n}$	$1.4 \sqrt{I_w I_n}$

b. The Estimator ϕ_i^* - Our estimator for phase error for subaperture i will be proportional to the difference in output of that subaperture's photomultipliers:

$$\phi_i^* = k(I_i^1 - I_i^2) \quad (2.31)$$

Then from (2.30), we have

$$E(\phi_i^*) = k I_m \sin \phi_i \quad , \quad (2.32)$$

so k must be $1/I_m$ for ϕ_i^* to be the proper estimator near zero.

c. Standard Deviation of ϕ_i^* - The standard deviation of ϕ_i^* (from 2.31) is

$$\begin{aligned} \sigma(\phi_i^*) &= \sqrt{\sigma^2(I_i^1) + \sigma^2(I_i^2)} / I_m = \sqrt{I_i^1 + I_i^2} / I_m \\ &= \sqrt{I_n + I_w} / I_m \quad . \quad (2.33) \end{aligned}$$

For all four cases and for all target widths σ , the smallest obtainable $\sigma(\phi_i^*)$ can be found by combining eqs. (2.28), (2.29), and (2.33) and Table II-3, and choosing θ to minimize the resulting calculated $\sigma(\phi_i^*)$.

For simplicity, we will do this for all four cases and for small and large σ but not for the middle range of σ .

Small σ

Here we assume $\sigma < 1$. Then

$$\sigma(\phi_i^*) \approx \left\{ \begin{array}{ll} \sqrt{\frac{0.8 + 0.2 \theta}{3.2 \theta (1 - \theta) I_T}} & \text{Case I} \\ \sqrt{\frac{0.8 + 0.2 \theta}{3.2 \theta (1 - \theta) I_T}} & \text{Case II} \\ \sqrt{\frac{1 + 0.8 n \theta}{4 \theta (1 - \theta) I_T}} & \text{Case III} \\ \sqrt{\frac{1 + ((0.8/\pi^2) n^2 - 1) \theta}{4 \theta (1 - \theta) I_T}} & \text{Case IV} \end{array} \right. \quad (2.34)$$

The following gives the θ . For Case III we also give a practical θ assuming that mirror reflectivity cannot change during convergence. The resulting $\sigma(\phi_i^*)$ are given.

	<u>θ</u>	<u>$\sigma(\phi_i^*)$</u>
Case I	0.5	$1/\sqrt{I_T}$
Case II	0.5	$1/\sqrt{I_T}$
Case III	$\frac{1.1}{\sqrt{n}}$ (optimum)	$0.45 \sqrt{n}/\sqrt{I_T}$
	0.5 (practical)	$0.6 \sqrt{n}/\sqrt{I_T}$
Case IV	0.5	$\sqrt{0.5(1 + 0.08 n^2)}/\sqrt{I_T}$ (2.35)

Large σ : $\sigma > n$

$$\sigma(\phi_i^*) \approx \left\{ \begin{array}{ll} \sigma \sqrt{\frac{1 + n \theta}{5. \theta (1 - \theta) I_T}} & \text{Case I} \\ \frac{\sigma}{2\pi} \sqrt{\frac{\theta(n^2 - \pi^2) + \pi^2}{1.2 \theta (1 - \theta) I_T}} & \text{Case II} \\ \sqrt{\frac{\sigma^2 \left(\theta + \frac{1 - \theta}{n} \right) + n\theta}{2.4 \theta (1 - \theta) I_T}} & \text{Case III} \\ \sqrt{\frac{\sigma^2 \left[\theta + (1 - \theta) \frac{\pi^2}{n^2} \right] + n^2 \theta / \pi^2}{2.4 \theta (1 - \theta) I_T}} & \text{Case IV} \end{array} \right. \quad (2.36)$$

As in the previous subsection, we give optimum values of θ for $\sigma(\phi_i^*)$.

Large σ

	<u>θ</u>	<u>$\sigma(\phi_i^*)$</u>
Case I	$1/\sqrt{n}$	$0.45 \sigma \sqrt{n}/\sqrt{I_T}$
Case II	π/n (no use of central light)	$0.14 \sigma n/\sqrt{I_T}$
Case III	$1/\sqrt{n}$	$0.64 \sigma / \sqrt{I_T}$
Case IV	π/n	$0.6 \sigma \sqrt{1 + 3.1/n}/\sqrt{I_T} \quad (2.37)$

B. Wavefront Correction with a Pinhole Interferometer for an Extended Target

Our analysis of the pinhole interferometer has led us to conclude that there is insufficient information obtained from the measurements to perform wavefront correction, when viewing an extended object or a multiple point source target. An assessment of the analysis given below is that too much information must be known about the target or obtained from the data to do wavefront correction. The number of point sources, their relative brightness, and their positions with respect to each other over the integration period must be known in order to estimate the wavefront distortion. These parameters will all be changing as the satellite rotates in its orbit and can directly introduce significant error in the wavefront phase error estimate.

Figure II-1 illustrates the optical setup and coordinates system for the analysis of the multiple point source target. Assume the target is characterized as

$$f(x, y) = \sum_{n=1}^N A_n \delta(x - x_n, y - y_n) \quad (2.38)$$

where A_n is the amplitude and (x_n, y_n) is the position of point source n . The amplitude at the telescope aperture prior to traversing the phase screen is given by

$$F(u, v) = \mathcal{F}[f(x, y)] = \sum_{n=1}^N A_n e^{-i\ell(\underline{u} \cdot \underline{x}_n)} \quad (2.39)$$

where $\underline{u} = (u, v)$, $\underline{x}_n = (x_n, y_n)$, ℓ is a scale factor and \mathcal{F} is the Fourier transform operator. The phase screen at the aperture introduces the phase function

$$\begin{aligned}
F_1(u, v) &= F(u, v) e^{i\psi(u, v)} \\
&= \mathcal{F}^{-1} [f(-x, -y) \otimes \Psi(-x, -y)] \\
&= \mathcal{F}^{-1} [f(x, y) \otimes \Psi(x, y)] \quad , \quad (2.40)
\end{aligned}$$

where we define the function

$$\Psi(x, y) = \mathcal{F}^{-1} [e^{i\psi(u, v)}] \quad (2.41)$$

and note the Fourier transform of the product of two Fourier transform functions is the convolution of the original two functions. The optical wavefronts from the beam splitter impinging on each of the pinholes in planes P_2 and P_2' is given by

$$\begin{aligned}
f_i'(x', y') &= a_i \mathcal{F}[F_1(u, v)] & i = 1 \text{ for plane } P_2 \\
&= a_i f(x, y) \otimes \Psi(x, y) & i = 2 \text{ for plane } P_2' \\
& & 0 < a_i < 1 \\
&= a_i \sum_{n=1}^N A_n \Psi(x' - x_n, y' - y_n) & (2.42)
\end{aligned}$$

The wavefront transmitted through the wide pinhole (assuming no spatial filtering of the target image) to plane P_3 is

$$\begin{aligned}
F_1'(u', v') &= \mathcal{F}[f_1'(x', y')] \\
&= a_1 \sum_{n=1}^N A_n e^{+i\ell(\underline{u}' \cdot \underline{x}_n) + i\psi(\underline{u}')} \quad . \quad (2.43)
\end{aligned}$$

The wavefront transmitted by the small pinhole at plane P_2^1 , is

$$\begin{aligned} f_2''(\mathbf{x}', y') &= a_3 f_2'(\mathbf{x}', y') \delta(\mathbf{x}', y') \\ &= a_2 a_3 \left[\sum_{n=1}^N A_n \Psi(\mathbf{x}' - \mathbf{x}_n, y' - y_n) \right] \delta(\mathbf{x}', y') \quad . \quad (2.44) \end{aligned}$$

The optical wavefront $f_2''(\underline{\mathbf{x}}')$ propagated to plane P_3 is

$$\begin{aligned} F_2'(\underline{u}', v') &= \mathcal{F}[f_2''(\mathbf{x}', y')] \\ &= a_4 \sum_{n=1}^N A_n \Psi(-\mathbf{x}_n, -y_n) \\ &= \sum_{n=1}^N B_n \quad \text{with } B_n = a_4 A_n \Psi(-\mathbf{x}_n, -y_n) \quad . \quad (2.45) \end{aligned}$$

The optical intensity at a detector in plane P_3 with position $\underline{\mathbf{u}}' = (u', v')$ is

$$\begin{aligned} I_1(\underline{\mathbf{u}}') &= \left\langle \left[F_1'(\underline{\mathbf{u}}') + F_2'(\underline{\mathbf{u}}') \right] \left[F_1'(\underline{\mathbf{u}}') + F_2'(\underline{\mathbf{u}}') \right]^* \right\rangle \\ &= \sum_{n=1}^N \left[\left| a_1 A_n \right|^2 + \left| B_n \right|^2 + a_1 A_n B_n^* e^{+i\ell \underline{\mathbf{u}}' \cdot \underline{\mathbf{x}}_n + i\psi} \right. \\ &\quad \left. + a_1 A_n^* B_n e^{-i\ell \underline{\mathbf{u}}' \cdot \underline{\mathbf{x}}_n - i\psi} \right] \quad (2.46) \end{aligned}$$

since each of the point sources is incoherent and has zero mutual intensity. If we re-express

$$\Psi(-\underline{x}_n) \triangleq \Psi_n e^{-i\theta_n}, \quad \text{with } \Psi_n = \Psi_n^*,$$

then

$$I_1(\underline{u}') = \sum_{n=1}^N |A_n|^2 \left[a_1^2 + a_4^2 \Psi_n^2 + 2a_1 a_4 \Psi_n \cos(\psi(\underline{u}') + \theta_n + \ell \underline{u}' \cdot \underline{x}_n) \right]. \quad (2.47)$$

By a similar analysis, the optical intensity at a detector in plane P_3' at position \underline{u}' , due to a phase shift of $\pi/2$ radians in the function $F_2'(\underline{u}')$ is given by

$$\begin{aligned} I_2(\underline{u}') &= \left\langle \left[F_1'(\underline{u}') + F_2'(\underline{u}') e^{i\pi/2} \right] \left[F_1'(\underline{u}') + F_2'(\underline{u}') e^{i\pi/2} \right]^* \right\rangle \\ &= \sum_{n=1}^N |A_n|^2 \left[a_1^2 + a_4^2 \Psi_n^2 + 2a_1 a_4 \Psi_n \cos(\psi(\underline{u}') + \theta_n - \pi/2 + \ell \underline{u}' \cdot \underline{x}_n) \right] \\ &= \sum_{n=1}^N |A_n|^2 \left[a_1^2 + a_4^2 \Psi_n^2 + 2a_1 a_4 \Psi_n \sin(\psi(\underline{u}') + \theta_n + \ell \underline{u}' \cdot \underline{x}_n) \right]. \end{aligned} \quad (2.48)$$

If we design the optical system so that $a_1 = a_4$,

$$I_2(\underline{u}') = a_1^2 \sum_{n=1}^N |A_n|^2 \left[1 + \Psi_n^2 + 2\Psi_n \sin(\psi(\underline{u}') + \theta_n + \ell \underline{u}' \cdot \underline{x}_n) \right]$$

$$I_1(\underline{u}') = a_1^2 \sum_{n=1}^N |A_n|^2 \left[1 + \Psi_n^2 + 2\Psi_n \cos(\psi(\underline{u}') + \theta_n + \ell \underline{u}' \cdot \underline{x}_n) \right]$$

(2.49)

It would greatly aid us in the estimation of $\psi(\underline{u}')$ if we knew the number of point sources, N , their amplitudes, A_n , and their positions $\underline{x}_n = (x_n, y_n)$, $n = 1, 2, \dots, N$. An additional difficulty with the ambiguity in the estimate of $\psi(\underline{u}')$ can be demonstrated easily for the case $N = 1$. Assume that $\Psi_1 = 1$ and $\underline{x}_1 = \theta_1 = 0$. Then

$$I_2(\underline{u}') = 2a_1^2 |A_1|^2 [1 + \sin \psi(\underline{u}')] \quad (2.50)$$

$$I_1(\underline{u}') = 2a_1^2 |A_1|^2 [1 + \cos \psi(\underline{u}')] \quad (2.51)$$

and

$$\frac{I_2}{I_1}(\underline{u}') = \frac{1 + \sin \psi(\underline{u}')}{1 + \cos \psi(\underline{u}')} \quad (2.52)$$

has values for ψ in the interval $-\pi/2 \leq \psi < \pi$ and $\pi < \psi \leq 3\pi/2$ for any given value of I_2/I_1 . The ambiguities become more complicated as N increases. Confronted with the intractable form of the parameter ψ to be estimated in the data $\{I_1, I_2(\underline{u}')\}_{\underline{u}'}$, we have discarded the pinhole interferometer as a candidate for predetection compensation.

C. Computer Evaluation of Wavefront Correction With Image Quality Detectors

1. Introduction

An analytic computer simulation has been used to evaluate the performance characteristics of image quality improvement measuring integral of intensity through a pinhole matched to the Airy disk size and integral of intensity squared. The computer simulation models a 48 in. telescope viewing a point source (in the far field) through a phase screen directly in front of the telescope. Using the design philosophy of minimizing system costs where possible, 32 piston corrector mirror elements, arranged in an annulus on the primary, relay the incident illumination to the single image quality detector.

Each of the mirror elements is 10 cm x 10 cm in size and can be shifted forward or backward individually or in synchrony with all other mirror elements to phase up the distorted wavefront incident on the primary aperture. The phase screen model used to distort the wavefront is generated by a fast Fourier transform technique which yields a two-dimensional distribution of gaussian random numbers having correlation properties consistent with those associated with Kolmogorov turbulence. The strength of the phase screen is an input parameter to the computer simulation.

Other parameter inputs to the computer simulation include

- The number of target generated photoelectrons per mirror element per image measurement
- The size and position of the detector in the focal plane
- The image quality criterion, either integral of intensity through the pinhole (if index SEXP = 1) or integral of the squared intensity (if index SEXP = 2).
- An index parameter specifying that phase compensation is to be performed one element at a time in sequence or with half the elements simultaneously, in sequence.

A flowchart of the computer simulation is shown in Fig. II-3.

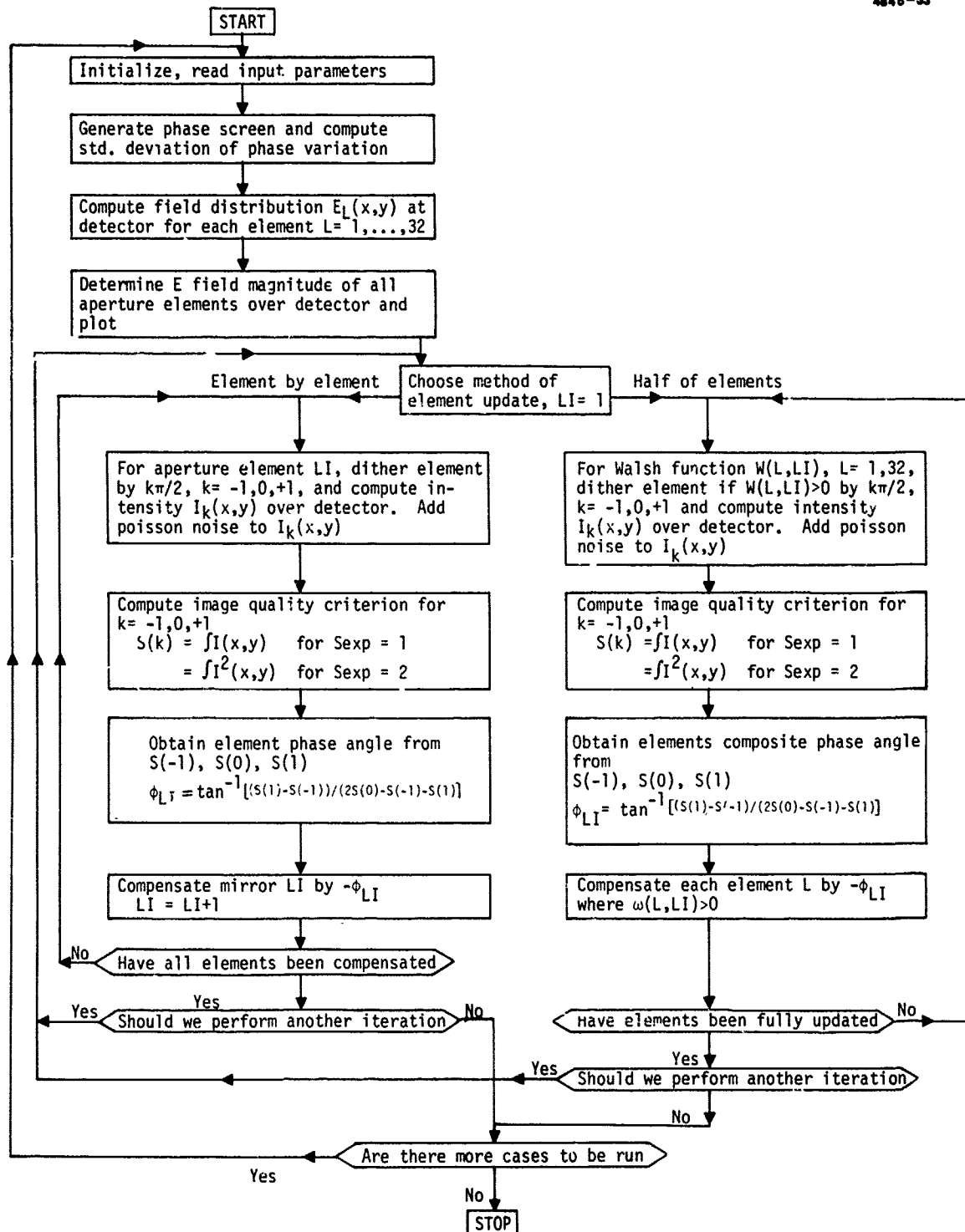


Fig. II-3. Flow chart for predetection compensation with 32 piston elements and image quality detectors.

2. Principle of Operation

The following discussion will illustrate the principle of phase compensation for the element-by-element method and the elements by halves method for the integral of intensity through a pinhole image quality detector. A discussion of the simulation results will conclude the section.

The element-by-element method of phase compensation for N elements holds $N-1$ elements constant and dithers one element $+\lambda/4$ and $-\lambda/4$ wavelengths (or $+\pi/2$ radians) to estimate the phase deviation ϕ between the average phase over the $N-1$ elements and the phase of the remaining element.

Taking E_T as the resultant electric field over the $N-1$ elements and E_1 as the field over the remaining element, and ϕ as the phase angle between the fields (Fig. II-4), the undithered intensity is given by

$$I_0 = E_T^2 + E_1^2 + 2E_1 E_T \cos \phi \quad (2.53)$$

Shifting the element forward to introduce $\pi/2$ radius phase shift,

$$\begin{aligned} I_1 &= E_T^2 + E_1^2 + 2E_1 E_T \cos(\phi + \pi/2) \\ &= E_T^2 + E_1^2 - 2E_1 E_T \sin \phi \end{aligned} \quad (2.54)$$

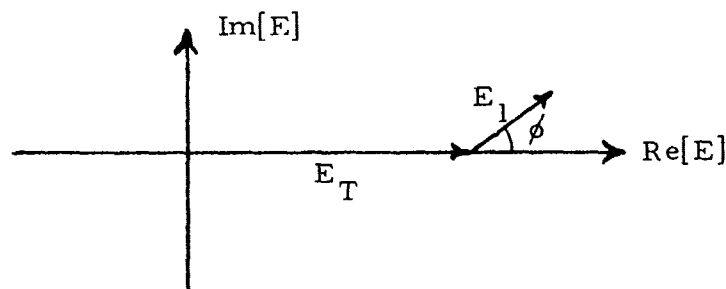


Fig. II-4. Phasor diagram for the electric fields using the element by element method.

Shifting the element back for $-\pi/2$ radians phase shift yields

$$I_{-1} = E_T^2 + E_1^2 + 2E_1 E_T \sin \phi \quad (2.55)$$

Note that a good estimator for ϕ is

$$\hat{\phi} = \tan^{-1} \left[\frac{I_{-1} - I_1}{2I_0 - I_1 - I_{-1}} \right] \quad (2.56)$$

The elements by halves method of compensation for N elements employs as many measurements as the element-by-element method but obtains an improved signal-to-noise ratio by increasing the modulation of the dithered intensity. The method of implementation chosen here is to sequence through each of the Walsh functions W_{LI} , $LI = 2, \dots, 32$, for as many elements as are to be compensated. All of the L lens elements, $L = 1, \dots, 32$, will be shifted $+\pi/2$ for one measurement and $-\pi/2$ for the next measurement if the value of the Walsh function $W_{LI}(L) > 0$. Otherwise, the element is not shifted.

The measured phase deviation $\hat{\phi}_{LI}$, described below, is used to compensate each of the elements L whose Walsh function value $W_{LI}(L) > 0$.

To illustrate the by halves estimation process, assume each element has a constant electric field strength E_0 and phasor θ_ℓ , for elements $\ell = 1, 2, \dots, 32$ (Fig. II-5). The intensity seen at the detector is

$$\begin{aligned} I &= \left| E_0 \sum_{\ell=1}^N e^{i\theta_\ell} \right|^2 \\ &= |E_0|^2 \left[N + 2 \sum_{\ell=1}^N \sum_{m=\ell+1}^N \cos(\theta_\ell - \theta_m) \right] \end{aligned} \quad (2.57)$$

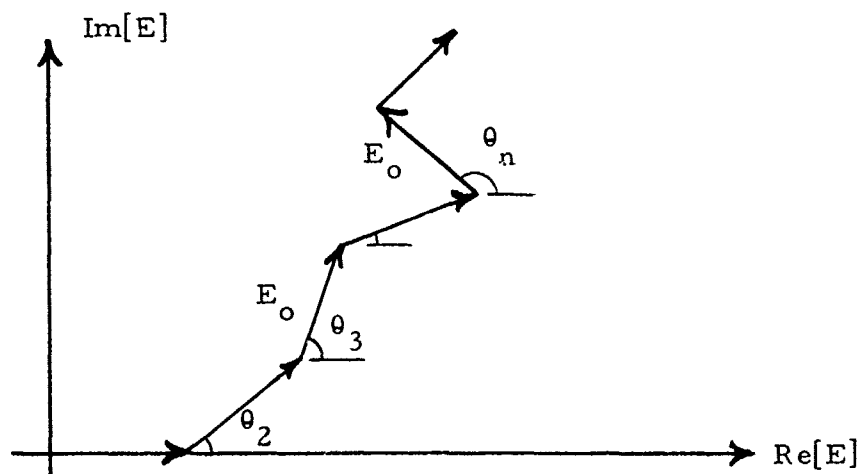


Fig. II-5. Phasor diagram for the electric fields using the elements by halves method.

To compute the intensity for step Ll in the sequence, $Ll = 1, \dots, 31$, some elements are dithered by $\pi/2$. Let J_1 be an index set with $j_1 \in J_1$ iff element j_1 is dithered. Let J_2 be an index set with $j_2 \in J_2$ iff element j_2 is not dithered. We are using the connection "iff" for "if and only if."

$$\begin{aligned}
 I(+\pi/2) = & \left| E_0 \right|^2 \left[N + \sum_{j_1 \in J_1} \sum_{\substack{k_1 \in J_1 \\ k_1 \neq j_1}} \cos(\theta_{j_1} - \theta_{k_1}) \right. \\
 & + \sum_{j_2 \in J_2} \sum_{\substack{k_2 \in J_2 \\ k_2 \neq j_2}} \cos(\theta_{j_2} - \theta_{k_2}) \\
 & \left. - 2 \sum_{j_1 \in J_1} \sum_{j_2 \in J_2} \sin(\theta_{j_1} - \theta_{j_2}) \right] \quad (2.58)
 \end{aligned}$$

Illustration of the elements by halves method is done most easily for the linearized case with θ_j small, $j = 1, \dots, 32$. It can easily be shown that for this case

$$I_{J_1} (+\pi/2) = N |E_o|^2 \left[\frac{N}{2} - \left\langle \sum_{j_1 \in J_1} \theta_{j_1} - \sum_{j_2 \in J_2} \theta_{j_2} \right\rangle \right] \quad (2.59)$$

and

$$I_{J_1} (-\pi/2) = N |E_o|^2 \left[\frac{N}{2} + \left\langle \sum_{j_1 \in J_1} \theta_{j_1} - \sum_{j_2 \in J_2} \theta_{j_2} \right\rangle \right] \quad (2.60)$$

Note that the phase estimator at small phase angles yields

$$\begin{aligned} \hat{\phi}_{J_1} &= \frac{N \left[I_{J_1} (-\pi/2) - I_{J_1} (+\pi/2) \right]}{2 \left[I_{J_1} (-\pi/2) + I_{J_1} (+\pi/2) \right]} = \frac{N \left[I_{J_1} (-\pi/2) - I_{J_1} (+\pi/2) \right]}{2 \left[2I_{J_1} (0) - I_{J_1} (-\pi/2) - I_{J_1} (\pi/2) \right]} \\ &= \left\langle \sum_{j_1 \in J_1} \theta_{j_1} - \sum_{j_2 \in J_2} \theta_{j_2} \right\rangle \quad (2.61) \end{aligned}$$

An example will suffice to illustrate how these measurements are used for phase compensations. Consider the case for $N = 4$. The Walsh functions for $N = 4$ are illustrated in Fig. II-6. For $W(m, 2)$, $J_1 = \{3, 4\}$ and $\hat{\phi}_{J_1}$ is denoted $\hat{\phi}_2$. For $W(m, 3)$, $J_1 = \{2, 3\}$ and $\hat{\phi}_{J_1}$ is denoted $\hat{\phi}_3$. For $W(m, 4)$, $J_1 = \{1, 3\}$ and $\hat{\phi}_{J_1}$ is denoted $\hat{\phi}_4$. We will also define a dummy variable $\hat{\phi}_1$ to ease manipulation of the variables. For $\hat{\phi}_1$, let $J_1 = \{1, 2, 3, 4\}$ as would be the case for $W(m, 1)$.

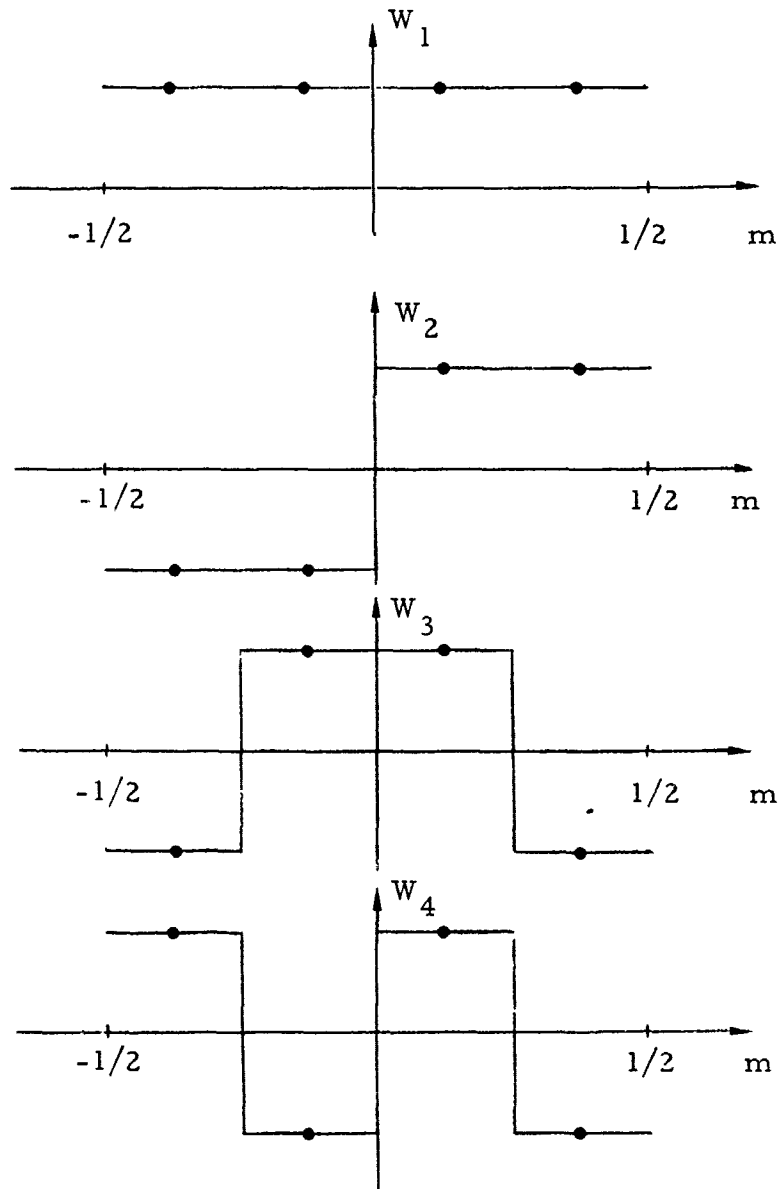


Fig. II-6. Walsh Functions (1, 2, 3, 4).

Thus, we obtain $\hat{\phi} = A\theta$

$$\begin{bmatrix} \hat{\phi}_1 \\ \hat{\phi}_2 \\ \hat{\phi}_3 \\ \hat{\phi}_4 \end{bmatrix} = \begin{bmatrix} 1 & 1 & 1 & 1 \\ -1 & -1 & 1 & 1 \\ -1 & 1 & 1 & -1 \\ 1 & -1 & 1 & -1 \end{bmatrix} \cdot \begin{bmatrix} \theta_1 \\ \theta_2 \\ \theta_3 \\ \theta_4 \end{bmatrix} \quad (2.62)$$

By the orthogonality of Walsh functions, $A^{-1} = A^T$, i. e., $\theta = A^T \hat{\phi}$, and

$$\begin{bmatrix} \theta_1 \\ \theta_2 \\ \theta_3 \\ \theta_4 \end{bmatrix} = \begin{bmatrix} 1 & -1 & -1 & 1 \\ 1 & -1 & 1 & -1 \\ 1 & 1 & 1 & 1 \\ 1 & 1 & -1 & -1 \end{bmatrix} \begin{bmatrix} \hat{\phi}_1 \\ \hat{\phi}_2 \\ \hat{\phi}_3 \\ \hat{\phi}_4 \end{bmatrix} \quad (2.63)$$

We can reference all θ to one θ_1 , e. g., θ_1 . By matrix manipulation, we obtain an expression that does not use the first Walsh function, namely,

$$\begin{bmatrix} \theta_2 \\ \theta_3 \\ \theta_4 \end{bmatrix} = \begin{bmatrix} 0 & 2 & -2 \\ 2 & 2 & 0 \\ 2 & 0 & -2 \end{bmatrix} \begin{bmatrix} \hat{\phi}_2 \\ \hat{\phi}_3 \\ \hat{\phi}_4 \end{bmatrix} \quad (2.64)$$

Thus, the measured values $\hat{\phi}_2, \hat{\phi}_3, \hat{\phi}_4$ permit us to estimate the phase angles $\theta_i, i = 2, \dots, 4$, for correction. Consequently, given N elements, only $N-1$ Walsh functions need be used in the elements by halves method.

3. Computer Simulation Results

Tables II-4 and 5 summarize the results obtained for the cases of interest that were examined. Table II-4 presents the results using the integral of the intensity through a pinhole matched to the Airy disk as the image quality sensor. The results are tabulated as a function of NPE, the number of photoelectrons generated per element area per measurement. The results in each table list the ratio of peak intensity on the detector to the maximum possible intensity, prior to correction and after one complete iteration to update all 32 elements.

The trends of the results are evident for both the element-by-element method and the elements by halves method. The element-by-element method does not appear to converge (with Poisson noise at the detector) for $NPE < 500$ photoelectrons/element area/measurement with either image quality sensor. The elements by halves method appears to work significantly better for both image quality sensors, being able to converge until NPE is reduced to 100 or 150 photoelectrons/element area/measurement. These results are not cause for optimism for the elements by halves method since it does require a large number of photoelectrons/iteration to update the elements.

Table II-4. Ratio of Peak/Maximum Possible Intensity With No Correction and After One Iteration Using the Integral of Intensity Squared Detector. Standard deviation of phase screen = 1.17 radians. NPE is number of photoelectrons/100 cm² element/measurement.

NPE	Element by Element Method	N Elements by Halves Method
1000	0.34 → 0.50	0.34 → 0.62
500	0.34 → 0.33	0.34 → 0.52
250	—	0.34 → 0.50
125	—	0.34 → 0.44
100	—	0.34 → 0.29
75	—	0.34 → 0.22

Table II-5. Ratio of Peak/Maximum Possible Intensity Prior to Correction and After One Iteration Using the Integral of Intensity Through a Pinhole Detector. NPE is number of photoelectron/100 cm² element/measurement.

NPE	Element by Element $\phi_{\text{Std dev}} = 1.17 \text{ rad}$	N Element by Halves		
		$\phi_{\text{Std dev}} = 1.17 \text{ rad}$	$\phi_{\text{Std dev}} = 1.37 \text{ rad}$	$\phi_{\text{Std dev}} = 1.56 \text{ rad}$
		1000	0.34 → 0.47	0.34 → 0.89
500	0.34 → 0.27	0.34 → 0.84		
250			0.27 → 0.61	0.25 → 0.47
200			0.27 → 0.62	0.25 → 0.38
150			0.27 → 0.35	0.25 → 0.22
125			0.27 → 0.42	0.25 → 0.18
100			0.27 → 0.25	0.25 → 0.19

As a brief example, the minimum number of photoelectrons for one iteration of 32 elements with the elements by halves method can be taken as (31 Walsh functions) (3 measurements/Walsh function) (100 PE/element area/measurement) = 9300 photoelectrons/iteration with the elements having an element area of 100 cm^2 . This required number of photoelectrons for this method is much higher than the number available for many of the objects of interest and is cause for us to attempt to reduce this required photoelectron count. Our improved method of aperture correction, multiple aperture interlinked (MAIL), is described in Section IV.

III. DEFORMABLE MIRROR DESIGN

In the initial period of this compensated imaging program, a portion of our effort was placed on the design of deformable mirrors for image correction and dither. This effort was not carried to completion because of program redirection to emphasize theoretical evaluation of the candidate predetection compensated imaging concept. Deformable mirror design is emphasized because it offers better phase error correction for a given number of actuators than the segmented mirror and it also allows the incorporation of a number of performance features not compatible with monolithic designs. The degree of development of deformable mirror technology makes it the first choice for phase correction in our system concepts. Because of its superior voltage sensitivity, accurate approximation to the desired surface figure, compatibility with simple cooling arrangements (if required by actuator dissipation), and state of development, the deformable mirror driven by a set of discrete actuators is our prime candidate for a combined dither/phase corrector at present.

The following topics will be discussed in this section:

- Surface figure
- Resonant modes
- Interactuator coupling
- Assembly techniques

Figure III-1 is a 54-element experimental Imaging-COAT prototype mirror assembled prior to this contract to test several aspects of a simple, high actuator density design. A thin, relatively flexible glass faceplate is supported by an array of actuator heads, which are in turn supported by hollow cylindrical PZT actuators. Figure III-1(b) shows the mirror figure as obtained after initial polishing. Several polishing techniques were tested, but no attempt was made to make this a thermally stable structure.

Figure III-2 shows a deformable mirror delivered to the Navy by Hughes for phase correction at $10.6 \mu\text{m}$ in a high power laser system. For high power, cooled, deformable mirrors for $10.6 \mu\text{m}$, the continuous surface mirror actuated by discrete piezoelectric or hydraulic actuators is the favored approach.

4134-0

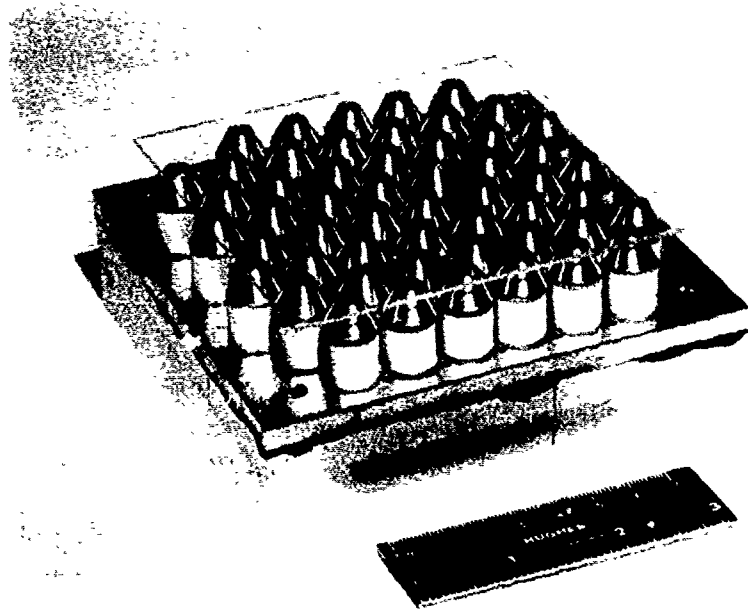


Fig. III-1(a). Sixty-four element I-COAT deformable mirror prototype.

4134-53

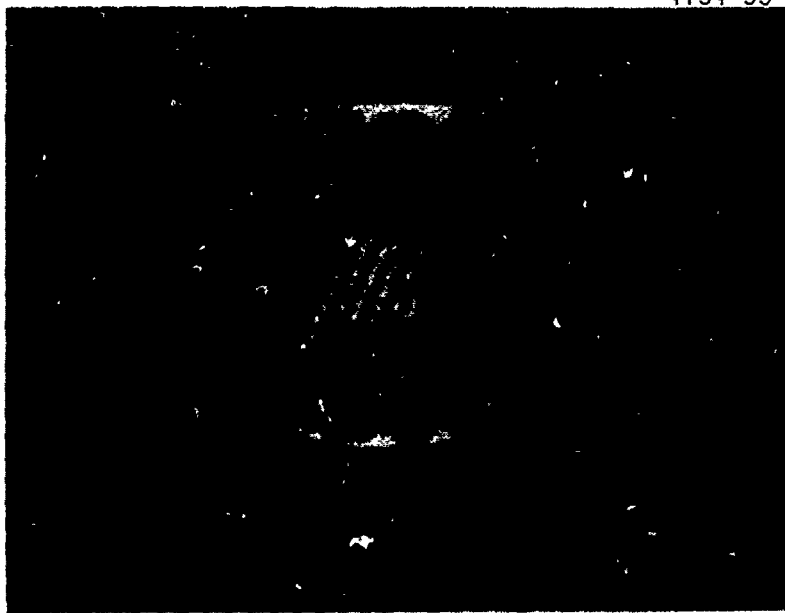
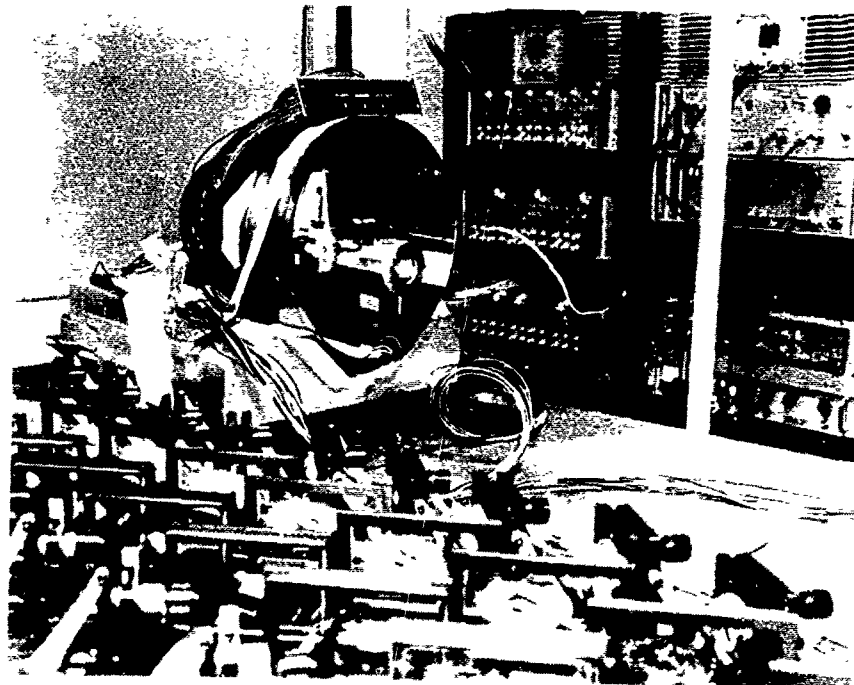


Fig. III-1(b). Interferogram of surface showing one actuator energized.



4845-35

Fig. III-2. Hughes high power phase compensating deformable mirror.

Figure III-3 is a high power dither mirror developed on a parallel IR&D program. In this, nine actuator stations are included, with the center driven. The faceplate is grooved to relax faceplate stiffness. An interesting feature of this design is its extremely high operating frequency (over 40 kHz), made possible by a cylinder spring surrounding the PZT cylinder to raise its resonant frequency, and the symmetrical model attachment, which decouples the dither drive oscillations from the backplate, giving better isolation between actuators.

The three basic types of phase correctors considered for compensated imaging applications are schematically illustrated in Fig. III-4. The segmented array of Fig. III-4(b) features certain simplicities of analysis, and its performance readily lends itself to an optimized dither mirror, as will be discussed. The monolithic array (Fig. III-4(c)) has strong advantages in economy of manufacture and maximum array density. Balanced against this is a relatively undeveloped technology and distinct disadvantages in high voltage drive requirements and the lack of cooling provisions. The third type of phase corrector (Fig. III-4(a)) is the deformable mirror, discrete actuator corrector. We discuss the design considerations for the deformable mirror below.

A. Surface Figure

The manner in which a surface approximates the desired figure by a finite number of actuators significantly influences the system performance. It appears that some considerable advantage can be gained by using a surface which can optimally tilt as well as displace.

The deformable faceplate configuration might be expected to provide an inherent tilt correction. However, to achieve the optimum correction, the actuator faceplate interface must be carefully configured to optimize the mirror's ability to fit a typical atmospheric dislocation function, while maintaining faceplate stress within acceptable bounds. A few sample configurations are shown in Fig. III-5. Figure III-5(a) shows the nearly

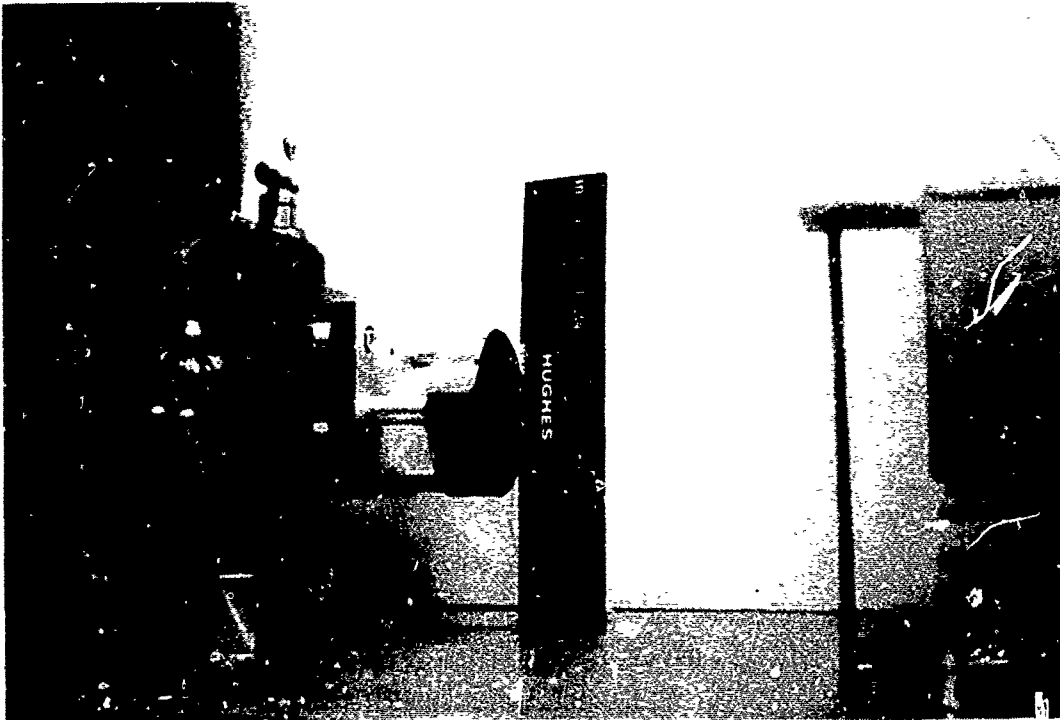
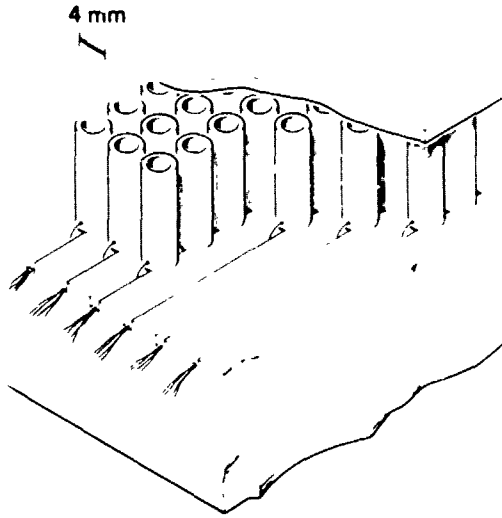
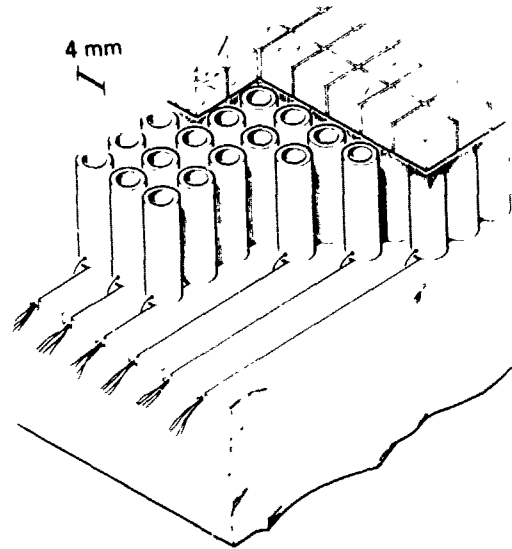


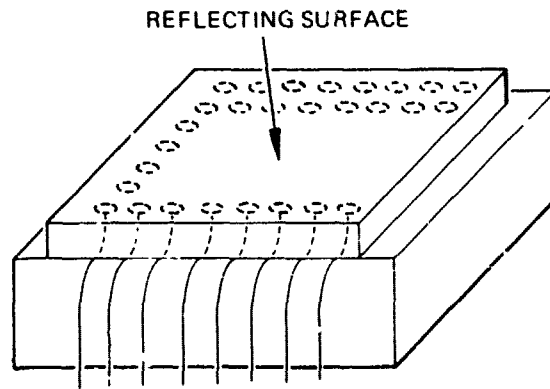
Fig. III-3. High power 28 kHz deformable dither mirror prototype.



a Deformable membrane mirror



b Segmented mirror



RIBBON CABLE TO AMPLIFIERS

c Monolithic mirror

Fig. III-4. Conceptual phase corrector/dither mirror configurations.

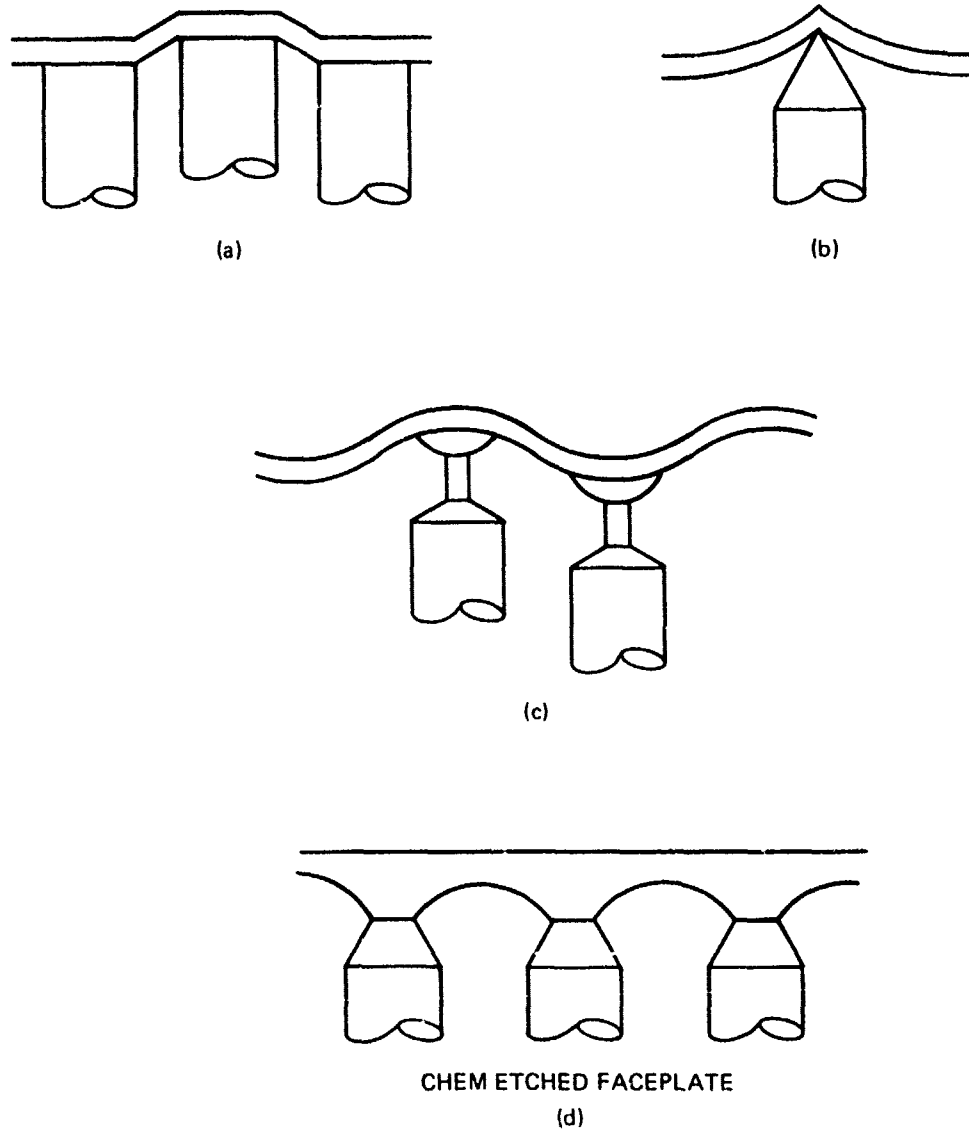


Fig. III-5. Faceplate-actuator design considerations.

segmented behavior of a deformable mirror when actuator head diameters (large compared to the spacing) are used. The opposite extreme (Fig. III-5(b)) can result in high localized stress and distortion over the head. Figure III-5(c) proposes a conceptual actuator head which provides flexure to accommodate tilt, with minimum compromise in inter-actuator coupling. Figure III-5(d) illustrates a simpler approach where a relatively thick faceplate is first fabricated, and then portions are etched away to increase faceplate compliance. This approach is promising because it allows careful shaping of the faceplate cross section to achieve the desired optimum mirror figure.

In our work to date we have investigated deformable mirrors both analytically and experimentally. The effect of deformable mirror figure upon COAT performance has been modeled in computer simulations where the faceplate deflection has been approximated as the deflection of a circular disk, clamped at the edges, and deflected at a central point. An analytic solution to this model is expressed as a table of deflections which is then incorporated into a COAT simulation algorithm.

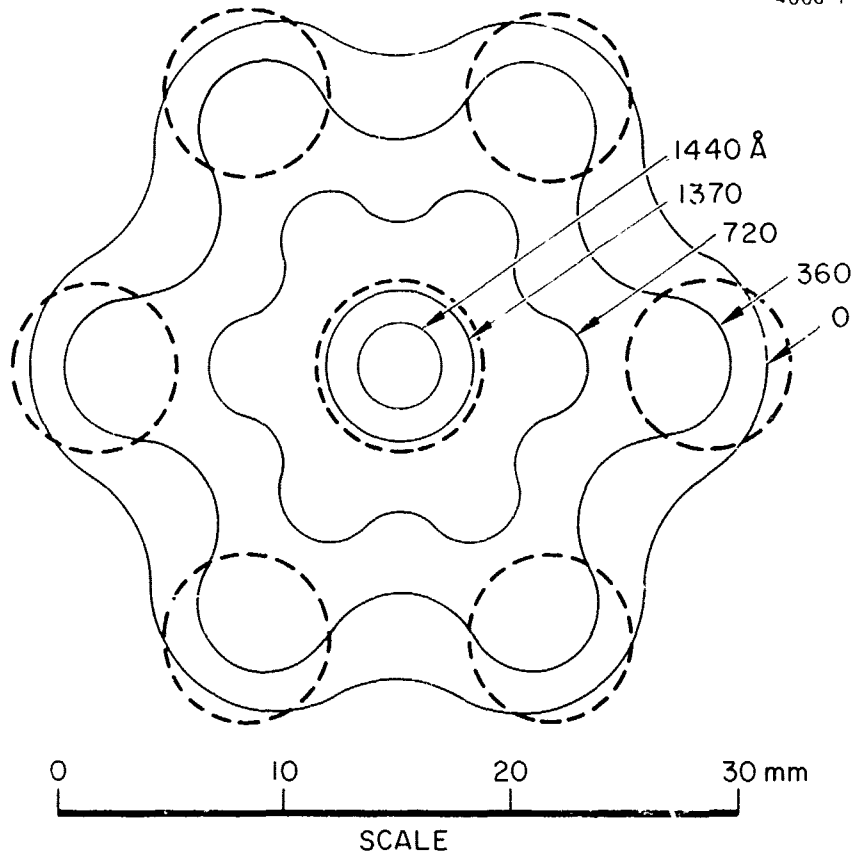
The central analytical approximations to the surface figure assumed a circularly symmetric smooth displacement from an actuator. Experimental observation, however, revealed a more complex pattern. Figure III-6 shows a static interferometric measurement of faceplate displacement for a hexagonal array of actuators on a deformable mirror. A double-pulse holographic exposure of the same mirror being driven at 13 kHz is shown in Fig. III-7, giving the identical pattern as for the static excitation.

We have shown that the actual surface, with finite head diameter and fixity at six points around the actuators, as described in Fig. III-6, can also be modeled with our computer techniques. This requires a simple change of the table used in our computer algorithm. As a result, a more accurate measure of deformable mirror COAT performance is obtained.

B. Structural Resonances

The key structural resonances in our deformable mirror system are the actuator/faceplate piston mode and the backplate mode (Figs. III-8(a) and III-8(b)). The frequency of the actuator/faceplate mode is determined by the mass of the faceplate, the mass of the actuator, and the spring constant

4006-1



MEASURED INTERFEROMETRICALLY AT 5461 Å GREEN
Hg LINE OVER RANGE OF -185 TO +185 V

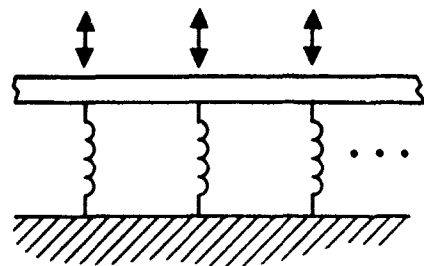
Fig. III-6. Isocontours of a portion of the 64-element I-COAT mirror with the central element deflected 1440 Å.

4075-68



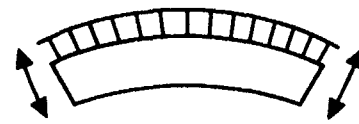
Fig. III-7. Double-pulse holographic interferogram of the 64-element I-COAT mirror with one actuator driven at 13 kHz, ± 250 V.

RESONANT MODES



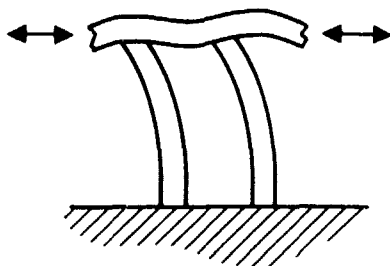
(a)

ACTUATOR/FACEPLATE

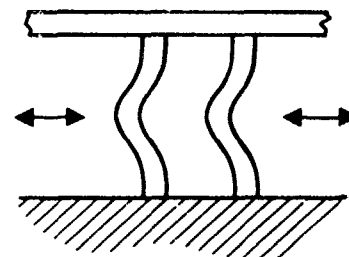


(b)

BACKPLATE MODES



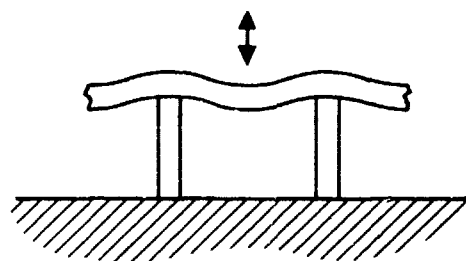
I



II

(c)

ACTUATOR LATERAL COLUMN RESONANCES



(d)

FACEPLATE DRUMHEAD MODES

Fig. III-8. Actuator, face plate, and backplate resonant modes.

of the actuator. In this system, the coupling to adjacent actuators, via the faceplate, contributes a small amount to the overall stiffness. The effect of the coupling is to simply broaden the actuator resonance into a band of resonances.

Additional resonant modes that must be considered are lateral column resonances (Fig. III-8(c)) and faceplate interactor drumhead modes.

1. Actuator/Faceplate Resonance

The lowest resonant frequency occurs when all the actuators vibrate in unison, so that the faceplate moves as a large piston. This resonant frequency can be obtained from the following expression:

$$f_o = \frac{1}{2\pi} \sqrt{\frac{k}{M + m/3}} \quad (3.1)$$

where

k = spring constant of actuator

m = mass of actuator

M = effective mass of faceplate defined as the mass of a disc whose radius is two thirds of the actuator spacing

For an actuator 1 cm long, 0.317 cm diameter, and 0.76 mm wall thickness, we obtain

$$f_o = 40 \text{ kHz} \quad (3.2)$$

Figure III-9 shows the effect of the actuator length on the resonant frequency. The resonant frequency given by this curve will not be affected appreciably by changes in actuator wall thickness or diameter since changes in these quantities leave the ratio of k/m constant. In addition, changes in the faceplate mass will have a nearly negligible effect on the resonant frequency since the faceplate mass is small compared to the actuator mass.

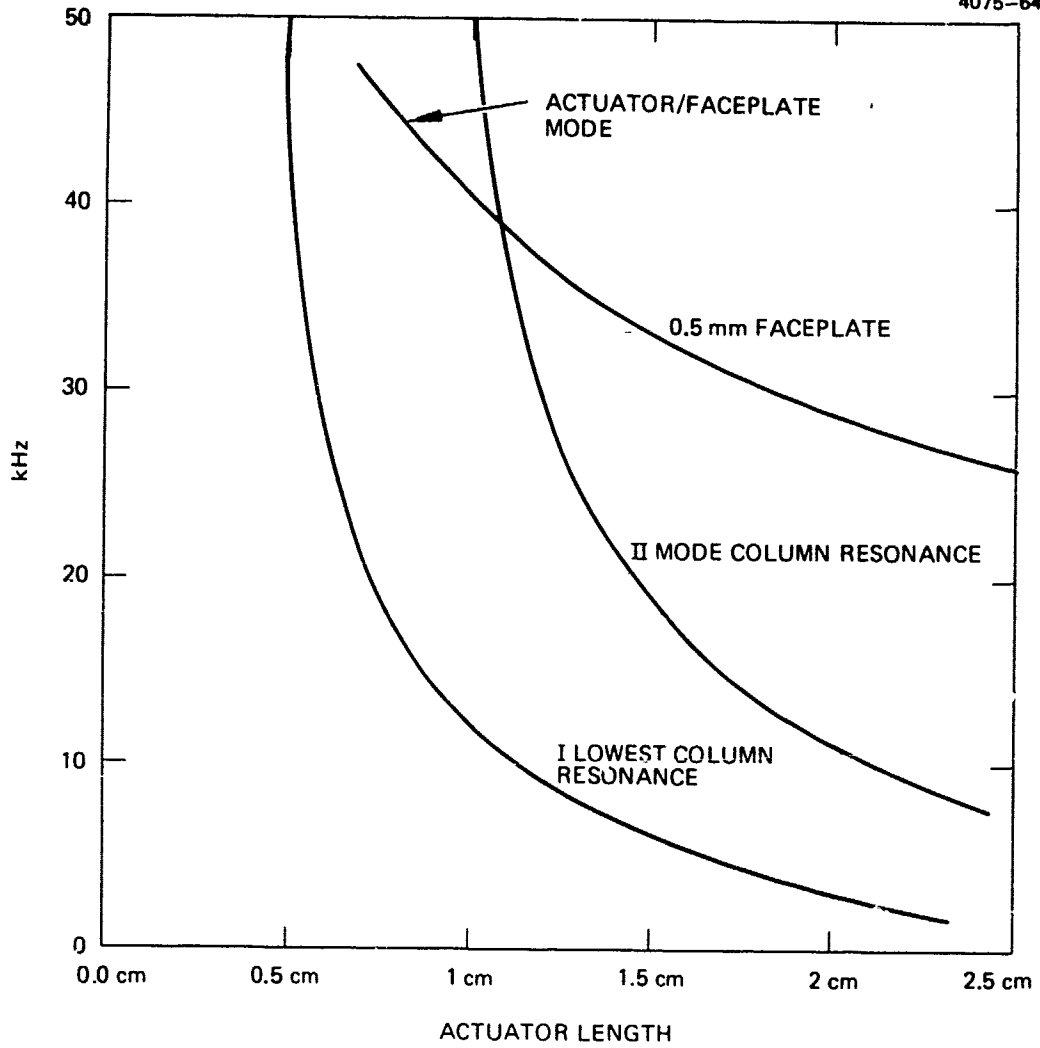


Fig. III-9. Resonant frequencies of the faceplate/actuator mode, and actuator column modes.

2. Interactuator Faceplate Resonant Modes

A stiff faceplate will raise the resonant frequency of the unsupported faceplate region between actuators but a flexible faceplate will minimize the necessary actuator forces and interactuator coupling. The resonant frequency of this region is given by solutions of the form

$$f_n = \beta_{ij} \left(\frac{t}{r^2} \right) \sqrt{\frac{E}{\rho(1-\nu^2)}} \quad (3.3)$$

where

E = Young's modulus of elasticity

ρ = density

ν = Poisson's ratio

r = radius of disk

t = thickness

For a rectangular array on 0.4 cm centers, the lowest resonance can be approximated by

$$f_n = \frac{\pi}{2} \left(\frac{t}{(0.4)^2} \right) \sqrt{\frac{E}{3\rho(1-\nu^2)}} \quad (3.4)$$

For a 0.4 mm thick glass faceplate we get a resonant frequency of about 125 kHz. In other words, it appears the faceplate can be made as thin as optical techniques permit.

3. Lateral Column Resonances

These modes are orthogonal to the driving forces as well as to the direction of phase shift. Thus their effect upon corrector mirror performance is certainly smaller than the previous cases, and perhaps neglectable. Nevertheless, an estimate of these frequencies can be easily made, where

$$f_c = \frac{3.52}{2\pi} \sqrt{\frac{EI}{\mu l^4}} \quad (3.5)$$

for the lowest mode, I, shown in Fig. III-8(c).

where

I = moment of inertia of cylinder cross section

μ = W/gl , mass/unit length

l = length

f_0 = 12 kHz for a 1 cm actuator, 0.317 cm diameter.

Figure III-9 illustrates the strong inverse square length dependence. However, since the faceplate can be strongly constrained at the edges against lateral movement (in a deformable but not a segmented mirror), the mode pictured in Fig. III-8(c), II, may be more appropriate. For this mode, the resonant frequency for our typical actuator is then

$$f_n \cong 50 \text{ kHz} \quad (3.6)$$

This type II mode is above the passband for actuators up to 2 cm. In addition, use of a 0.5-cm diameter actuator will raise the frequency by a factor of 2.5, placing the lowest mode above the passband for 2 cm actuator lengths.

4. Backplate Resonances

When the actuator array size becomes large, structural resonant modes of the backplate can occur at low frequencies and can dominate faceplate and actuator modes. The wave equation for simple thin plates

$$\nabla^4 \eta + \frac{12\rho(1-\nu^2)}{Et^2} \frac{d^2 \eta}{dt^2} = 0 \quad (3.7)$$

where

η = displacement

ρ = density

ν = Poisson's ratio

t = thickness of plate

E = Young's Modulus

can be solved for circular plates clamped at the edge.

$$f_n = 0.467 \left(\frac{t}{r^2} \right) \sqrt{\frac{E}{\rho(1-\nu^2)}} \quad (3.8)$$

for the lowest mode and for the edges free, clamped in the center (umbrella mode)

$$f_n = 0.17 \left(\frac{t}{r^2} \right) \sqrt{\frac{E}{\rho(1-\nu^2)}} \quad (3.9)$$

(The overtones in this system are not harmonic.)

For a 15 cm diameter glass substrate, 4 cm thick, the lowest frequency obtainable (in the umbrella mode) is

$$f_n = 6700 \text{ Hz} \quad (3.10)$$

Thus, one should employ a mirror-mounting system which will constrain the mirror to a higher normal mode, or use a structure of higher specific stiffness. For instance, by appropriate choice of mounting points, it should be fairly simple to constrain the mirror motion to a mode which is at least as high as the clamped mode ($f_n = 18 \text{ kHz}$).

Alternately, since f_n improves only by $\sqrt{E/\rho}$, materials choice offers limited advantage; experience in optical table design has shown that far greater results can be achieved without compromise of other properties

(such as coefficient of thermal expansion) by the use of high stiffness honeycomb construction. For glass, this has been sometimes implemented by fusing an array of tubes to two faceplates. Corresponding resonant frequencies can easily be tripled by this technique.

C. Interactuator Coupling

A property of deformable mirrors that has been a cause for concern is the extent to which the motion of one actuator affects the mirror figure at neighboring stations. It is shown below that even for an actuator of 4 cm in length and 0.317 cm in diameter the coupling coefficient is $\leq 1\%$ for a 0.4 mm faceplate. The effect of faceplate thickness is summarized in Fig. III-10. This chart plots interactuator coupling and stress as a function of actuator head diameter and faceplate thickness. The conclusions to be reached here are that faceplate thickness in the thinned etched regions (Fig. III-5(d)) are to be limited to about 0.5 mm by considerations of stress. If a material other than glass (or quartz or Cer-Vit) is to be used, one with a lower modulus of elasticity and/or higher stress limit, thicker faceplates can be used. For actuators which are shorter than the baseline 1 cm length, and therefore stiffer, the interactuator coupling is proportionately reduced.

The interactuator coupling is assumed to occur only through the faceplate. The coupling is expressed as a percentage of the initial motion, and by linear superposition; the general case of arbitrary displacement of all actuators can be modeled. Frequencies are assumed to be sufficiently below the lowest faceplate resonance, that static analysis is valid.

Figure III-11 shows seven actuators of a hexagonal array. The spring forces on the central actuator arise from the faceplate and can be approximated by considering the faceplate to be terminated at the first ring of surrounding actuators. This section of faceplate can be further approximated as a circular disc, with a hard peripheral support and a center load via the driving actuator (in Fig. III-12). The displacement at the center of this model is

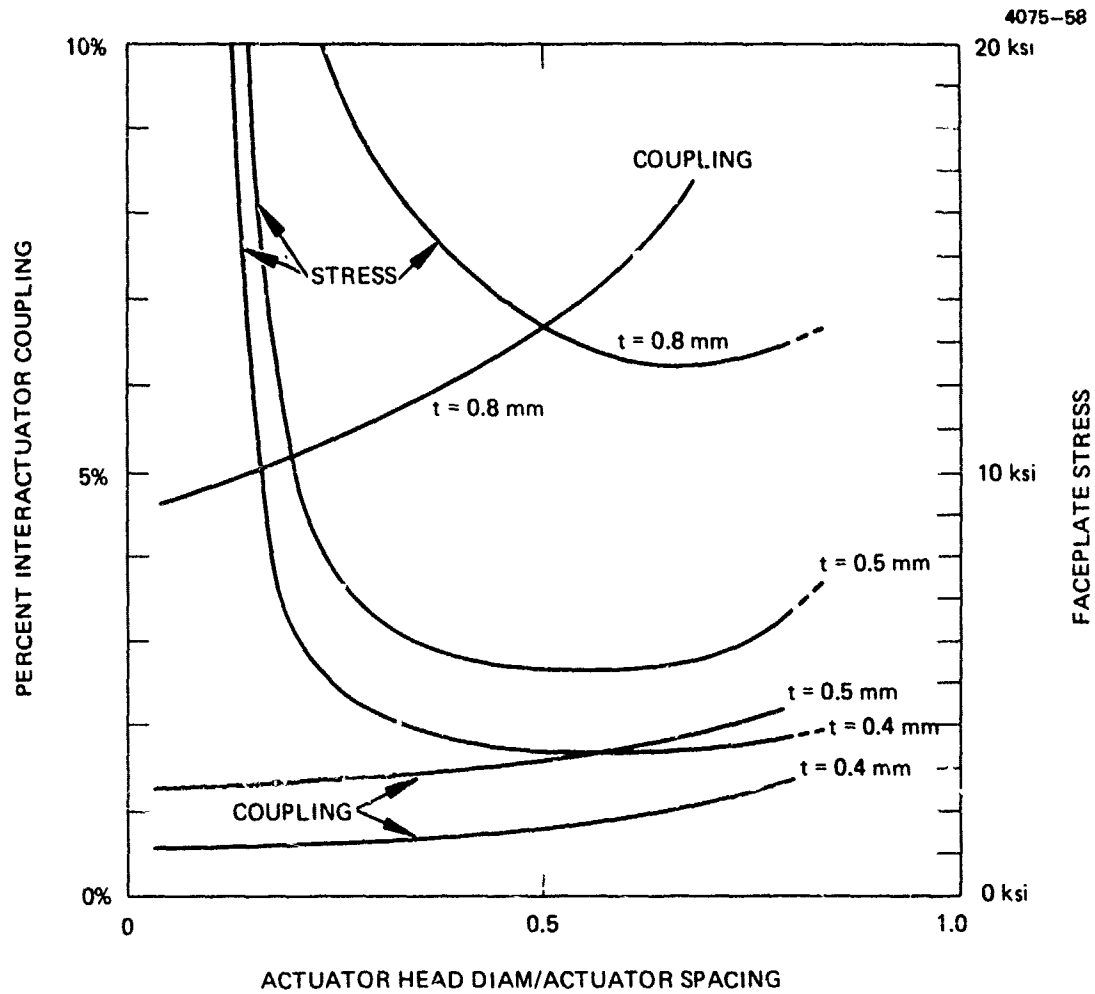


Fig. III-10. Interactuator coupling as a function of ratio of actuator head diameter to actuator spacing.

$$y = \frac{3W(m^2-1)}{4m^2\pi Et^3} [K_1] \quad (3.1)$$

$$\text{WHERE } K_1 = \frac{a^4(3m+1) - b^4(m-1) - 2a^2b^2(m+1) - 8ma^2b^2 \log\left(\frac{a}{b}\right) - 4a^2b^2(m+1)\left(\log\frac{a}{b}\right)^2}{a^2(m+1) + b^2(m-1)}$$

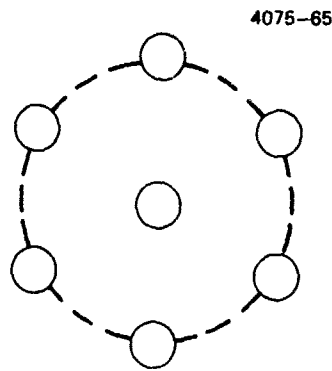
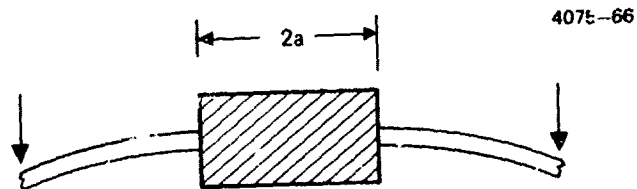


Fig. III-11.
Seven actuators.



- W = TOTAL APPLIED LOAD
- E = YOUNG'S MODULUS = 10^7 psi FOR GLASS
- t = THICKNESS OF PLATE
- m = $(\nu)^{-1} = (\text{POISSON'S RATIO})^{-1} = 4$ FOR GLASS
- a = RADIUS OF DISC = INTERACTUATOR SPACING = 0.4 cm
- b = RADIUS OF ACTUATOR HEAD DISC

REF ROARK, RELN NO. 22 P 223

Fig. III-12. Faceplate section.

Membrane or diaphragm stresses can be ignored, since the deflections are much smaller than the thickness. Thus the load deflection and load-stress relations are linear.

As a sample case, let us evaluate

$$t = 0.4 \text{ mm (faceplate thickness)}$$

$$a = 0.4 \text{ cm (actuator spacing)}$$

$$b = 0.1 \text{ cm (head diameter = 2 mm)}$$

then

$$y = 2.12 \times 10^{-4} W \text{ in English units}$$

$$\text{or, for } y = 1150 \text{ nm} = 4.53 \times 10^{-5} \text{ in.}$$

$$W = 0.21 \text{ lb}$$

The maximum faceplate stress is given approximately by

$$\sigma_r = \frac{3W}{2\pi t^2} [K_2]$$

where

$$K_2 = \frac{2a^2(m+1) \log \frac{a}{b} + a^2(m-1) = b^2(m-1)}{a^2(m+1) + b^2(m-1)} \quad (3.12)$$

or

$$K_2 = \frac{1}{2}(m-1) + (m+1) \log \frac{a}{b} - (m-1) \frac{b^2}{2a^2}, \quad (3.13)$$

whichever is larger.

Since the second expression is larger, the maximum stress occurs over the actuator head (Fig. III-13) and is equal to

$$\sigma_r = 3,400 \text{ psi}$$

4075-67

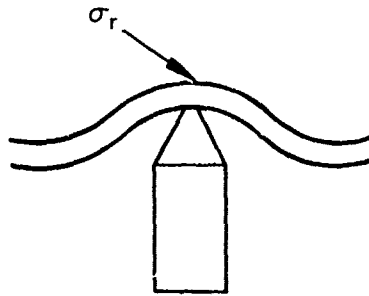


Fig. III-13. Actuator head.

This is a value which can be accommodated by conventional glasses. For a faceplate which is properly etched, the stresses can be expected to be lower due to the smooth fillets.

The faceplate spring constant is simply

$$k_f = \frac{W}{y} = 4.64 \times 10^3 \text{ lb/in.} \quad (3.14)$$

By comparison, the actuator spring constant can be calculated using the expression

$$y = \left[\frac{\ell}{A_1 E_1} \right] + \frac{h}{A_2 E_2} \quad (3.15)$$

where

ℓ = actuator length

A_1 = cross-sectional area of actuator tube

E_1 = modulus of elasticity of PZT in Y_{31} direction
when short circuited

h = height of actuator head

A_2 = average cross sectional area of actuator head

E_2 = Young's modulus of elasticity of actuator head

For our sample case, let us take the more challenging case of a long actuator configured for low voltage (since this aids in driver design), where

actuator length = 4 cm = 1.57 in.

actuator tube wall thickness = 0.020 in.

actuator diameter = 0.125 in.

$E_1 = (12.3 \times 10^{-12} \text{ m}^2/\text{nt})^{-1}$ for PZT-4, short circuited
 $= 8.1 \times 10^{10} \text{ nt/m}^2 = 11.8 \times 10^6 \text{ psi}$

$h = 0.4 \text{ cm} = 0.157 \text{ in}$

$A_1 = 1.5 \times 10^{-2} \text{ in.}^2$

$A_2 = 1.068 \times 10^{-2} \text{ in.}^2$, assuming hollow heads of
0.040 in. wall thickness

$E_2 = 10 \times 10^6 \text{ psi}$ for glass

then

$$y = 1.07 \times 10^{-5} W$$

or

$$k_a = 9.34 \times 10^4 \text{ lb/in.}$$

This should represent very nearly a worst (lowest stiffness) case analysis for the actuator.

The stress in the actuator due to the faceplate constraint is

$$\sigma = \frac{W}{A} = 14.5 \text{ psi}$$

which is well below the 8000 psi limit set by the manufacturer to hold stress induced depoling to 10%. Dynamic stresses may however be higher.

The buckling limit for this actuator, incidentally, is

$$W = \frac{\pi^2 EI}{l^2}$$

where

$$I = \frac{1}{4} \pi (R^4 - R_o^4) \text{ the moment of inertia}$$

$$R = \text{O.D.} \div 2$$

$$R_o = \text{I.D.} \div 2$$

$$I = 9.42 \times 10^{-6} \text{ in.}^4$$

When

$$W = 442 \text{ lb, or at stress of 30 ksi, in the actuator} \\ \text{(failure is at 75 ksi)}$$

The interactor coupling can be deduced from the following considerations.

1. The force on the actuator head is equal and opposite to the force of constraint of the faceplate.
2. The force of a central actuator is exactly encountered by an opposite force on the six surrounding actuators. Thus, the force on one adjacent actuator is 1/6 the force on the deployed actuator (see Fig. III-11).
3. In Fig. III-14, a spring model for Fig. III-11 is constructed. $k_f(\Delta x_1) = 6k_a(\Delta x_2)$, by statement (1) and (2), where Δx_1 is the displacement of the

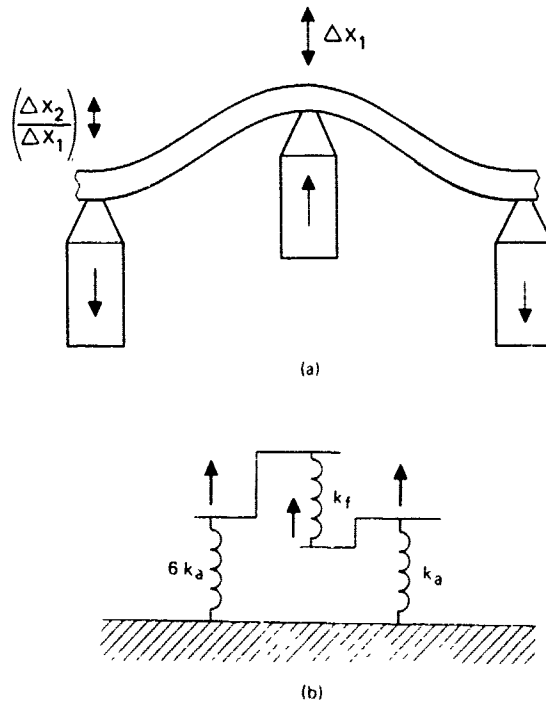


Fig. III-14. Spring model.

faceplate and activated actuator, and Δx_2 is the displacement of the adjacent actuator. It follows that the coupling between two actuators, expressed as a fraction is then

$$\frac{\Delta x_2}{\Delta x_1} = \frac{k_f}{6k_a} = 8.4 \times 10^{-3}$$

or .1%.

Since computer simulations have shown that considerable interaction coupling can be tolerated, the faceplate can be made up to twice the thickness used here. Even with this increase in thickness the inter-actuator coupling is less than 7%. However, faceplate stresses will have to be carefully calculated and controlled by actuator head diameter choice and the geometrical shaping of the juncture. Whereas, in this example, there is only a 5% shortening of the actuator by the faceplate constraint, a stiffer faceplate will require an actuator with an appreciably greater free extension.

Computer simulations for multidither COAT systems have shown that interactor coupling of up to 30% results only in a small loss of convergence time. Thus, with coupling typically under 1%, interactor coupling alone does not significantly impact our baseline design.

1. Assembly Techniques for Deformable Reflectors

During the past seven years Hughes Aircraft Company has gained considerable experience in joining complex mirror structures. Our molybdenum cooled mirrors for high power applications are now joined by a high temperature brazing process, followed by cold cycling down to 80°K, to relieve braze stresses and stabilize the mirror figure. The deformable reflector shown in Fig. III-2 employs threaded preloading rods which act to join faceplates to PZT actuator, preload the PZT-5H stacks, and also to supply a portion of the actuator spring construction. This design has also proved to be stable with time.

One prototype for imaging applications (Fig. III-1) uses epoxy (Armstrong A-12) bonding between the faceplate and actuator heads, as well as for the rest of the structure. The stability of such organic bonds is presently under investigation. Other adhesives presently under investigation are Eastman type 910 adhesive, a UV curing PMM Loctite glass adhesive, and various Owens-Illinois silicon glass adhesives. Other techniques that might merit consideration include optical contacting, metal diffusion bonding, and soldering.

One Hughes preliminary design is illustrated in Fig. III-15. A 15 cm backplate around 4 cm thick of Pyrex or Cer-Vit honeycomb construction is mounted to a blocklike mirror mount in a manner which minimizes resonances. A discrete actuator array of 500 PZT-4 or PZT-8 cylinders between 0.5 cm and 2 cm in length is ground and lapped to equal length in one batch. These are bonded to the optically flat backplate, with the aid of a locating fixture plate. Actuator heads of a material with identical expansion coefficient to the faceplate, with a head diameter of about half the actuator spacing are fabricated as shown, bonded to the PZT tubes, and ground and lapped to create a flat surface. A faceplate of roughly 1 mm thickness is made optically parallel using a technique which has been

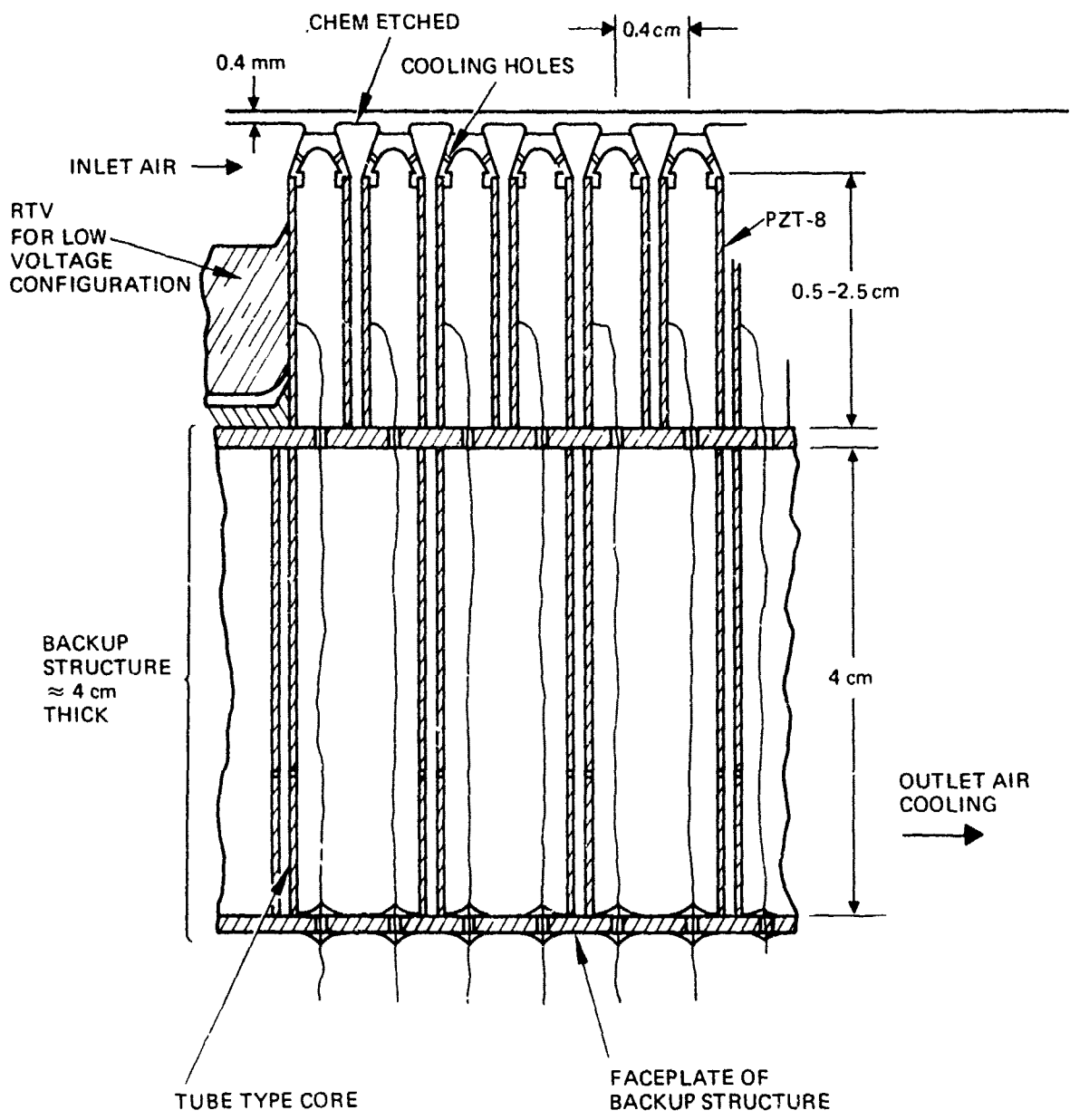


Fig. III-15. Conceptual deformable mirror cross-section using a honeycomb backplate structure.

employed by our optical fabrication shop in which the faceplate is bonded to a flat during polishing. The back surface is then photomasked and etched to thin the interactor regions to 0.4 to 0.5 mm. This plate is then bonded to the actuator heads and the final structure is thermally cycled, stabilized, "aged" by driving the PZT actuators, and given a final polish to the best possible flatness if necessary. Possible added features are cooling passages, and an RTV low modulus damping material. One thousand addressable leads are required in the baseline design, and 2500 in the digital design. These are appropriately routed through connectors on the back of the mirror mount, and through ribbon cables to the electronic driver rack.

IV. THE MULTIPLE APERTURE INTERLINKED BLOCK CODED SYSTEM

A. Introduction

This section presents the description of the block coded, multiple aperture, interlinked (MAIL), deferred-correction, polystep-dither imaging system proposed for predetection compensated imaging of objects viewed through turbulent atmosphere. The linked, block-coded system dithers a mirror surface sequentially in a code organized by blocks of the mirror surface. The linked, block-coded system uses the polystep dither sequence to measure the atmospheric phase distortions introduced in the incident wavefront from the target.

The procedure to estimate these phase distortions is as follows. The light that is reflected from each of the "elements" (mirror regions) within a block is focused to an image plane. Each block has an associated pinhole in the image plane that transmits a portion of the incident light to an optical detector behind the pinhole (see Fig. IV-1). The elements of the mirror surface may be either piston mirrors or portions of a deformable mirror. The blocks, lenses, pinholes, and detectors are replicated many times, such that the entire aperture (or its image) is completely covered. Each actuator basically perturbs the illumination fields falling on two adjacent lenses so that displacements in any one elemental area of the mirror displace (or shape) the images in two adjacent block image planes. (With deformable mirrors the perturbation effects may extend over more than two lenses, but these are basically second order effects. As the dither process is sequenced through a series of discrete steps (typically, four or six), the associated intensities, as transmitted through the pinhole, are detected, integrated and stored in a computer memory. Conceptually, at least, the associated integrated intensities or photoelectron counts are first employed to correct the intrablock errors for every block. Since dual, generally conflicting estimates of the corrections are obtained for the full array of actuators, a rectification routine is required to remove or at least minimize the discrepancies.

Many different dither sequences, block organizations, and rectification routines are possible. One of the most promising block organizations is with four-element blocks employing a six-step, double-element dither sequence, as illustrated in Fig. IV-2 and described in Table IV-1. Each of these dither sets perturbs the "block" image which is formed by a particular block lens upon a pinhole located in its focal plane, as illustrated (by typical perturbation sets) in Fig. IV-3. In general, the perturbations either displace the image or distort it, such that an increased or reduced number of photons impinges on the underlying detector, Fig. IV-4. This increased or decreased photon count is caused by the mirror displacement being an improvement or degradation of the image. The atmospheric phase distortions measured by the variation in dithered image intensity is then compensated by mirror correction.

A second, promising block organization employs two element blocks using a single two step dither sequence as illustrated in Fig. IV-5 and described in Table IV-2. This block organization offers an improved signal-to-noise ratio for viewing dim targets but requires many more detectors, assuming the spacing between actuators is constant.

Table IV-1. Six-Step (Arc-Sine) Block Dither Sequence for a Four-Element Block-Coded Linked I-COAT System

n	ψ_0	ψ_1	ψ_2	ψ_3
1	0	0	$\pi/2$	$\pi/2$
2	0	0	$-\pi/2$	$-\pi/2$
3	0	$\pi/2$	$\pi/2$	0
4	0	$-\pi/2$	$-\pi/2$	0
5	0	$\pi/2$	0	$\pi/2$
6	0	$-\pi/2$	0	$-\pi/2$

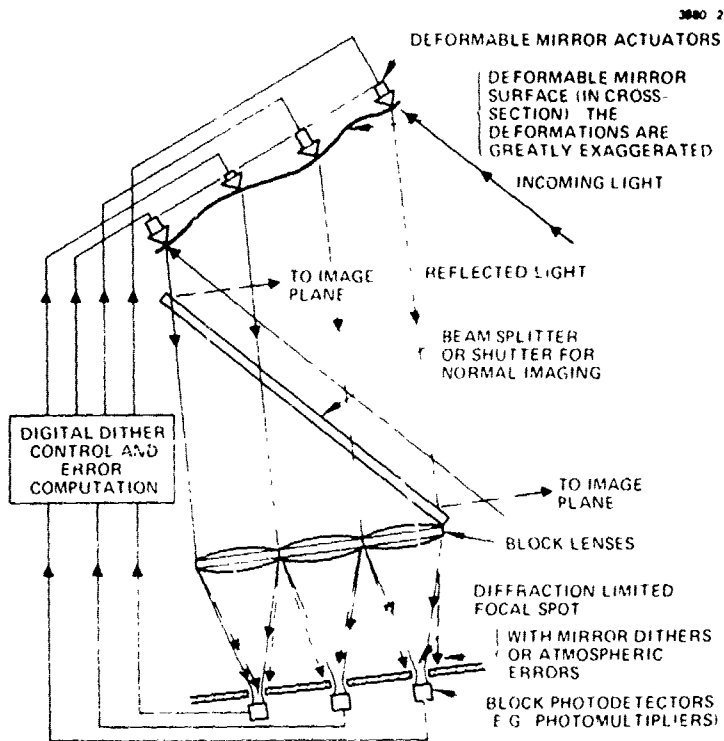


Fig. IV-1. Block-coded, multiple-apertured, inter-linked, imaging COAT system.

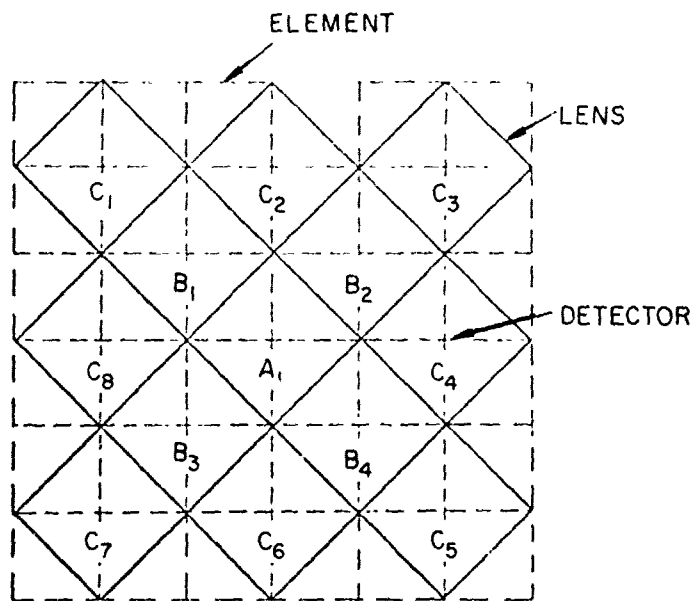


Fig. IV-2. Linked, block-coded I-COAT system. Two elements are simultaneously dithered in every block.

DITHER SEQUENCE NO.

3880-1R1

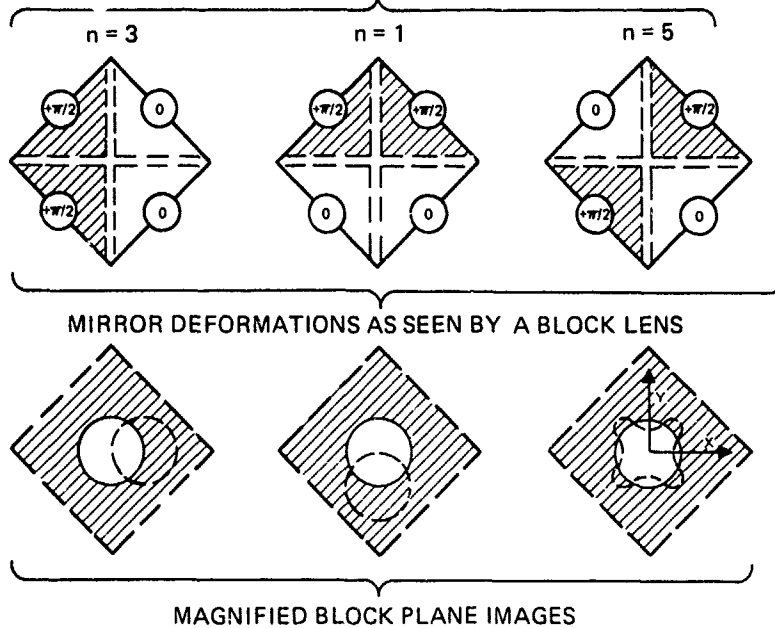
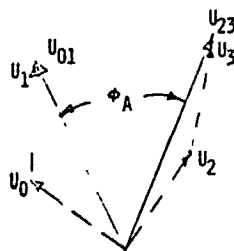


Fig. IV-3. Typical mirror deformations and block-plane images with piston mirrors.



$$I_1 = \kappa(|u_{01}|^2 + 2|u_{01} u_{23}| \cos(\phi_A + \pi/2) + |u_{23}|^2)$$

$$I_2 = \kappa(|u_{01}|^2 + 2|u_{01} u_{23}| \cos(\phi_A - \pi/2) + |u_{23}|^2)$$

FOR THE NEARBY CONVERGED CASE, THE ASSOCIATED PHOTOELECTRON COUNTS ARE

$$(NPE)_1 = (NPE)_0 (1 - \sin\phi_A)$$

$$(NPE)_2 = (NPE)_0 (1 + \sin\phi_A)$$

FROM WHICH

$$\phi_A = \sin^{-1} \left\{ \frac{(NPE)_2 - (NPE)_1}{(NPE)_2 + (NPE)_1} \right\}$$

Fig. IV-4. Phasor diagram which defines ϕ_A .

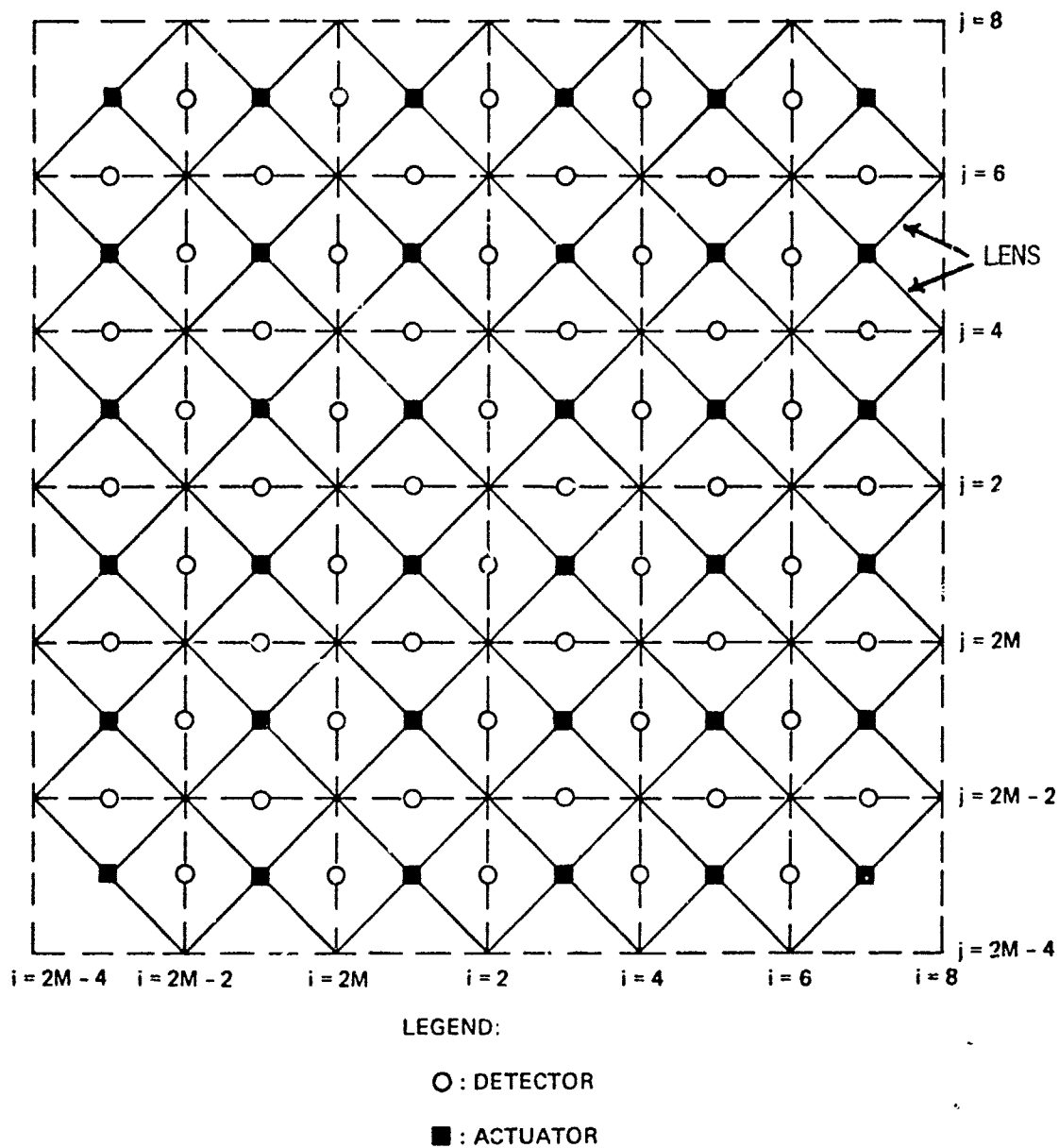


Fig. IV-5. Linked, block coded, I-COAT system. Adjacent actuators dither in alternate sequence.

Table IV-2. Two-Step (Arc-Sine) Block Dither Sequence for a Two-Element Block-Coded Linked I-COAT System

n	ψ_0	ψ_1
1	$-\pi/4$	$+\pi/4$
2	$+\pi/4$	$-\pi/4$

B. Pairwise Element Angle Calculation for Four Elements per Block

Consider the piston-mirror dither policy of Table IV-1 and suppose that the transmitted optical intensities through the pinholes are proportional to the on-axis intensities (this is certainly true for small pinholes but can also be shown to hold for larger pinholes) within a scale factor. Let the fields of elements 0, 1, 2, and 3 be designated by the phasors U_0 , U_1 , U_2 , and U_3 . Let U_{nm} be the phasor sum of U_n and U_m . Next, consider the element pairings leading to U_{01} and U_{23} for example. In steps $N = 1$ and 2, the pair of elements "2" and "3" are perturbed as an entity in phase steps $+\pi/2$ and $-\pi/2$, giving on-axis intensities at the pinhole.

$$I_1 = K \left[|U_{01}|^2 + 2 |U_{01} U_{23}| \cos(\phi_A + \pi/2) + |U_{23}|^2 \right] \quad (4.1.a)$$

$$I_2 = K \left[|U_{01}|^2 + 2 |U_{01} U_{23}| \cos(\phi_A - \pi/2) + |U_{23}|^2 \right] \quad (4.1.b)$$

where K is an optical constant, relatable to the incident flux, and ϕ_A is the phasing error of the phasor pair U_{23} relative to U_{01} (see Fig. IV-4).

These field intensities are transmitted through a pinhole with transmission efficiency η_p and integrated on a photosurface generating a photocurrent with quantum efficiency η_q . These currents are then integrated for the time period T_m , producing a mean total number of photoelectrons NPE, where for the near convergence condition, each of the optical intensities of (4.1) gives

$$\overline{(NPE)}_1 = \overline{(NPE)}_e [1 - \sin \phi_A] \quad (4.2. a)$$

$$\overline{(NPE)}_2 = \overline{(NPE)}_e [1 + \sin \phi_A] \quad (4.2. b)$$

and $\overline{(NPE)}_e$ is the mean effective number of photoelectrons induced by the photons falling on one (square) element in one measurement integration time, T_m ; or

$$\overline{(NPE)}_e = 2KU_{01}^2 T_m = \eta_p \eta_q P_e = N_0 \quad (4.2. c)$$

where N_0 is the number of photoelectrons per actuator element in one measurement integration time and P_e is the total number of photons falling on an element during an integration time. Equation (2.2c) is essentially a statement of the conservation of photons (or energy) in the imaging process. Based on these photoelectron counts, one forms an estimator on ϕ_A called $\hat{\phi}_A$

$$\begin{aligned} \phi_A &= \sin^{-1} \left[\frac{\overline{(NPE)}_2 - \overline{(NPE)}_1}{\overline{(NPE)}_2 + \overline{(NPE)}_1} \right] \\ &= \sin^{-1} \left[\frac{2\overline{(NPE)}_e \sin \phi_A + N_2 - N_1}{2\overline{(NPE)}_e + N_2 + N_1} \right] \end{aligned} \quad (4.3)$$

where N_2 and N_1 are zero-mean noise disturbances with variances associated with the integrated photoelectron measurements of (4.2). For the high S/N case where N_2 and N_1 are very small, (4.3) becomes, to a reasonable approximation,

$$\phi_A = \hat{\phi}_A \quad (4.4)$$

Similarly, we estimate two other "pairwise" phase errors $\hat{\phi}_B$ and $\hat{\phi}_C$ based on photoelectron counts from dither sequences $N = 3, 4, 5,$ and 6

$$\phi_B = \sin^{-1} \left[\frac{(\overline{\text{NPE}})_4 - (\overline{\text{NPE}})_3}{(\overline{\text{NPE}})_4 + (\overline{\text{NPE}})_3} \right] \quad (4.5)$$

$$\phi_C = \sin^{-1} \left[\frac{(\overline{\text{NPE}})_6 - (\overline{\text{NPE}})_5}{(\overline{\text{NPE}})_6 + (\overline{\text{NPE}})_5} \right] \quad (4.6)$$

The true pairwise phasing errors are

$$\phi_A = \phi_{23} - \phi_{01} = \frac{1}{2} (\phi_3 + \phi_2 - \phi_1 - \phi_0) \quad (4.7.a)$$

$$\phi_B = \phi_{13} - \phi_{02} = \frac{1}{2} (\phi_3 + \phi_1 - \phi_2 - \phi_0) \quad (4.7.b)$$

$$\phi_C = \phi_{12} - \phi_{03} = \frac{1}{2} (\phi_2 + \phi_1 - \phi_3 - \phi_0) \quad (4.7.c)$$

where ϕ_{nm} is the phase associated with the field U_{nm} . The right-hand expansion of (4.7) employs the property (unique to two elements) that the composite phase (error) of a phasor pair is the average of the individual phases (errors). Equation (4.7) yields a set of estimation correction settings (within each block).

C. Block Rectification Procedure for Four Elements per Block

Using the results from the previous section, the phase variation between elements in a single block is obtained from (4.7) to be

$$\phi_1 - \phi_0 = \phi_B + \phi_C \quad (4.8.a)$$

$$\phi_2 - \phi_0 = \phi_A + \phi_C \quad (4.8.b)$$

$$\phi_3 - \phi_0 = \phi_A + \phi_B \quad (4.8. c)$$

If the telescope required only one block for wavefront correction, actuators 1, 2 and 3 could be displaced to drive $\phi_1 - \phi_0$, $\phi_2 - \phi_0$ to zero. However, the telescope requires many contiguous blocks with each actuator (mirror element) shared between two blocks. Wavefront correction for one block may conflict with the mirror element displacement requirement for the element's adjacent block. The method chosen to resolve these potential conflicts is to select a predetection compensation performance criterion to be optimized and then determine the actuator control law that will seek to optimize this performance criterion. We have chosen to minimize the sum over all the actuator locations of the squares of the optical path length errors. The specific description of this criterion and the optimum actuator control law is discussed in Section V-B. It is shown that the optimum block rectification procedure is of the form

$$\hat{\underline{X}} = B \underline{\phi} \quad (4.9)$$

where $\underline{\phi}$ are the measured phase variations $\{\phi_i\}$, B is a matrix obtained from the noise covariance matrix of the measurements and $\hat{\underline{X}}$ are the best estimate of the actuator positions $\{X_i\}$. The expression for B is described in Section V-B to obtain a minimum sum of the squares of the optical path length errors.

D Introduction to the Two Element per Block Organization

Another promising block organization uses two-element blocks in a two-step, two-element dither sequence, as illustrated in Fig. IV-2 and described in Table IV-2. Each of the dither steps perturbs the "block" image which is formed by a particular block lens upon a pinhole located in its focal plane. The perturbations displace the image such that an increased or reduced number of photons impinges on the underlying detector. This increased or decreased photon count is caused by the

mirror displacement being an improvement or degradation of the image. The atmospheric phase distortions measured by the variation in dithered image intensity is then compensated by mirror correction.

E. Element Angle Calculation for Two Elements per Block

Consider the piston-mirror dither policy of Table IV-1 and suppose that the transmitted optical intensities through the pinholes are proportional to the on-axis intensities (this is certainly true for small pinholes but can also be shown to hold for larger pinholes) within a scale factor. Let the fields of elements 0 and 1 be designated by the phasers U_0 and U_1 . In steps $N = 1$ and 2 , the elements "0" and "1" are perturbed in phase steps $+\pi/4$ and $-\pi/4$ alternately, for a net difference of $\pi/2$, giving on-axis intensities at the pinhole

$$I_1 = K \left[|U_0|^2 + 2 |U_0 U_1| \cos(\phi + \pi/2) + |U_1|^2 \right] \quad (4.10a)$$

$$I_2 = K \left[|U_0|^2 + 2 |U_0 U_1| \cos(\phi - \pi/2) + |U_1|^2 \right] \quad (4.10b)$$

where K is an optical constant, relatable to the incident flux, and ϕ is the phase error of the phaser U_1 relative to U_0 .

These field intensities are transmitted through a pinhole with transmission efficiency η_p and integrated on a photosurface generating a photocurrent with quantum efficiency η_q . These currents are then integrated for the time period T_m , producing a mean total number of photoelectrons NPE , where for the near convergence condition, each of the optical intensities of (4.10) gives

$$\overline{(NPE)}_1 = \overline{(NPE)}_e [1 - \sin \phi] \quad (4.11a)$$

$$\overline{(NPE)}_2 = \overline{(NPE)}_e [1 - \sin \phi] \quad (4.11b)$$

and $(\overline{NPE})_e$ is the mean effective number of photoelectrons induced by the photons falling on one quarter of an actuator (square) element in one measurement integration time, T_m ; or

$$(\overline{NPE})_e = 2KU_0^2 T_m = \eta_p \eta_q P_e = \frac{N_0}{4}, \quad (4.11c)$$

where N_0 is the number of photoelectrons per actuator element area per measurement integration time and P_e is the total number of photons falling on a quarter of an actuator element during an integration time. Equation (4.11c) is essentially a statement of the conservation of photons (or energy) in the imaging process. Based on these photo-electron counts, one can form an estimator on ϕ called $\hat{\phi}$

$$\begin{aligned} \hat{\phi} &= \sin^{-1} \left[\frac{(\overline{NPE})_2 - (\overline{NPE})_1}{(\overline{NPE})_2 + (\overline{NPE})_1} \right] \\ &= \sin^{-1} \left[\frac{2(\overline{NPE})_e \sin \phi_A + N_2 - N_1}{2(\overline{NPE})_e + N_2 + N_1} \right] \end{aligned} \quad (4.12)$$

where N_2 and N_1 are zero-mean noise disturbances with variances associated with the integrated photoelectron measurements of (4.11). For the high S/N case where N_2 and N_1 are very small, (2.3) becomes, to a reasonable approximation,

$$\hat{\phi} \doteq \phi \quad (4.13)$$

For the special case when the target is of uniform brightness and target scintillation is not present, then only one dither step is required to measure ϕ . For the targets being considered in this analysis, the mean effective number of photoelectrons $(\overline{NPE})_e$ is constant and can be estimated from prior data. Hence, the phase error ϕ can be estimated by

$$\begin{aligned}\hat{\phi} &= \sin^{-1} \left[\frac{(\overline{\text{NPE}})_2}{(\overline{\text{NPE}})_e} - 1 \right] \\ &= \sin^{-1} \left[\frac{(\overline{\text{NPE}})_e \sin + N_2}{(\overline{\text{NPE}})_e} \right].\end{aligned}\quad (4.14)$$

For the high S/N case where N_2 is very small, (4.14) becomes, to a very reasonable approximation,

$$\hat{\phi} = \phi \quad (4.15)$$

SECTIONS V and VI (pages 89 - 135) have been deleted from this document.

VII. IMPROVED PREDICTIVE TRACK PROCEDURES

A critical technology issue identified for the conditions specified in the Second Standard Noise Calculation for any predetection compensated imaging system is to compensate a fast-moving image viewed through strong plus distributed turbulence. The phase error measurement strategy for compensation is to use predictive track of multiple phase layers to obtain an extended integration time when it is advantageous; otherwise, rely on a one phase layer "quick look" of the phase error while viewing a bright target.

A. One Phase Layer "Quick Look" Technique

The residual phase error for our compensated imaging system comes from three sources: the error introduced by detector noise; the error introduced by an imperfect fit of the deformable mirror surface to the desired correction; and the error introduced by the fact that the required phase correction changes as a function of time, and hence a detector having a finite response time, tends to measure a time-averaged value of the required correction rather than the instantaneous value. Since these errors are statistically independent, the net mean square residual phase error is equal to the sum of the individual errors

$$\langle (\Delta\phi)^2 \rangle = \langle (\Delta\phi)^2 \rangle_D + \langle (\Delta\phi)^2 \rangle_M + \langle (\Delta\phi)^2 \rangle_{TA}, \quad (7.1)$$

where the subscripts D, M, and TA denote detector, mirror, and time average, respectively. Utilizing results described in reference A, we can express the terms in eq. (7.1) as follows

$$\langle (\Delta\phi)^2 \rangle_D = \frac{6}{P A_e \tau} \left[\frac{1}{4\pi} \ln \frac{17671}{A_e} + 0.12 \right], \quad (7.2)$$

$$\langle (\Delta\phi)^2 \rangle_M = 0.407 A_e^{5/6} r_o^{-5/3}, \quad (7.3)$$

$$\langle (\Delta\phi)^2 \rangle_{TA} = \frac{3}{11} \hat{c}(\omega) \tau^{5/3}, \quad (7.4)$$

where A_e is the mirror area per actuator, τ is the measurement time, P is the number of photoelectrons detected per unit area of the primary mirror per millisecond, r_o is the phase coherence length defined by Fried, and $\hat{c}(\omega)$ is given by the expression

$$\hat{c}(\omega) = 2.91 k^2 \int_0^\infty dh C_N^2(h) \left| \bar{w} + \frac{\tau}{\theta h} \right|^{5/3}. \quad (7.5)$$

As system designers, we wish to select the element area A_e and the system response time τ so as to minimize the net residual phase error. To determine the optimum values of these parameters, let us express eq. (7.1) in the form

$$\langle (\Delta\phi)^2 \rangle = \alpha \tau^{5/3} + \beta \tau^{-1} + \gamma, \quad (7.6)$$

with

$$\alpha = \frac{3}{11} \hat{c}(\omega) \quad (7.7)$$

$$\beta = \frac{6}{P A_e} \left[\frac{1}{4\pi} \cdot \frac{17671}{A_e} + 0.12 \right], \quad (7.8)$$

$$\gamma = 0.407 A_e^{5/6} r_o^{-5/3}. \quad (7.9)$$

The minimum of $\langle (\Delta\phi)^2 \rangle$ with respect to τ and A_e occurs when $\partial \langle (\Delta\phi)^2 \rangle / \partial \tau$ and $\partial \langle (\Delta\phi)^2 \rangle / \partial A_e$ are zero. This yields the conditions

$$\frac{5}{3} \alpha \tau^{2/3} - \beta \tau^{-2} = 0, \quad (7.10)$$

$$\frac{1}{\tau} \frac{\partial \beta}{\partial A_e} + \frac{\partial \gamma}{\partial A_e} = 0 \quad (7.11)$$

which yields the relations

$$\tau_{\text{opt}} = \left(\frac{0.6\beta}{\alpha} \right)^{3/8} \quad (7.12)$$

$$(A_e)_{\text{opt}} = 71.73 P^{-3/7} (\alpha/\xi)^{9/35} \left(\xi + \frac{1}{4\pi} \right)^{24/35} \quad (7.13)$$

with

$$\xi = \frac{1}{4\pi} \ln \left(\frac{17671}{(A_e)_{\text{opt}}} \right) + 0.12 \quad (7.14)$$

To solve these equations, we first solve eq. (7.14) numerically and then utilize the resulting value of β in eq. (7.12) to obtain τ_{opt} .

The following analysis of the rms phase error is presented for the conditions of a satellite at 300 km altitude, with an atmospheric transmission of 25%, a quantum efficiency of 10% and an optical transmission efficiency of 33%. The value of $\hat{c}(\infty)$ and α are obtained using the phase structure function specified in the Second Standard Noise Calculation. The parameters for the rms phase error obtained by optimally solving for A_e and the measurement time τ are presented in Table VII-1.

However, it should be noted that the rms phase error can be improved by treating the atmospheric turbulence as a single phase layer at altitude h_o , translating at velocity $\bar{\theta}h_o$.

The new value of $c(\infty)$ becomes

$$\hat{c}_{h_o}(\infty) = 2.91 k^2 \int_0^{\infty} dh C_N^2(h) \left| \frac{\bar{v}}{v} + \bar{\theta}(h - h_o) \right|^{5/3} \quad (7.15)$$

Table VII-1. One-Look RMS Phase Error Measurement
Parameters, $h_o = 0$, $\alpha = 7.06$

Target Intensity, ω/sr	P, photoelectrons per cm^2 per ms	$(A_e)_{opt}$	τ_{opt} , ms	$\langle(\Delta\phi)^2\rangle^{1/2}$	N, II of actuators for D = 150 cm
2000	50.52	19.97	0.0496	0.482	885
1000	25.26	26.55	0.0571	0.543	666
500	12.63	35.29	0.0658	0.611	500
250	6.315	46.88	0.0755	0.686	377
125	3.158	62.24	0.0868	0.771	284
62.5	1.579	82.62	0.0998	0.867	214

For the value of h_o that minimizes $\hat{c}_{h_o}(\omega)$, $\alpha = 2.66$, reduced from $\alpha = 7.06$. The optimized parameters for the rms phase error for these new conditions are presented in Table VII-2.

B. Multiple Phase Layer Predictive Track Scheme

The phase layer estimation procedure for the second Standard Noise Calculation assumed a linear array of 12 detectors viewing the satellite through 12 contiguous columns of atmosphere (Fig. VII-1). In the analysis below, a least squares multiple phase layer estimation procedure is presented for an array of M detectors viewing the satellite for N unit time intervals (Fig. VII-2). A unit time interval T is the time required for a phase patch at the maximum altitude of interest to move one-half of a lens width. This interval T is the same unit integration time used in the second Standard Noise Calculation. It is also assumed that each of the phase measurements $\Delta\phi$ at a detector is obtained in the unit time interval T.

The multiple phase layer procedure described below can be used for an arbitrary number of phase layers. An error analysis is also presented for this estimation procedure. To simplify the analysis, a complete solution is presented for a two phase layer atmosphere. The

4076-79

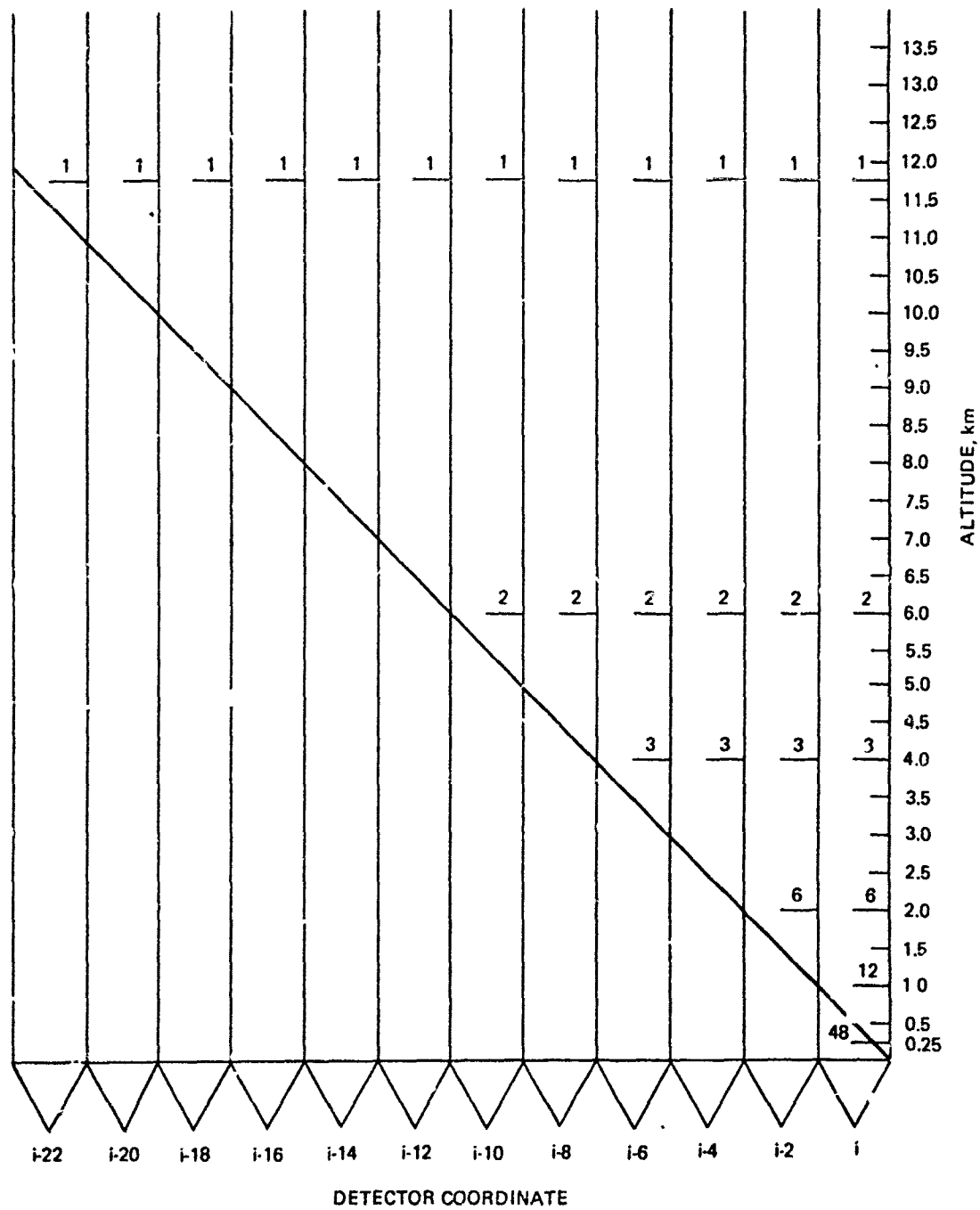


Fig. VII-1. Optical geometry for measurement of phase layers by 12 detectors.

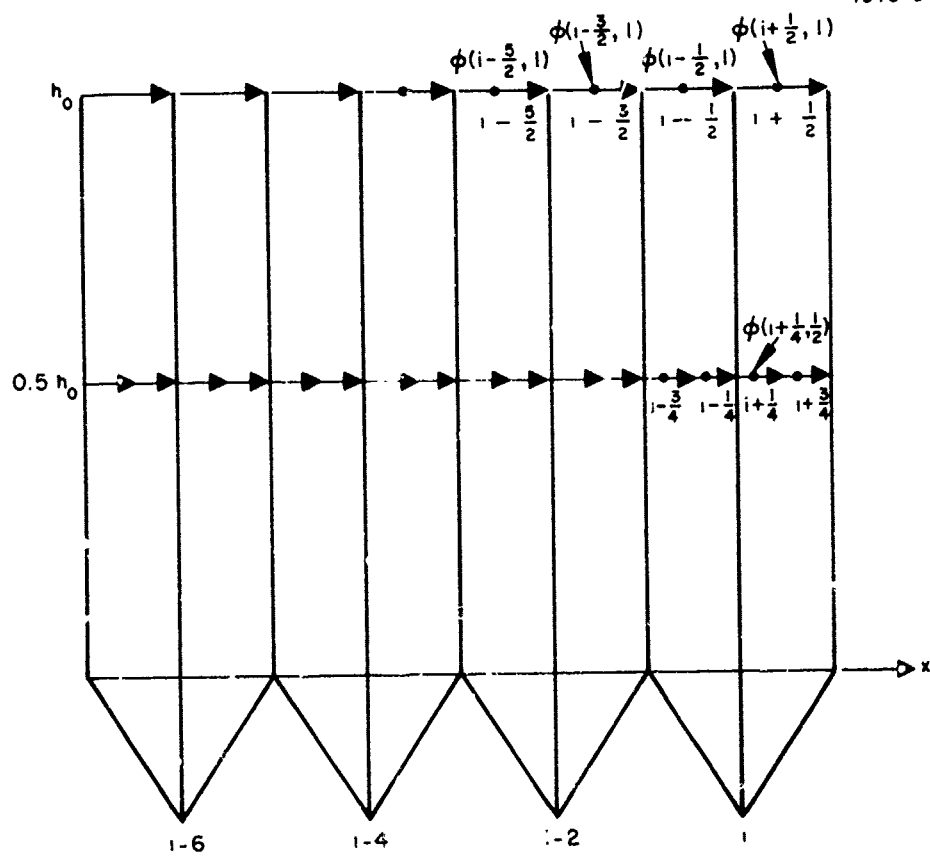


Fig. VII-2. Optical setup for least squares estimation procedure

Table VII-2. One-Look RMS Phase Error Measurement Parameters, $\alpha = 2.66$

Target Intensity, ω/sr	P, photoelectrons per cm^2 per ms	$(A_e)_{\text{opt}}, \text{cm}^2$	$\tau_{\text{opt}}, \text{ms}$	$\langle(\Delta\phi)^2\rangle^{1/2}$	N, II of actuators for D = 150 cm
2000	50.52	15.70	0.079	0.436	1126
1000	25.26	20.88	0.091	0.492	846
500	12.63	27.75	0.105	0.55 π	636
250	6.315	36.88	0.121	0.621	479
125	3.158	48.98	0.139	0.698	361
62.5	1.579	65.04	0.159	0.785	272

error analysis below identifies six different types of phase patterns that cannot be measured by the detector array. Three of these phase patterns will not degrade the image and the other three patterns probably do not occur often.

The phase model used for the non-overlap geometry of Fig. VII-2 assumes

$$\begin{aligned} \Delta\phi(i, t) = & \left[\phi_t\left(i + \frac{1}{2}, 1\right) - \phi_t\left(i - \frac{1}{2}, 1\right) \right] \\ & + \frac{1}{2} \left[\phi_t\left(i + \frac{3}{4}, \frac{1}{2}\right) + \phi_t\left(i + \frac{1}{4}, \frac{1}{2}\right) \right. \\ & \left. - \phi_t\left(i - \frac{1}{4}, \frac{1}{2}\right) - \phi_t\left(i - \frac{3}{4}, \frac{1}{2}\right) \right] \end{aligned} \quad (7.16)$$

where $\Delta\phi(i, t)$ is the phase measurement $\Delta\phi$ of the i^{th} detector ($-4, -2, 0, 2, 4, \dots$) at time t and $\phi_t(i + \alpha, \beta)$ is the lumped parameter value of the phase patch at time t and position $(i + \alpha, \beta h_0)$; h_0 the altitude of the

top phase layer. It is also useful to note, for formulation of the measurement process that

$$\phi_{t-nT}(i + \alpha, \beta) = \phi_t(i + \alpha + r, \beta) . \quad (7.17)$$

In the formulation of the least squares problem, we are given a real $m \times n$ matrix A of rank $k \leq \min(m, n)$

$$\Delta \underline{\phi} = A \underline{\phi} \quad (7.18)$$

obtained from (7.16) and (7.17) and the set of measurements we chose to make. Figure VII-3 illustrates matrix A for a choice of 19 measurements made over nine time intervals at three detectors. Given any real m -vector $\Delta \underline{\phi}$, we wish to find a real n -vector $\hat{\underline{\phi}}$ that minimizes the euclidean length $\|A \hat{\underline{\phi}} - \Delta \underline{\phi}\|$. The solution to the least squares problem obtains the orthogonal decomposition

$$A = H R K^T \quad (7.19)$$

where H is an $m \times m$ orthogonal matrix, R is an $m \times n$ matrix of the form

$$R = \begin{bmatrix} R_{11} & 0 \\ 0 & 0 \end{bmatrix} \quad (7.20)$$

R_{11} is a $k \times k$ matrix of rank k , and K is an $n \times n$ orthogonal matrix. It is a theorem¹² that the unique minimum length least squares solution is given by

$$\hat{\underline{\phi}} = K \begin{pmatrix} R_{11}^{-1} & 0 \\ 0 & 0 \end{pmatrix} H^T \Delta \underline{\phi} \quad (7.21)$$

$$\hat{\underline{\phi}} \triangleq A_1 \Delta \underline{\phi}$$

The pseudoinverse A_1 for A in Fig. VII-3 is shown in Fig. VII-4. The rank of A is 16; $\Delta\phi$ is a 19-vector and ϕ is a 22-vector. Since the rank of A is six less than 22-vector ϕ , there are six basis vectors, i. e., independent phase patterns, that cannot be obtained from the measurements $\Delta\phi$.

As a check that matrix A_1 , the pseudoinverse of A is correctly computed, we can project forward the values of ϕ to obtain the estimated values of $\Delta\hat{\phi}(i+2, t+5T)$, where

$$\begin{aligned} \Delta\phi(i+2, t+5T) = & \left[\phi\left(i - 2\frac{1}{2}, 1\right) - \phi\left(i - 3\frac{1}{2}, 1\right) \right] \\ & + \frac{1}{2} \left[\phi\left(i + \frac{1}{4}, \frac{1}{2}\right) + \phi\left(i - \frac{1}{4}, \frac{1}{2}\right) \right. \\ & \left. - \phi\left(i - \frac{3}{4}, \frac{1}{2}\right) - \phi\left(i - 1\frac{1}{4}, \frac{1}{2}\right) \right] \end{aligned} \quad (7.22)$$

from (7.16) and (7.17). Forming the propagator matrix

$$P^T = (0, 0, 0, 0, 0, 0, 0, 1, -1, 0, 0, 0, 0, 0, 0, 0, .5, .5, -.5, -.5, 0, 0, 0) \quad (7.23)$$

where $\Delta\hat{\phi}(i+2, t+5T) = P^T \Delta\phi$ and ϕ is defined in Fig. VII-3. It can be shown that

$$\begin{aligned} \Delta\hat{\phi}(i+2, t+5T) = & P^T \Delta\phi = P^T A_1 A\phi \\ = & \phi\left(i - 2\frac{1}{2}, 1\right) - \phi\left(i - 3\frac{1}{2}, 1\right) \\ & + \frac{1}{2} \left[\phi\left(i + \frac{1}{4}, \frac{1}{2}\right) + \phi\left(i - \frac{1}{4}, \frac{1}{2}\right) \right. \\ & \left. - \phi\left(i - \frac{3}{4}, \frac{1}{2}\right) - \phi\left(i - 1\frac{1}{4}, \frac{1}{2}\right) \right] \end{aligned} \quad (7.24)$$

which is mathematically identical with definition (7.22).

Similar techniques can be used to compute the rms phase error of the estimate for $\Delta\hat{\phi}(i+2, t+5T)$, the phase correction at time $t+5T$ after all measurements are concluded. By computing the phase correction estimate

$$\Delta\hat{\phi}(i+2, t+5T)^T = P^T A_1 \Delta\phi \quad (7.25)$$

the variance of $\Delta\hat{\phi}(i+2, t+5T)$ is given by

$$\begin{aligned} \langle \Delta\hat{\phi}, \Delta\hat{\phi}(i+2, t+5T) \rangle &= \langle (P^T A_1 \Delta\phi)^T, P^T A_1 \Delta\phi \rangle \\ &= P^T A_1 (P^T A_1)^T \langle \Delta\phi^T, \Delta\phi \rangle \\ &= 1.75 \langle (\Delta\phi)^2 \rangle \end{aligned} \quad (7.26)$$

for the three detectors and 19 measurements of Fig. VIII-3. The use of more detectors over more time intervals will considerably reduce the predicted rms phase error $\langle (\Delta\hat{\phi})^2 \rangle$.

C. Unobservable Multiple Phase Layers

All matrices for the two-layer phase model that have been evaluated in this analysis have always been reduced to a six dimensional subspace of unobservable phase patterns. In order to determine whether these unobservable phase patterns can badly degrade the image and to assess whether these unobservable phase patterns are fundamental to the two layer measurement process or are just artifacts of the phase estimator design procedure, it was felt necessary to identify a set of six basis vectors for this null space. The basis vectors are

$$\begin{aligned} 1. \quad \phi \left(i + \frac{1}{2}, 1 \right) &= a_0 & i = 0, \pm 1, \pm 2, \dots & \quad (7.27) \\ \phi \left(j + \frac{1}{4}, \frac{1}{2} \right) &= 0 & j = 0, \pm 0.5, \pm 1, \pm 1.5, \dots & \end{aligned}$$

$$2. \quad \phi \left(i + \frac{1}{2}, 1 \right) = 0 \quad i = 0, \pm 1, \pm 2, \dots \quad (7.28)$$

$$\phi \left(j + \frac{1}{4}, \frac{1}{2} \right) = b_0 \quad j = 0, \pm .5, \pm 1, \pm 1.5, \dots$$

$$3. \quad \phi \left(i + \frac{1}{2}, 1 \right) = 0 \quad i = 0, \pm 1, \pm 2, \dots \quad (7.29)$$

$$\phi \left(j + \frac{1}{4}, \frac{1}{2} \right) = (-1)^{2j} b_0 \quad j = 0, \pm .5, \pm 1, \pm 1.5, \dots$$

$$4. \quad \phi \left(i + \frac{1}{2}, 1 \right) = 0 \quad i = 0, \pm 1, 2, \dots \quad (7.30)$$

$$\phi \left(j_0 + j + \frac{1}{4}, \frac{1}{2} \right) = (-1)^{2j} [j] b_0 \quad j_0, j = 0, \pm .5, \pm 1, \pm 1.5, \dots$$

where $[j] \triangleq n$ for $n \leq j < n+1$

$$5. \quad \phi \left(i_0 + i + \frac{1}{2}, 1 \right) = i \cdot a_0 \quad i_0, i = 0, \pm 1, \pm 2, \dots \quad (7.31)$$

$$\phi \left(j_0 + j + \frac{1}{4}, \frac{1}{2} \right) = -[j] a_0 \quad j_0, j = 0, \pm .5, \pm 1, \pm 1.5, \dots$$

$$6. \quad \phi \left(i_0 + i + \frac{1}{2}, 1 \right) = \left[\frac{i}{2} \right] a_0 \quad i_0, i = 0, \pm 1, \pm 2, \dots \quad (7.32)$$

$$\phi \left(j_0 + j + \frac{1}{4}, \frac{1}{2} \right) = (-1)^{2j+1} \{ [j]([j] - 1) - \langle j \rangle \} a_0$$

$$j_0 = \frac{(i_0 + 1)}{2} \pm n$$

$$j = 0, \pm .5, \pm 1, \pm 1.5, \dots$$

where $[j] \triangleq n$ for $n \leq j < n+1$ (7.33)

and

$$\langle j \rangle \triangleq \begin{cases} 1 & \text{if } j+.5 \text{ integer} \\ 0 & \text{if } j \text{ integer} \end{cases} \quad (7.34)$$

Examples of each of the six basis phase patterns are given below. The patterns are given for a single point in time with the top layer phase pattern appropriately positioned above the lower layer phase pattern appropriately positioned above the lower layer phase pattern (Fig. VII-5).

Having identified the six basis vectors of the null space, it becomes important to determine whether or not these unobservable phase patterns are a fundamental element of the two layer measurement process. It is claimed, on the basis of the following demonstrative argument, that these six phase patterns are fundamentally unmeasurable using the M contiguous phase detectors operated along parallel lines of sight for N sets of time measurements.

The first pattern $\{\phi(i + 1/2, 1) = a_0 \text{ and } \phi(j + 1/4, 1/2) = 0\}$ is not measurable because for all i

$$\phi\left(i + \frac{1}{2}, 1\right) - \phi\left(i - \frac{1}{2}, 1\right) = 0 \quad (7.35)$$

The second phase pattern $\{\phi(i + 1/2, 1) = 0 \text{ and } \phi(j + 1/4, 1/2) = b_0\}$ is not measurable because for all j

$$.5 \left\{ \phi\left(j + \frac{3}{4}, \frac{1}{2}\right) + \phi\left(j + \frac{1}{4}, \frac{1}{2}\right) - \phi\left(j - \frac{1}{4}, \frac{1}{2}\right) - \phi\left(j - \frac{3}{4}, \frac{1}{2}\right) \right\} = 0 \quad (7.36)$$

The third phase pattern $\{\phi(i + 1/2, 1) = 0 \text{ and } \phi(j + 1/4, 1/2) = (-1)^{2j} b_0\}$ is not measurable because for all j

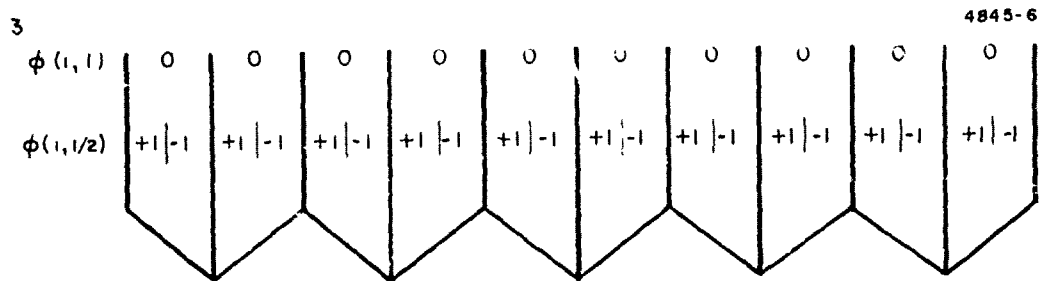
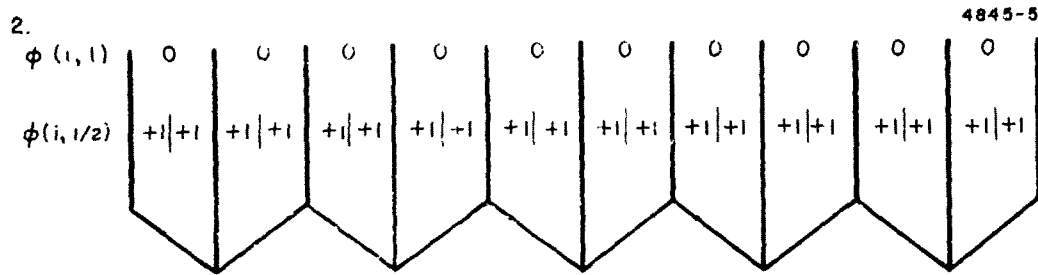
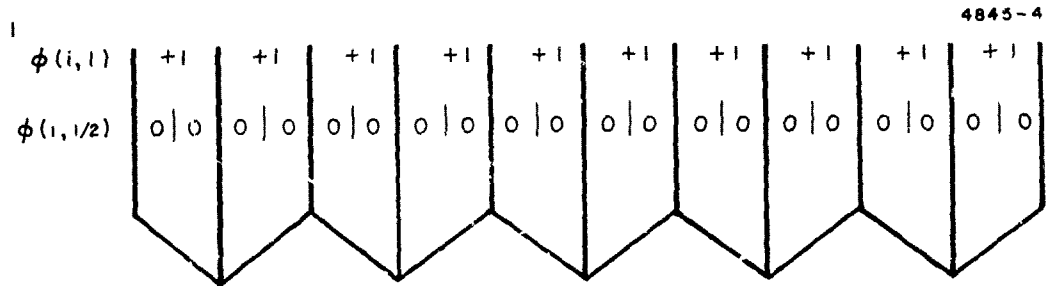


Fig. VII-5. Unmeasurable basis vectors for two layer atmosphere

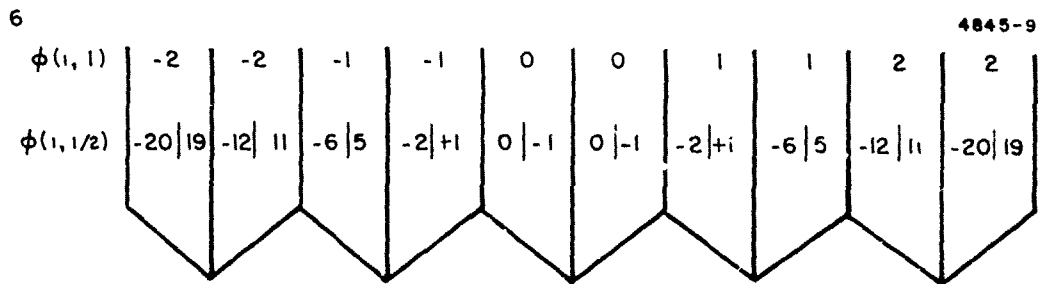
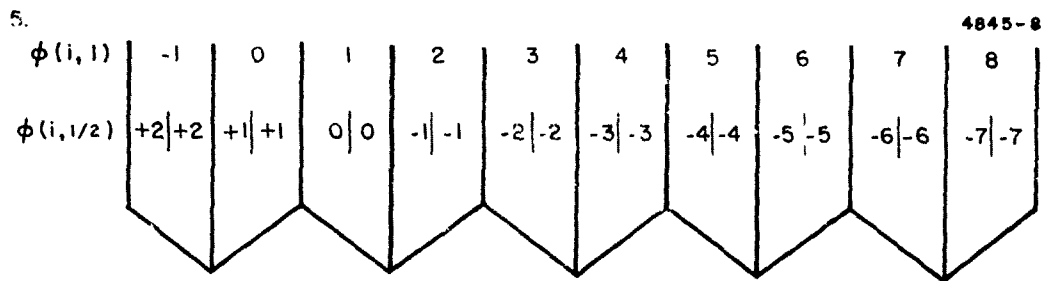
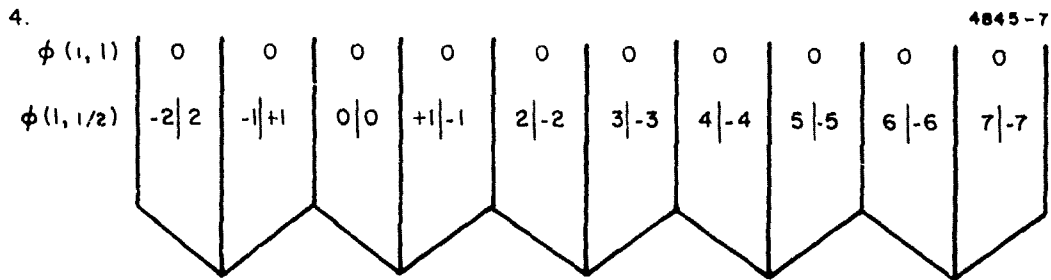


Fig. VII-5. (Continued)

$$\begin{aligned}
& .5 \left\{ \phi \left(j + \frac{3}{4}, \frac{1}{2} \right) + \phi \left(j + \frac{1}{4}, \frac{1}{2} \right) - \phi \left(j - \frac{1}{4}, \frac{1}{2} \right) - \phi \left(j - \frac{3}{4}, \frac{1}{2} \right) \right\} \\
& = .5(-1)^{2j} b_o \left\{ (-1)^2 + (-1)^1 - (-1)^0 - (-1)^{-1} \right\} = 0 \quad (7.37)
\end{aligned}$$

The fourth phase pattern $\{ \phi(i + 1/2, 1) = 0$ and $\phi(j + 1/4, 1/2) = (-1)^{2j} [j] b_o \}$ is not measurable because for all j

$$\begin{aligned}
& .5 \left\{ \phi \left(j + \frac{3}{4}, \frac{1}{2} \right) + \phi \left(j + \frac{1}{4}, \frac{1}{2} \right) - \phi \left(j - \frac{1}{4}, \frac{1}{2} \right) - \phi \left(j - \frac{3}{4}, \frac{1}{2} \right) \right\} \\
& = .5(-1)^{2j} b_o \left\{ \left[j + \frac{1}{2} \right] - [j] - \left[j - \frac{1}{2} \right] + [j - 1] \right\} \\
& = .5(-1)^{2j} b_o \left\{ j - j - (j - 1) + (j - 1) \right\} = 0 \text{ for } j \text{ integer} \\
& = .5(-1)^{2j} b_o \left\{ \left(j + \frac{1}{2} \right) - \left(j - \frac{1}{2} \right) - \left(j - \frac{1}{2} \right) + \left(j - \frac{3}{2} \right) \right\} = 0
\end{aligned}$$

$$\text{for } j + \frac{1}{2} \text{ integer.} \quad (7.38)$$

The fifth phase screen $\{ \phi(i + 1/2, 1) = i \cdot a_o$ and $\phi(j + 1/4, 1/2) = -[j] a_o \}$ is not measurable because for all i

$$\phi \left(i + \frac{1}{2}, 1 \right) - \phi \left(i - \frac{1}{2}, 1 \right) = i \cdot a_o - (i - 1) a_o = a_o \quad (7.39)$$

and for all j

$$\begin{aligned}
& .5 \left\{ \phi \left(j + \frac{3}{4}, \frac{1}{2} \right) + \phi \left(j + \frac{1}{4}, \frac{1}{2} \right) - \phi \left(j - \frac{1}{4}, \frac{1}{2} \right) - \phi \left(j - \frac{3}{4}, \frac{1}{2} \right) \right\} \\
& = -.5 a_o \left(\left[j + \frac{1}{2} \right] + [j] - \left[j - \frac{1}{2} \right] - [j - 1] \right) = -a_o \quad (7.40)
\end{aligned}$$

The contributions a_0 and $-a_0$ from each phase layer combine at the detector to provide zero measured phase difference.

The sixth phase pattern $\{ \phi(i + 1/2, 1) = [i/2] a_0$ and $\phi(j_0 + j + 1/4, 1/2) = (-1)^{2j+1} \{ [j] ([j] - 1) - \langle j \rangle \} a_0 \}$ is not measurable because for all i

$$\begin{aligned} \phi\left(i + \frac{1}{2}, 1\right) - \phi\left(i - \frac{1}{2} - 1\right) &= a_0 \left(\left[\frac{i}{2} \right] - \left[\frac{i-1}{2} \right] \right) \\ &= \begin{cases} a_0 & \text{for } i \text{ even} \\ 0 & \text{for } i \text{ odd} \end{cases} \end{aligned} \quad (7.41)$$

When i is odd, j_0 is an integer and when i is even, $j_0 + .5$ is an integer. The lower layer phase contribution

$$\begin{aligned} \phi_\ell &= .5 \left\{ \phi\left(j_0 + j + \frac{3}{4}, \frac{1}{2}\right) + \phi\left(j_0 + j + \frac{1}{4}, \frac{1}{2}\right) \right. \\ &\quad \left. - \phi\left(j_0 + j - \frac{1}{4}, \frac{1}{2}\right) - \phi\left(j_0 + j - \frac{3}{4}, \frac{1}{2}\right) \right\} \\ &= \begin{cases} 0 & \text{for } j \text{ integer} \\ (-1)^{2j_0} a_0 & \text{for } j + .5 \text{ integer} \end{cases} \end{aligned}$$

Setting $j_0 + .5$ an integer when i is even synchronizes the two phase layers so the contributions a_0 and $-a_0$ combine at the detector on alternate time steps to provide zero measured phase difference. On adjacent time steps, each phase layer contributes zero phase.

It has been shown in this two-phase layer error analysis that there will always be six unobservable phase patterns and they are identified. With the addition of more phase layers to the atmospheric model, there will be more unmeasurable phase patterns added to the null space. If this estimation procedure is pursued, those phase patterns should be identified.

VIII. IMAGE QUALITY WITH RMS PHASE ERROR

We have carried out computer simulation studies of the imaging COAT system to determine if any correlation exists between image quality and residual rms phase error of the segmented mirror. For the simulations, a 1.5 m diameter segmented mirror was considered which was capable of correcting for both phase and tilt distortions in an incident wave. Two different segmented mirrors were considered in the simulation studies, differing in the size of the mirror segments. That is, the number of mesh points encompassed by each mirror segment was different. For the coarsely segmented mirror, each segment encompasses 31 mesh points, while for the finer segmented mirror 14 mesh points were included in each segment. A brief description of the phase and tilt correction code of the segmented mirror is as follows. The phase and tilt of each segment was adjusted to give a least squares fit to the phase of the distorted field over that segment. The difference between the least squares fit and actual phase distribution was introduced as a residual phase error in the system, i. e., the aperture phase distribution in the PSF determination was equated to this residual phase. Comparison with results of more complicated simulations in which deformable mirrors are driven by a COAT servo system indicates that the least squares technique utilized in these studies yields comparable results.⁸

The phase screen used in the simulation studies is generated by a fast Fourier transform technique which yields a two-dimensional distribution of gaussian random numbers having correlation properties consistent with those associated with Kolmogorov turbulence. In particular, we represent the phase in the form

$$\phi(\underline{x}) = \int d\underline{K} [\Phi_{\phi}(\underline{K})]^{1/2} a(\underline{K}) \exp(i \underline{K} \cdot \underline{x}) \quad (8.1)$$

where Φ_{ϕ} is the spatial spectrum of the phase variation, \underline{K} is a spatial wave-number, and $a(\underline{K})$ is a completely random function with zero mean and unity variance, i. e.,

$$\langle a \rangle = 0 \quad (8.2)$$

$$\begin{aligned} \langle a(\underline{K}_1) a^*(\underline{K}_2) \rangle &= 0 \quad \underline{K}_1 \neq \underline{K}_2, \\ &= 1 \quad \underline{K}_1 = \underline{K}_2 \end{aligned} \quad (8.3)$$

Note that with this representation, the random function $\phi(\underline{x})$ satisfies the Wiener-Khinchin theorem

$$\langle \phi(\underline{x}_1) \phi^*(\underline{x}_2) \rangle = \int d\underline{K} \Phi_\phi(\underline{K}) \exp[i \underline{K} \cdot (\underline{x}_1 - \underline{x}_2)] \quad (8.4)$$

as is required for any valid representation of a homogeneous random process.¹

In these studies we have utilized a modified von Karman spectrum for Φ_ϕ

$$\Phi_\phi(\underline{K}) = \frac{0.490 r_o^{-5/3} K_o^{-11/3}}{[1 + K^2/K_o^2]^{11/6}} \quad (8.5)$$

where K_o is 2π divided by the outer scale of turbulence L_o , and r_o is the phase coherence length defined by Fried.⁹ The phase structure function associated with this spectrum is

$$D_\phi(r) = 6.88 (K_o r_o)^{-5/3} \left[\frac{3}{5} - \frac{(K_o r/2)^{5/6} K_{5/6}(K_o r)}{\Gamma(11/6)} \right] \quad (8.6)$$

where $K_{5/6}$ is a modified Bessel function of the 5/6th order. In the limit of an infinite outer scale, the phase structure function given in eq. (8.6) reduces to

$$D_\phi(r) = 6.88 (r/r_o)^{5/3}, \quad (8.7)$$

which is the phase structure function specified in the standard noise calculation problem statement.

To verify that our numerically generated phase screens do indeed satisfy the theoretical relation given in eq. (8.6), we have calculated the phase structure function associated with an ensemble of 100 realizations of phase screen samples generated by a fast Fourier transform evaluation of eq. (8.1). A 64×64 mesh was used in these calculations, and it was assumed that the mesh points are 1.106 cm apart and that the outer scale of turbulence is 2 m. The results of the calculation are shown in Fig. VIII-1 along with a plot of the theoretical expression given in eq. (8.6) and the corresponding infinite outer scale expression given in eq. (8.7).

The results given in Fig. VIII-1 yield the following observations: (1) Our numerical technique for generating the phase screen does, in fact, yield phase screens that have the theoretical phase structure function given in eq. (8.6). The deviation at large separations is caused by the fact that the total extent of the phase screen used in these studies is $64 \times 1.106 = 71$ cm, whereas the outer scale is 2 m. Larger screens are needed to obtain better agreement at large separation values. We feel that this moderate discrepancy at large separations is not important in our simulation studies, because the degree of correction obtainable with a deformable or piston plus tilt mirror does not depend significantly on the large scale properties of the turbulence. (2) A comparison on the theoretical curve for the phase structure function given in eq. (8.6) with the corresponding curve for the infinite outer scale result reveals that the mean square fluctuation between two points is significantly less when $L_0 = 2$ m than it is when $L_0 = \infty$. It is our contention that the phase screens that we are using, for which $L_0 = 2$ m, are adequate for the simulation studies because the increased rms phase fluctuation level observed with $L_0 = \infty$ is due to the additional large scale variations that occur under this condition.

Each phase screen was characterized by the initialization index of the random number generator. Thus, phase screen 3 corresponds to the phase screen generated by the sequence of random numbers obtained with the initialization index of 3. Similar correspondence exists for phase screen 32. The level of turbulence considered in the simulations corresponds to

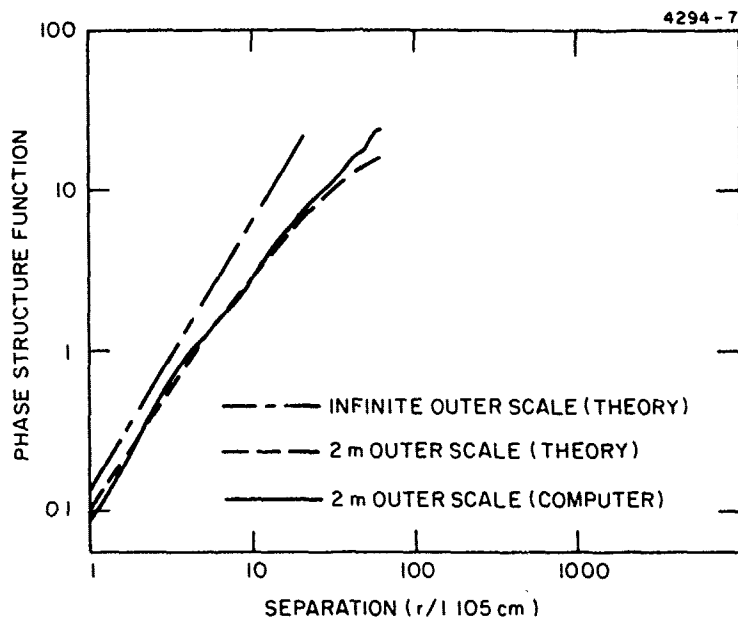


Fig. VIII-1. Comparison of computer calculated and theoretical phase structure function results.

phase coherence lengths of 10 cm and 5 cm. An option was incorporated into the simulation scheme which allowed more than one COAT corrected image to be added. In this way, phase corrected images for many phase screens could be averaged. Both single run (i. e., one phase screen) and five runs averaged (i. e., averaged over five separate phase screens) images were simulated. In addition, the simulations performed did not include the effect of noise in the system.

The object used in the simulations was derived from a digitized tape of the intensity reflection of a scaled model of a satellite, provided by B. L. McGlammery.¹⁰ The object possessed a dynamic range of 1296 intensity levels. Originally, the object was recorded in a 256 x 256 mesh-point format. Because of limitations imposed by core space in the computer, the object was converted to a 128 x 128 format by utilizing only that portion of the object which was pertinent to our simulation studies. A photograph of the object used is shown in Fig. VIII-2. The display is limited to only 16 levels of grey, thereby severely restricting the faithful reproduction of the object because of its large (1296 levels) dynamic range. In order to overcome this dynamic range limitation, enhancement schemes were applied to the object before display. Similarly, the COAT reconstructed images were also enhanced prior to display.

The enhancement technique, which proved to be most useful, is known as the local area brightness and gain control (LABGC) technique. This technique, developed by D. J. Ketcham,¹¹ tabulates the intensity distribution of the pixels within a localized window in the image, calculates the statistical properties therein, and applies a linear gain to pixel values below a threshold value, determined by the statistics within that window. Pixel values above the threshold value are given a gain of one. Thus, the low intensity features of the image are highlighted while the high intensity features are unaltered to prevent saturation. An illustration of the gain curve is shown in Fig. VIII-3. In the enhancement process the replacement of the old pixel values by the "enhanced" values is carried out for only the center portion of the localized window in order to avoid the mosaic effect which would arise if the entire window area is replaced by the new enhanced values. The window is then displaced by one mesh point, and

4845-16

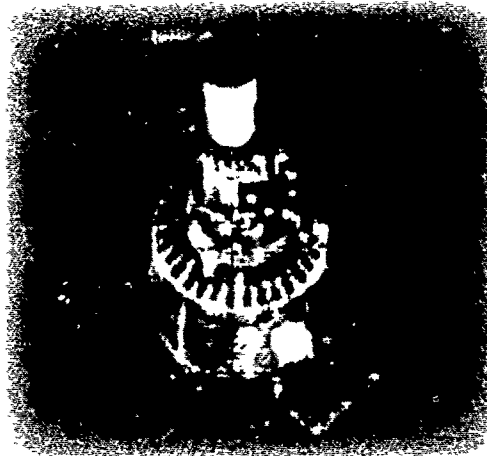


Fig. VIII-2. Photograph of object on display.

4845-10

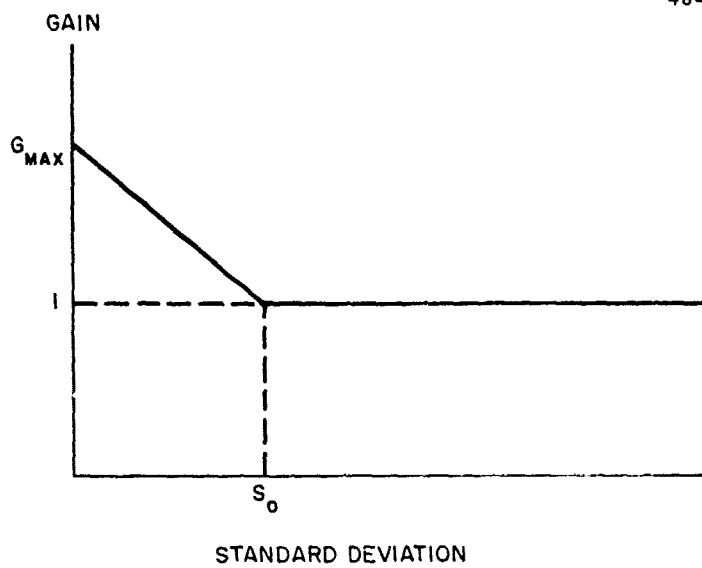


Fig. VIII-3. Selective gain curve applied in LABGC within a window area.

the entire process started over again for the new window until the entire image has thus been enhanced in this fashion. In our enhancement schemes, a 9×9 window was used and a central 2×2 area was used for the updating. A detailed discussion of the LABGC technique is beyond the scope of this report and can be found in Ref. 11. The maximum gain, G_{max} , and the intensity values which determine S_0 in Fig. VIII-3 are input parameters, and can be varied to achieve the best enhancement. It should be emphasized that the simulation scheme has been carried out for a noise-free system. In the presence of noise, the enhancement scheme may bring out noise-related features which are not part of the original object.

The results of the simulation studies are shown in Fig. VIII-4, with the parameters of the corresponding simulations listed in Table VIII-1. Once chosen, the gain and threshold values used for these enhanced pictures were kept constant for all cases. They were chosen, after many trial-and-error processes, as presenting the most pleasing visual images of the COAT corrected data, i. e., the details of the low intensity features of the image have been properly highlighted. It is seen from Table VIII-1 that Fig. VIII-4 contains the images reconstructed from consideration of phase screen 3. Figures VIII-4(a) and VIII-4(b) are simulations in which the phase coherence length is 10 cm; while Figs. VIII-4(c) and VIII-4(d) are for 5 cm phase coherence length. Figures VIII-4(a) and VIII-4(c) employed 506 actuators in the simulations, thereby representing a finely segmented mirror; Figs. VIII-4(b) and VIII-4(d) employed 225 actuators and represent a coarsely segmented mirror. All simulations in Fig. VIII-4 were carried out for only one phase screen. The residual rms phase error for each case is shown in the last column, and range from 0.582 radians to 1.25 radians. It is seen that there is a general improvement in image quality when the residual phase error is decreased significantly. This is shown by comparing Figs. VIII-4(c) and VIII-4(d) with Fig. VIII-4(a). However, when the residual phase errors are not significantly different, the improvement in image quality becomes less apparent, if at all. This can be seen by comparing Fig. VIII-4(c) with Fig. VIII-4(d), or VIII-4(a) with VIII-4(b). Similar remarks hold for the other figures of Table I.

Table VIII-1. Simulation Conditions

Figure	Phase Screen	Phase Coherence Length, cm	Number of Actuators	Number of Runs	Residual ϕ_{rms}
VIII-4a	3	10	506	1	0.582
VIII-4b	3	10	225	1	0.750
VIII-4c	3	5	506	1	0.969
VIII-4d	3	5	225	1	1.25
VIII-5a	32	10	506	1	0.577
VIII-5b	32	10	225	1	0.790
VIII-5c	32	5	506	1	0.962
VIII-5d	32	5	225	1	1.32
VIII-6a	3	10	506	5	0.590
VIII-6b	3	10	225	5	0.793
VIII-6c	3	5	506	5	0.984
VIII-6d	3	5	225	5	1.32
VIII-7a	32	10	506	5	0.607
VIII-7b	32	10	225	5	0.836
VIII-7c	32	5	506	5	1.01
VIII-7d	32	5	225	5	1.39

An examination of the enhanced images of Figs. VIII-4 through 7 shows that overall, when the residual phase errors are significantly different in magnitude, there is a correlation between image quality and residual rms phase error. For example, the image quality is significantly different between the -a and -c or -d images of each figure. Here, the residual rms phase errors differed by nearly a factor of 2 to 2.5. However, as the difference in the phase errors is decreases, it becomes more difficult to detect any obvious improvements in image quality. This point is readily illustrated by Figs. VIII-4(c) and (d), where (d) has a larger value of residual phase error, but it is not obvious that the image quality

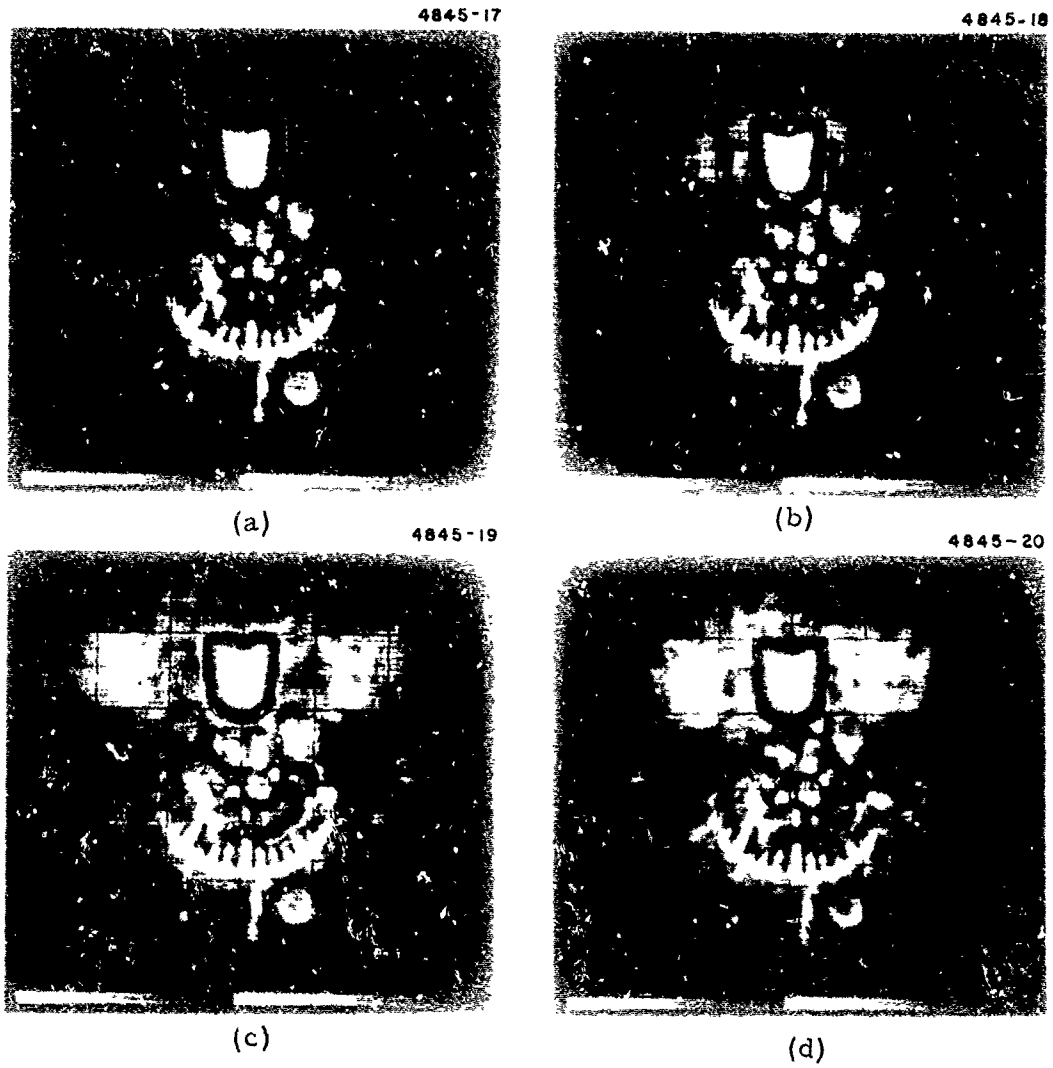


Fig. VIII-4. Degraded image, using phase screen No. 3 for conditions in Table VIII-1.

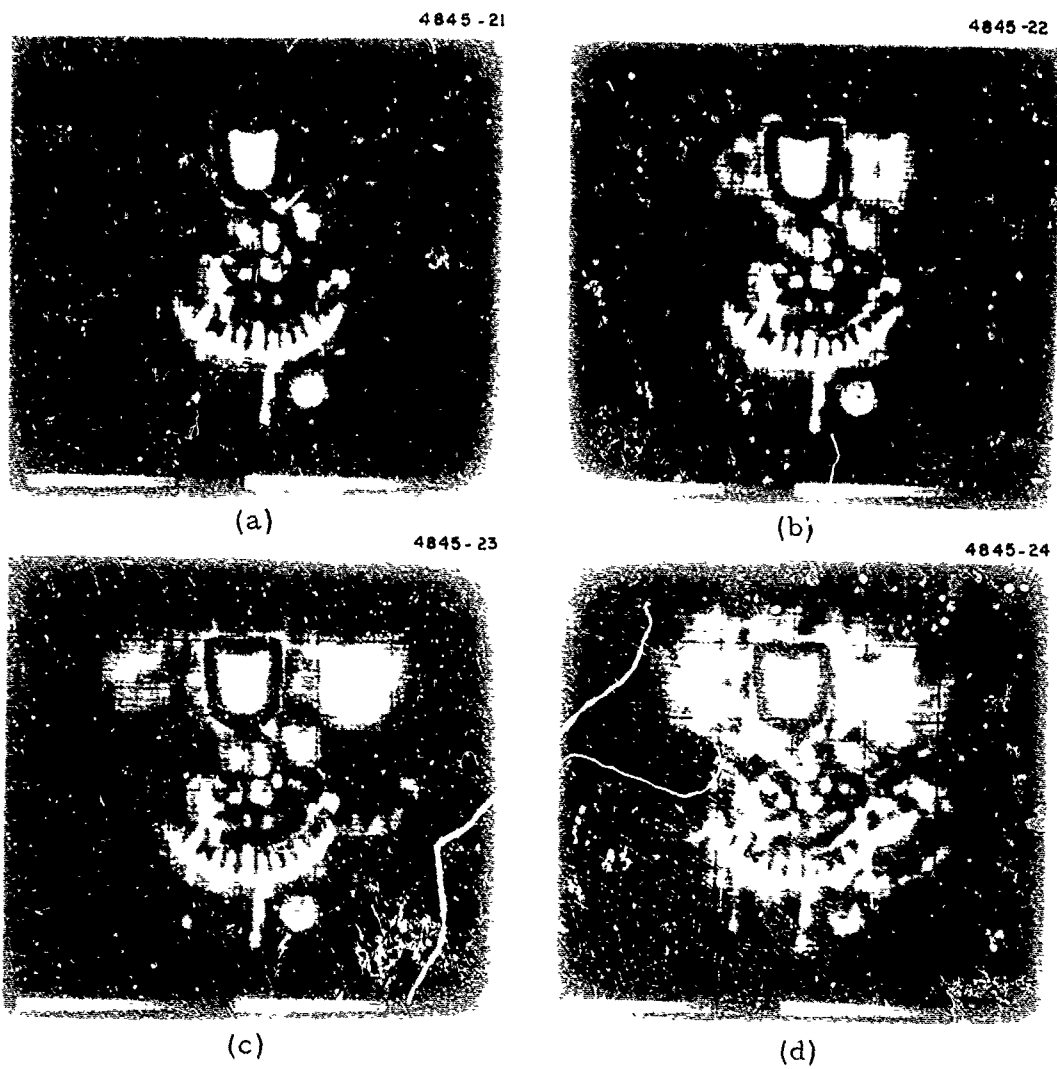


Fig. VIII-5. Degraded image, using phase screen No. 32 for conditions in Table VIII-1.

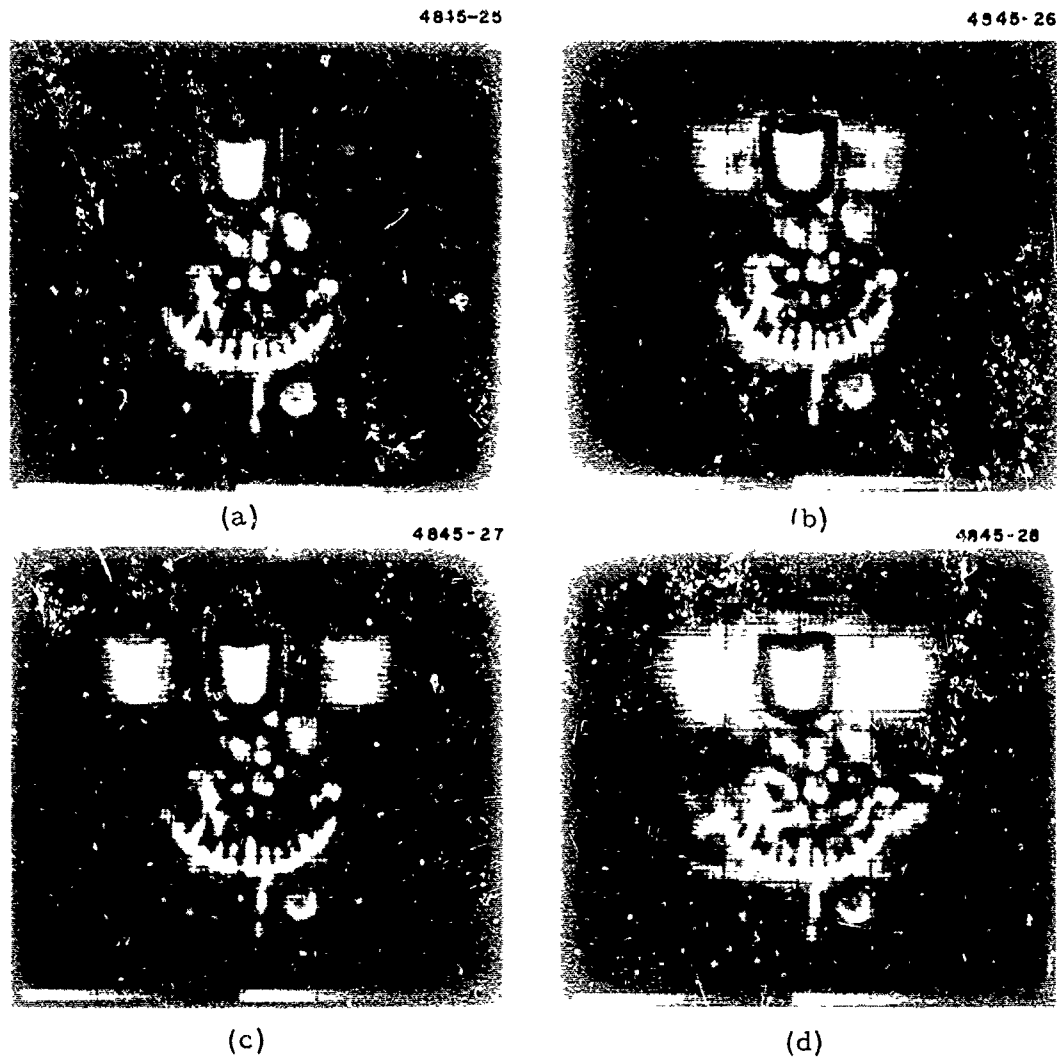


Fig. VIII-6. Degraded image, smoothed using five separate representations of random phase screen No. 3 for conditions in Table VIII-1.

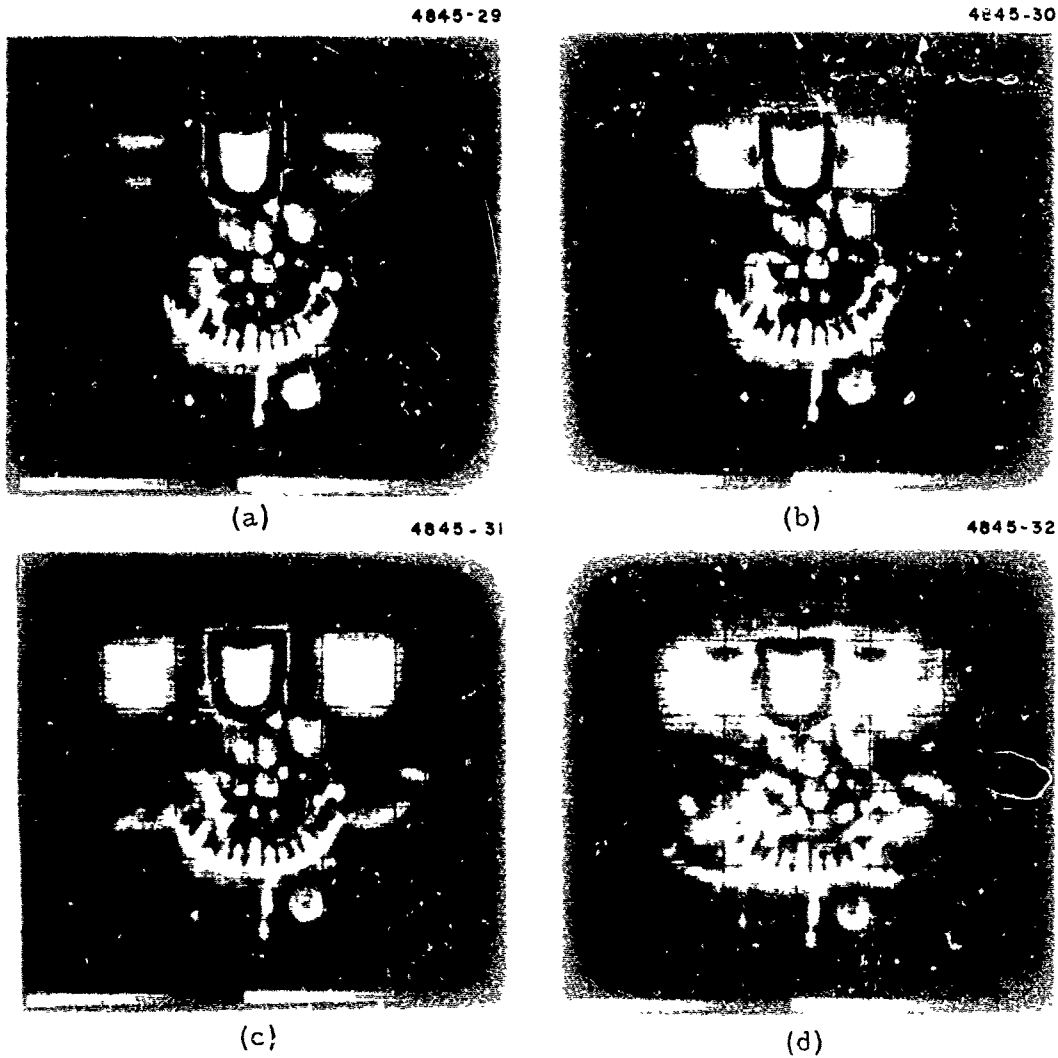


Fig. VIII-7. Degraded image, smoothed using five separate representations of random phase screen No. 32, for conditions in Table VII-1.

is worse than Fig. VIII-4(c). Other figures show a gradual degradation in image quality as residual phase error is increased slightly. This effect seems to be more pronounced for lower values of ϕ_{rms} . The multiple images which sometimes appear in these figures are due to the side-lobes associated with the segmented mirror. As the number of actuators is decreased, thereby necessitating a larger block of mesh points for each segment, the period of the segmented blocks is increased. Thus, the sidelobes appear closer together and introduce closer spaced multiple images as in the -b and -d parts of each figures.

IX. REPORT CONCLUSIONS

This final report for the predetection compensated imaging study provides the opportunity to review the major conclusions and the significant accomplishments of the study. The nature of the study itself changed very early with the contract redirection to emphasize theoretical evaluation of the candidate predetection compensated imaging concepts.

One of the most significant conclusions of the study was the theoretical evaluation of the sensitivity of the following wavefront error sensors:

- Hartman test system
- Pinhole interferometer
- Integral of intensity through a mask (pinhole image quality sensor).

The Hartman test system was shown to be a very sensitive wavefront error sensor. Although its sensitivity is good, the pinhole interferometer was shown to have difficulties with wavefront error connection when viewing a multiple glint target. The pinhole image quality sensor with one detector was found to have extremely poor sensitivity.

However, another major development in the study was the evaluation of the multiple aperture interlinked (MAIL) predetection compensated imaging system. This MAIL concept obtains a significantly improved sensitivity compared with the pinhole image quality sensor by employing multiple detectors to sense wavefront error within blocks of the full telescope aperture. The MAIL system was the candidate concept for evaluation in the first and second Standard Noise Calculations.

PRECEDING PAGE BLANK-NOT FILMED

REFERENCES

1. "Revised Standard Noise Calculation for Predetection Compensation Imaging Systems," Hughes Research Laboratories, Feb. 27, 1975.
2. "Another Standard Noise Calculation for Predetection Compensation Imaging Systems," Hughes Research Laboratories, April 28, 1975.
3. A. P. Sage, Optimum Systems Control (Prentice-Hall, 1968).
4. A. P. Sage and J. L. Melsa, Estimation Theory with Applications to Communications and Control (McGraw-Hill, 1971).
5. V. L. Berezinskii, Soviet Phys. -JETP 34- 610 (1971).
6. J. Goldstone, Nuovo Cimento 19, 154 (1961); J. Goldstone, A. Salam and S. Weinberg, Phys. Rev. 127, 965 (1962).
7. N. D. Mermin and H. Wagner, Phys. Rev. Lett. 17, 1133 (1966).
8. W. P. Brown, "Computer Simulation of Adaptive Optical System," NSWC Final Report on Contract N60921-74-C-0249, Sept. 1975.
9. D. L. Fried, "Optical Resolution Through A Randomly Inhomogeneous Medium for Very Long and Very Short Exposures," J. Opt. Amer. 56, 1372-1379 (1966).
10. B. L. McGlammery, "Computer Simulations and Processing of Degraded Images," Scripps Institute of Oceanography, RADC-TR-74-65.
11. D. J. Ketcham, "Image Enhancement Techniques for Cockpit Display," Tech. Rept. No. P74-530R, HAC Ref. D0802.
12. C. E. Lawson and R. J. Hanson, Solving Least Squares Problems (Prentice-Hall, 1974).

APPENDIX

CALCULATION I_m , THE DEGREE OF COHERENCE

This appendix calculates the intensity and depth of modulation of one output of an interferometer whose inputs are I_n and I_w .

The degree of coherence between I_n and I_w can be expressed by writing

$$e_n(t) = e_o(t) + e_1(t)$$

and

$$e_w(t) = \alpha e_o(t) + e_2(t)$$

where the $e(t)$ are instantaneous electric fields and e_o, e_1 , and e_2 have no mutual coherence:

$$\langle e_o(t)e_1(t) \rangle \sim 0$$

$$\langle e_1(t)e_2(t) \rangle \sim 0$$

$$\langle e_o(t)e_2(t) \rangle \sim 0$$

The angular brackets denote time average over about a microsecond (i.e., short with respect to the I-Coat system response, but long compared with the 10^{-15} sec period of light oscillations). The electric fields are normalized so that

$$I_i = \langle e_i(t)^2 \rangle \text{ for } i = n, w, o, 1, 2.$$

then

$$I_n = I_o + I_1$$

and

$$I_w = \alpha^2 I_o + I_2.$$

PRECEDING PAGE BLANK-NOT FILMED

The output of an interferometer that combines I_n and I_w is

$$I_c = \langle [e_n(t) + e_w(t+\Delta)]^2 \rangle$$

$$= I_n + I_w + 2\langle e_n(t)e_w(t+\Delta) \rangle$$

$$= I_n + I_w + 2\alpha \langle e_o(t)e_o(t+\Delta) \rangle + \text{equal to}$$

zero, where Δ is the path difference divided by the speed of light. Assuming an average light frequency ν , and some degree of chromatism, for small Δ we have

$$\langle e_o(t)e_o(t+\Delta) \rangle \sim I_o \cos \Delta\nu,$$

then

$$I_c = 1/2 (I_n + I_w + 2\alpha I_o \cos \Delta\nu).$$

The average intensity is $I_n + I_w$, as expected, and $2\alpha I_o$ is the peak modulation. We define $I_m \equiv 2\alpha I_o$.

We now calculate and evaluate I_o for various cases. A cross section of the intensity distribution before and after the narrow and wide pinholes is shown to the right for each case. Since both the narrow and wide pinholes are approximately unresolvable by each subaperture, each of the n interferometers has as its two inputs $1/n$ of the total light penetrating the wide and narrow pinholes.

1. Cases I and II, Small σ

Since all the light originates from an unresolved point (small σ), I_n and I_w are fully coherent:

$$I_1 = I_2 = 0$$

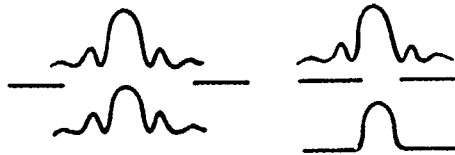
$$I_o = I_n$$

$$v = \sqrt{I_w/I_n}$$

so

$$I_m = 2 \sqrt{I_w I_n}$$

4845-13



2. Cases I and II, Large σ

Since the system is converged, different areas of the image on the pinholes originate from different areas on the target and are thus uncorrelated. So the shaded portion of the image passing the wide pinhole is coherent with the light passing the narrow pinhole:

$$I_o = I_n$$

$$\alpha^2 I_o = \frac{1}{v^2} I_w$$

so

$$I_m = \frac{2}{v} \sqrt{I_w I_n}$$

4845-12

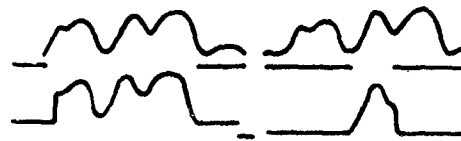


3. Cases III and IV, Small σ

As in 1. above, all the light originates from an unresolved point so I_n and I_w are fully coherent:

$$I_m = 2 \sqrt{I_w I_n}$$

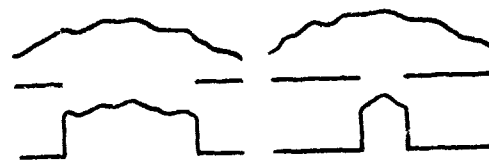
4845-11



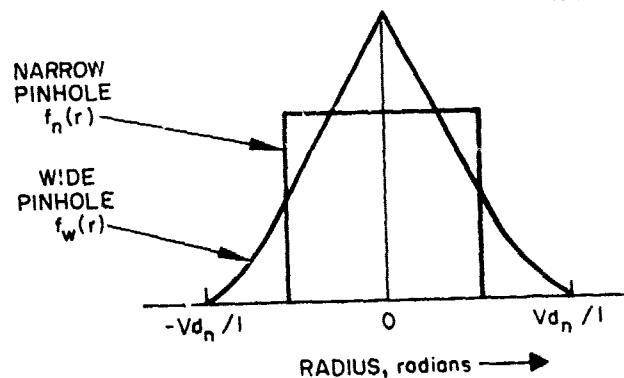
4. Cases III and IV, Large σ

Here, the unconverged condition causes the light from each target point to be spread to a width Vd_n^* . The light penetrating the narrow pinhole is therefore a (roughly) uniform mixture of light from a circular region on the target of angular diameter Vd_n/ℓ . The light penetrating the wide pinhole is a mixture of light from a region on the target of angular diameter $2Vd_n/\ell$, with the mixture weighted by a radial function which gives the overlap of two equal circles of angular diameter Vd_n/ℓ . One of these circles is the spread caused by nonconvergence and the other is the wide pinhole. The weighting functions for the narrow and wide pinholes look like

4845-14



4845-15



Letting $e_n(t)$ be the electric field at point \underline{r} on the target, we have

$$e_n(t) = \int_{-\infty}^{\infty} \sqrt{f_n(\underline{r})} e_{\underline{r}}(t) d\underline{r}^2$$

and

$$e_w(t) = \int_{-\infty}^{\infty} \sqrt{f_w(\underline{r})} e_{\underline{r}}(t) /r/ d\underline{r}^2 .$$

Then letting $\langle e_{\underline{r}}^2 \rangle \equiv I_{\underline{r}}$,

$$\begin{aligned} \langle e_n e_w \rangle &= \left\langle \int_{-\infty}^{\infty} \int_{-\infty}^{\infty} \sqrt{f_n(\underline{r}_1) f_w(\underline{r}_2)} e_{\underline{r}_1} e_{\underline{r}_2} d\underline{r}_1^2 d\underline{r}_2^2 \right\rangle \\ &= \int_{-\infty}^{\infty} \sqrt{f_n(\underline{r}) f_w(\underline{r})} I_{\underline{r}} d\underline{r}^2 \end{aligned}$$

since $\langle e_{\underline{r}_1} e_{\underline{r}_2} \rangle = \delta(\underline{r}_1 - \underline{r}_2) \langle e_{\underline{r}_1}^2 \rangle$

and similarly,

$$I_n = \langle e_n^2 \rangle = \int_{-\infty}^{\infty} f_n(\underline{r}) I_{\underline{r}} d\underline{r}$$

and

$$I_w = \langle e_w^2 \rangle = \int_{-\infty}^{\infty} f_w(\underline{r}) I_r d\underline{r}.$$

The interferometer output is then

$$I_c = I_n + I_w + I_m \cos(\Delta \cdot \underline{D}),$$

where

$$I_m = 2 \int_{-\infty}^{\infty} \sqrt{f_n(\underline{r}) f_w(\underline{r})} I_r d^2 \underline{r}.$$

Recalling our original definition of the target, we have

$$I_r \propto e^{-|\underline{r}|^2 / 2\sigma^2}.$$

If σ is large, then I_r is nearly constant when f_n and f_w are nonzero, and

$$I_m = 2 I_{r=0} \int_{-\infty}^{\infty} f_n(\underline{r}) f_w(\underline{r}) d^2 \underline{r},$$

$$I_n = I_{r=0} \int_{-\infty}^{\infty} f_n(\underline{r}) d^2 \underline{r},$$

and

$$I_w = I_{r=0} \int_{-\infty}^{\infty} f_w(\underline{r}) d^2 \underline{r}.$$

Therefore,

$$I_m = 2 \sqrt{I_n I_w} \int_{-\infty}^{\infty} \sqrt{f_n(\underline{r}) f_w(\underline{r})} d^2 \underline{r} \left/ \sqrt{\int_{-\infty}^{\infty} f_n(\underline{r}) d^2 \underline{r} \int_{-\infty}^{\infty} f_w(\underline{r}) d^2 \underline{r}} \right.$$

For our functions f_n and f_w

$$I_m \sim 1.4 \sqrt{I_n I_w}.$$